Alma Mater Studiorum – University of Bologna

DEPARTMENT OF ELECTRICAL ENGINEERING
FACULTY OF ENGINEERING

XXII Ph.D.Course in Electrotechnic Engineering
ELECTRIC SYSTEMS FOR ENERGY (ING-IND/33)

PARTIAL DISCHARGES IN POWER DISTRIBUTION ELECTRICAL SYSTEMS: PULSE PROPAGATION MODELS AND DETECTION OPTIMIZATION

Ph.D. Thesis

by

MARCO TOZZI
Dr. Eng.

Tutor:

Prof. Eng. Andrea Cavallini

Coordinator:

Prof. Eng. Francesco Negrini

Prof. Eng. Gian Carlo Montanari

Final Dissertation 2010

Contents

Introduction pag. 1

Chapter 1: PD Propagation and detection in Medium Voltage Cables pag. 5

1.1 Premise pag. 5
1.2 Extraction of cables propagation constant pag. 6
1.2.1 Time Domain Reflectometry method pag. 7
1.2.2 Scattering matrix method pag. 8
1.2.3 Determination of cables propagation constant through analytical models pag. 14
1.3 Determination of cable propagation constant through approximate analytical model pag. 18
1.4 Determination of cables optimum detection bandwidth pag. 28
1.5 Coupling mechanisms for PD in cables pag. 39
1.6 Typical sensors for PD detection in MV cables pag. 48

Chapter 2: PD Pulse propagation and detection in Medium Voltage Transformers pag. 53

2.1 Premise pag. 53
2.2 Overview on existing PD detection methods pag. 55
2.2.1 PD detection from capacitive taps in power transformers pag. 55
2.2.2 UHF detection using internal and external sensors in power transformers pag. 56
2.2.3 Acoustic techniques pag. 58
2.2.4 Detection through HFCT sensors installed on power cables at transformer termination pag. 59

2.3 Investigation of irradiation properties of a metallic shielded enclosure with apertures pag. 60
2.3.1 Analytical evaluation of electric and magnetic fields within a metallic box with a circular aperture pag. 63
2.3.2 Experimental irradiation test pag. 69
2.3.3 Analytical model of a shielded enclosure with a circular aperture pag. 76
2.3.4 Simulations using CAD systems pag. 83
2.4 Investigation of PD irradiation properties of a three-phase distribution transformer pag. 89
2.4.1 Experimental irradiation tests pag. 90
2.4.2 Simulations using CAD systems pag. 94
2.5 Design of an UHF coupler for PD acquisition in MV transformers pag. 107
2.5.1 Description of the antenna sensor pag. 109
2.5.2 Optimization procedures pag. 116
2.6 Partial Discharge measurement on a three-phase MV transformer pag. 121

Chapter 3: PD propagation and detection in Medium Voltage Switchgears pag. 127

3.1 Premise pag. 127
3.2 Overview on existing PD detection methods pag. 128
3.2.1 PD detection from HFCT sensors installed inside the switchgear pag. 128
3.2.2 PD detection from capacitive couplers installed inside the switchgear pag. 129
3.2.3 PD detection from Transient Earth Voltage capacitive sensors pag. 129
3.2.4 PD detection through acoustic sensors pag. 131
3.3 Investigation of PD irradiation properties inside and outside switchgears pag. 132
3.3.1 PD detection inside switchgears through internal sensors pag. 132
3.3.2 PD detection outside switchgears through external antenna sensors pag. 134
3.3.3 Simulations using CAD systems pag. 139
3.4 PD detection through proper antenna

sensors pag. 141

Chapter 4: Applications: on-line PD detection in MV grids pag. 143

4.1 Premise pag. 143
4.2 Examples of on-line PD measurement setups pag. 145
4.3 PD detection and localization in MV cables pag. 147
4.4 PD detection in MV transformers pag. 150
4.5 PD investigation in MV substations pag. 151
4.5.1 PD sources localization in MV switchgears pag. 151
4.5.2 PD detection in MV switchgears through EM field couplers pag. 155
4.5.3 Discrimination between PD sources close and far from the switchgears pag. 157
4.6 Conclusions pag. 160

References pag. 161

Introduction

Investigation on impulsive signals, originated from Partial Discharge (PD) phenomena, represents an effective tool for preventing electric failures in High Voltage (HV) and Medium Voltage (MV) systems. As a matter of facts, such PD activities can be considered as both a cause and consequence of the degradation of insulation systems. Indeed, PD phenomena occur due to insulation defects, but, if neglected, can lead to further degradation and, eventually, to the complete breakdown. For these reasons, PD phenomena can constitute a valuable diagnostic index, which allows both instantaneous insulation condition assessment and life prediction to be carried out.

Diagnosis based on PD investigation can be basically divided into three phases: (a) PD pulses acquisition, (b) separation of signals coming from PD sources to those coming from disturbances and noise, (c) data interpretation for risk assessment. As regards the signal acquisition, the determination of both the sensor and instrument bandwidths is the key to achieve meaningful measurements, that is to say, obtaining the maximum Signal-To-Noise Ratio (SNR). The optimum bandwidth, which can be defined as the bandwidth where SNR is optimum and, thus, where PD detection is carried out with maximum sensitivity, depends on the characteristics of the system under test, which can be often represented as a transmission line characterized by signal attenuation and dispersion phenomena.

Indeed, when PD occur inside an electrical apparatus, Electro-Magnetic (EM) waves can propagate inside and outside the system through irradiation mechanisms. At the same time, the PD pulses can propagate by conduction,

along the HV, MV or earth conductors. It is therefore necessary to develop both models and techniques which can characterize accurately the PD propagation mechanisms in each system and work out the frequency characteristics of the PD pulses at detection point, in order to design proper sensors able to carry out PD measurement on-line with maximum SNR.

It must be pointed out that particular attention is given, in general, to High Voltage systems since such apparatuses (transformers, cables, generators, motors, breakers, etc...) present significant costs in terms of both commercial value and maintenance. It is therefore necessary to invest in diagnostic techniques based on the actual condition of the system in order to sense any possible degradation process within the insulation, to analyze the degradation trend, to provide a complete and preventive diagnosis and, thus, reduce maintenance costs. Such diagnostic philosophy is commonly known as Condition Based Maintenance (CBM) which means to monitor the insulation system conditions and carry out maintenance only if required. Such an investment for diagnosis, which is generally afforded for HV systems, can not always be economically viable for MV systems, due to their significantly lower costs.

However, in the last ten years, attention was focused also to MV systems, which constitute the main framework of the electric distribution systems, both in the industrial and civil ambit. Medium Voltage apparatuses (cable, transformer, switchgear, motor) have costs definitely lower than those HV and, sometimes, their costs are even comparable to that of a PD detection instrument. It is therefore necessary to find out smart techniques, economically viable, able to carry out proper diagnosis on MV systems. As a matter of fact, if each MV apparatus is considered as a node of a network where several systems are interconnected and whose global commercial value is comparable to one HV single system, it is possible to figure out that a smart investment on diagnostic could be affordable and advantageous.

Indeed, economic advantages are appreciable when it is possible to consider only one detection instrument able to assess the insulation condition of several apparatuses having different characteristics. As an example, transformers and switchgears can be connected at cables ends. Hence, an effective instrument should be able to detect PD pulses in all the three systems, even if they have different characteristics and, thus, different optimum bandwidths. Beside the economical advantage, there are also many technical benefits. Using the same detection unit for different systems it is

possible to correlate the acquired data and localize the PD source on-line. As a matter of facts, PD sources located in one apparatus (e.g., in a MV cable) can propagate to the other systems (e.g., transformers etc...) and be recorded in several different detection points. As an example, when on-line PD measurements are carried out, it can happen that PD coming from other apparatuses can be detected in the equipment under test, misleading the diagnosis. Therefore, in order to achieve accurate PD source localization and correct diagnosis, it should be possible to perform measurements in all the systems connected in the same line.

The best compromise in terms of costs and accuracy is represented by the permanent installation of sensors in each MV apparatus. Then, using the same PD detection unit it is possible to carry out a screening of the system, connecting the instrument to the each sensor. After the acquisition of the PD pulses in each apparatus, the data can be analyzed, the results correlated and PD sources localized. Only if critical situations are found, continuous monitoring can be run.

This smart solution requires very good knowledge of the systems under test, in order to

- design proper sensors resorting to the optimum detection bandwidth for each apparatus;
- design proper PD acquisition instruments to be fitted with all the different sensors and providing results which can be correlated for localization purposes.

To start with, PD propagation has to be investigated in detail in MV systems in order to design proper sensors. Analytical models have to be devised in order to predict PD propagation in MV apparatuses. Furthermore, simulation tools can be used where complex geometries make analytical models to be unfeasible.

In the following work, PD propagation in MV cables, transformers and switchgears will be investigated, taking into account both irradiated and conducted signals associated to PD events.

Chapter 1

PD propagation and detection in Medium Voltage cables

1.1 Premise

Fundamental concerns associated with PD measurements in HV cables are, typically, maximum length that can be scanned to achieve a certain measurement sensitivity and measurement system bandwidth.

IEC 60270 gives indications about to the choice of wide- and narrow-bandwidths detectors that should be used to perform PD measurements [1]. Within those bandwidths, separation and location of PD sources cannot be achieved generally, because most of the frequency spectrum of the PD pulses is filtered out. Another class of detectors, called Ultra-Wide Bandwidth (UWB), can be preferred to capture more information about PD pulses, capturing also their high frequency content. These detectors may have the lower cutoff frequency lying in the same region of IEC-compliant ones (i.e. 100 kHz) and the upper frequency in very high frequency region (e.g. up to 50-100 MHz). Thus, if cable length and distance between each accessory are known, together with cable attenuation characteristic, level and frequency content of noise, it is possible to single out the frequency band at which signal-to-noise ratio (SNR) is the highest and, thus, to perform optimum detection.

It is, therefore, of utmost importance to develop techniques able to extract cable properties and find the frequency attenuation and dispersion, as a

function of the distance of PD pulse propagation, for every kind of cable. In the following paragraphs, methods able to calculate propagation constants in power cables are investigated and compared, and an approximate, but accurate, model is proposed for MV extruded cables.

1.2 Extraction of cables propagation constant

Three different methods are used in the forthcoming paragraphs to extract the propagation constant of a MV cable.
The device under test is a 2 meter-long splice of 20 kV EPR cable with aluminum conductors and a metallic screen made up of copper wires. Between the conductors and the insulation layer there are two semiconductive layers. An external PVC layer is used to cover the whole cable (see Fig. 1.1). The geometric characteristics of the cable under test are collected in Table 1.1.

TABLE 1.1 Cable characteristics

Outer radius of core conductor (mm)	8.2
Inner radius of main insulation (mm)	9.2
Outer radius of main insulation (mm)	13.0
Inner radius of shield conductor (mm)	14.0
Outer radius of shield conductor (mm)	14.8
Outer radius of outer insulation (mm)	17.3
Core resistivity (Ωm)	2.65e-8
Sheath resistivity (Ωm)	1.72e-8
Main insulation real permittivity	2.8

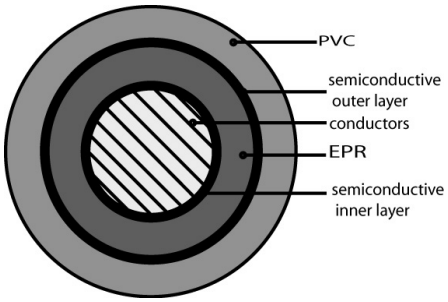

FIGURE 1.1 Device under test: 20 kV cable section.

1.2.1 Time Domain Reflectometry method

Time Domain Reflectometry (TDR) is a technique widely used to extract transmission line parameters. One common application is the prediction of an unknown load connected at the end of a transmission line having known characteristics. Indeed, when an incident step waveform traveling through a transmission line finds a discontinuity, a step wave is reflected back and can be detected at the measurement point. Resorting to the characteristic of the reflected wave, such as amplitude, rise-time, fall-time etc… it is possible to figure out the load impedance and parameters. Furthermore, in MV and HV applications, TDR techniques allow PD localization to be carried out when the cable length is known. At last, instruments based on TDR are largely used from MV utility to localize the joints between cables. Once the propagation speed along the cable under test is known, the time elapsed between the injection of the incident wave and the reception of the reflected one may provide an indication about the distance between sending end and discontinuity, i.e., the joint.

In order to estimate power cable attenuation characteristics through TDR, the spectral characteristics of a traveling pulse and his reflections can be evaluated [2, 3]. In particular, a voltage pulse, *V1*, is injected at sending end of the cable (open ended) and its reflection, *V2*, is recorded, again at the sending end, by a Digital Sampling Oscilloscope (DSO). If *L* is the length of the cable, *V2* returns at the sending end after propagating through a length 2*L*. Thus, equation (1.1) can be used to estimate the cable propagation constant, γ, by comparing the Fourier transform (FFT) of the two pulses.

$$\gamma = \alpha + j\beta = \frac{1}{L}\ln\frac{FFT(V1)}{FFT(V2)} \tag{1.1}$$

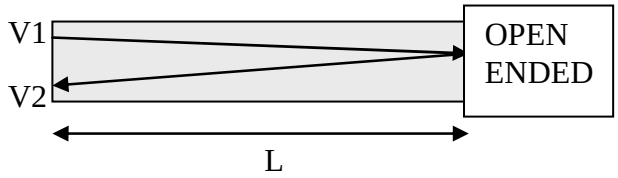

FIGURE 1.2 TDR measurement: injected and reflected pulses are detected at the same point and their relevant Fast Fourier Transforms are calculated and compared.

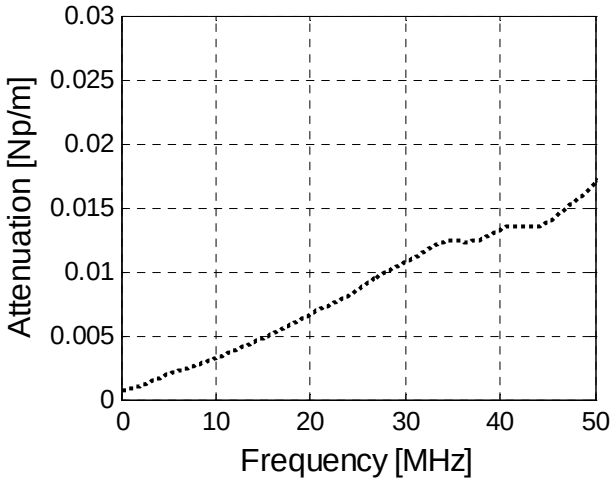

FIGURE 1.3 Cable attenuation obtained from TDR measurement

It must be considered that if the cable is too long, attenuation can be strong enough to prevent measurement of reflected pulses with adequate signal-to-noise ratio (SNR). In practice, attenuation can be estimated accurately up to the frequency of which the reflected pulse spectrum becomes indistinguishable from noise. To estimate accurately the propagation constant in a wide range of frequencies, some practices can be adopted. The injected pulse must be very fast (rise time of 1 or 2 ns, possibly) and with large peak value at the sending end. In addition, the sample of the cable under test must be chosen short enough to allow large frequency components to be reflected back with enough energy to be detected above noise.

1.2.2 Scattering matrix method

A single-core medium voltage cable can be represented as a coaxial transmission line, which is described by the propagation constant γ and characteristic impedance Z_0 (1.2). The real part of γ (1.3) is the attenuation constant α, expressed in dB/m, whereas the imaginary part is the phase constant, β, expressed in rad/m.

$$Z_0(\omega) = \sqrt{\frac{R + j\omega L}{G + j\omega C}} \tag{1.2}$$

$$\gamma(\omega) = \alpha(\omega) + j\beta(\omega) = \sqrt{(R + j\omega L)(G + j\omega C)} \tag{1.3}$$

Suppose to connect a transmission line to a load with known impedance Z_L. The solutions of the coupled ordinary differential equation obtained from Telegrapher's equations are:

$$V(z) = V^+ e^{-\gamma z} + V^- e^{\gamma z} \tag{1.4}$$

$$I(z) = I^+ e^{-\gamma z} + I^- e^{\gamma z} \tag{1.5}$$

where $z=d$ is the initial point of the transmission line, which is distant d from the load, and $z=0$ is the end of the cable, terminated by Z_L. Therefore, the input impedance seen at the start of the transmission line, terminated by the load, is:

$$V(z) = V^+ e^{-\gamma z} + V^- e^{\gamma z} \tag{1.6}$$

$$Z_{IN}(d) = \frac{V(d)}{I(d)} = Z_0 \frac{Z_L + Z_0 \tanh \gamma d}{Z_0 + Z_L \tanh \gamma d} = Z_0 \frac{1 + \Gamma_L e^{-2\gamma d}}{1 - \Gamma_L e^{-2\gamma d}} \tag{1.7}$$

where d is transmission line length, Z_0 is transmission line characteristic impedance, γ is line propagation constant and Γ_L is reflection coefficient of the load.

If the cable is terminated with an open circuit, we can consider $Z_L = \infty$ and we obtain (1.9), while if the cable is short circuited then $Z_L=0$ and we obtain (1.10).

$$\Gamma_L = \frac{Z_L - Z_0}{Z_0 + Z_L} \tag{1.8}$$

$$Z_{IN} = Z_{OC} = \frac{Z_0}{\tanh \gamma d} \tag{1.9}$$

$$Z_{IN} = Z_{SC} = Z_0 \tanh \gamma d \tag{1.10}$$

The propagation constant γ and the characteristic impedance Z_0 can be derived from (1.9) and (1.10) as shown in (1.11) and (1.12):

$$\gamma = \frac{1}{d} \tanh^{-1} \sqrt{\frac{Z_{SC}}{Z_{OC}}} \tag{1.11}$$

$$Z_0 = \sqrt{Z_{SC} Z_{OC}} \tag{1.12}$$

Therefore, if the input impedance Z_{IN} of a cable is known for both a short circuited end and an open end, it is possible to work out both the propagation constant and the characteristic impedance of the cable using (1.11) and (1.12).

A method generally used for determining Z_{OC} and Z_{SC} impedances of a transmission line is based on the extraction of the reflection coefficient S11 of the line.

$$S11 = \Gamma_{IN} = \Gamma_L e^{-2\gamma d} \tag{1.13}$$

By measuring S11 through a proper Network Analyzer (NA) and using (1.13) and (1.7) it is possible to determine the input impedance of the cable [4-7]. S11 parameter is measured in two conditions: open (the cable is open circuit terminated) and short (the cable is short circuited). In this case we have:

$$Z_{OC} = 50 \frac{1 + S11_{OC}}{1 - S11_{OC}} \tag{1.14}$$

$$Z_{SC} = 50 \frac{1 + S11_{SC}}{1 - S11_{SC}} \tag{1.15}$$

where 50 (expressed in Ω) is NA port impedance and $S11_{OC}$ and $S11_{SC}$ are S11 parameters, measured in open and short conditions.

Alternatively, connecting the Equipment Under Test (EUT) to both ports of Network Analyzer, the scattering matrix can be determined, where S11 is

reflection coefficient at port 1 and S21 is transmission coefficient from port 1 to port 2.
Cable characteristic parameters can be derived from:

$$\gamma = \frac{1}{d}\cosh^{-1}\sqrt{\frac{1-S11^2+S21^2}{2S21}} \tag{1.16}$$

$$Z_0 = 50\sqrt{\frac{(1+S11)^2-S21^2}{(1-S11)^2-S21^2}} \tag{1.17}$$

An Agilent Network Analyzer 4396B was used for S-parameters evaluation. The investigation was carried out within the frequency range 300 kHz to 100 MHz on a piece of cable 0.5 m long.
To reduce geometrical discontinuities and phase shift effect, a cable adapter is realized, Fig. 1.4, which permits to connect the cable directly to NA ports.

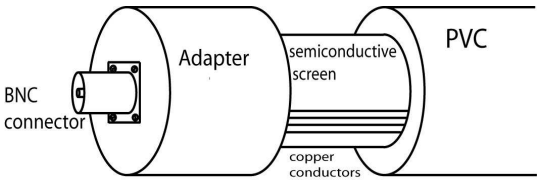

FIGURE 1.4 Cable adapter realized to minimize geometrical discontinuities

The measurement setup is shown in Fig. 1.5, that is, a cable splice with adapters connected to port 1 of the NA measuring system.

The application of the two adapters at cable termination may introduce measurement errors due to three causes: (1) the cable under test and its adapters present a complex combination of geometrical and material changes which may lead to an impedance mismatch especially over the high frequency range; (2) connections may be represented by discrete series impedance and shunt admittance, which modify electrical parameters of EUT; (3) phase shift error due to BNC connectors.

To minimize these errors, Network Analyzers are generally endowed with a special function, called Port Extension, which is a post-calibration procedure that allows to virtually extend the port up to the beginning of the cable, in order to virtually bypass the adapter and reduce phase shift errors. Therefore, after the classical N-Type calibration (i.e., open circuit, short circuit and load calibration using N-Type connectors), only the adapters are

connected to Port 1 without the EUT and the phase is set to zero at all frequencies. In such a way the phase error introduced by the adapter is prevented. Then, the EUT is connected to the adapter and S11 is extracted. This procedure allows the electrical characteristics of adapters to be taken into account, thus improving propagation constant and characteristic impedance evaluation.

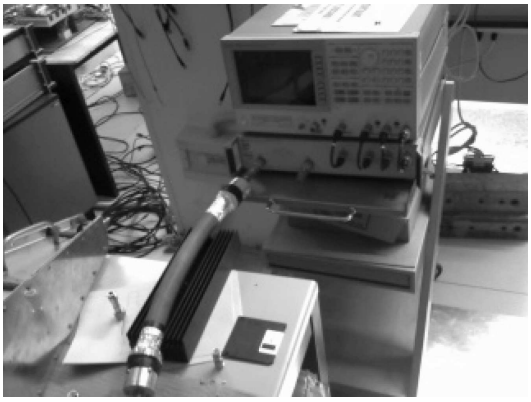

FIGURE 1.5 Measurement set up.

Figures 1.6 and 1.7 show the measurement results (propagation constant and characteristic impedance, respectively), with and without the port extension procedure. As can be seen, using the port extension procedure permits ruling out resonance phenomena associated with imperfect cable terminations. Notwithstanding all devices, measurement results show a random ripple at frequencies below approximately 10 MHz. This ripple can be addressed to an internal damage of the instrument, due to a failed low frequency amplifier of the RF output channel. It can be noticed in Fig. 1.6 and 1.7 that whenever phase constant is zero, both attenuation constant and characteristic impedance present a peak, associated with resonance and anti-resonance phenomena. These peaks were explained as above by inductive and capacitive stray parameters due to the adapters. As can be seen, the port extension procedure reduces noticeably these phenomena.

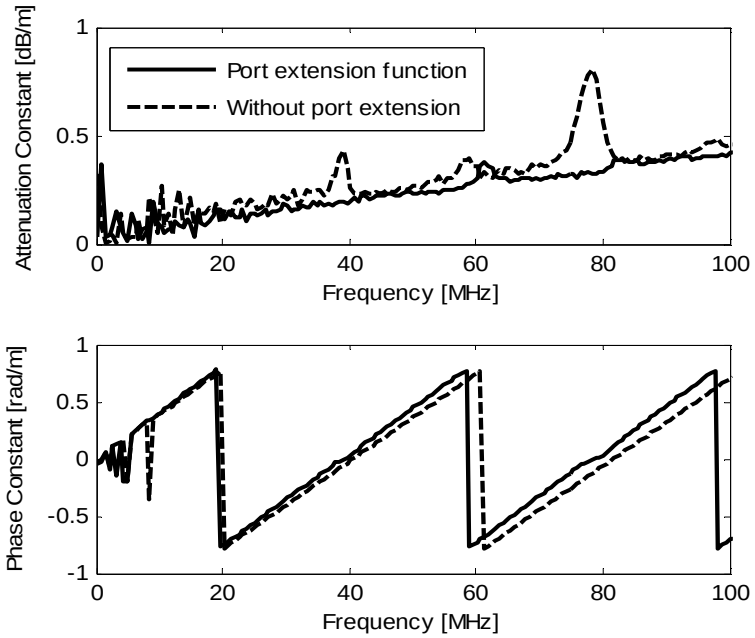

FIGURE 1.6 Propagation constant derived from one-port measurements (S11) with and without port extension procedure.

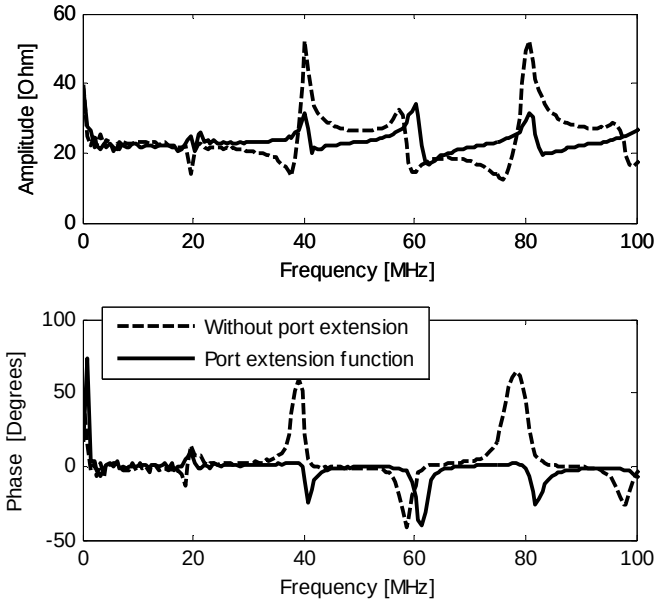

FIGURE 1.7 Characteristic impedance derived from one-port measurement (S11) with and without port extension procedure.

. *1.2.3 Determination of cables propagation constant through analytical models*

A few analytical models have been already developed and investigated to achieve mathematical tool suitable to characterize power cables up to hundreds of MHz and, therefore, simulate PD pulse propagation [7-14]. These models can be very useful to highlight the influence on propagation constant characteristics of cable materials properties. By the use of the analytical expressions developed in [4] and [8-15] two features have been made clear:

1. The main cause of attenuation in power cables at frequencies below 1 MHz is associated with skin effect losses in core and sheath [14]. Attenuation, therefore, is affected mainly by the geometric characteristics of the cable.
2. At higher frequencies, the attenuation is due mainly to the radial displacement of the capacitive current through the semiconductive layers, but it can be affected also by the interaction between the ground shield and the strands in the sheath [14].

In 1982 a model has been developed by Boggs and Stone [4], which is based on the calculation of longitudinal impedance and parallel admittance of the cable, taking into account frequency dependence, skin effect and semicon influence (Figure 1.8).

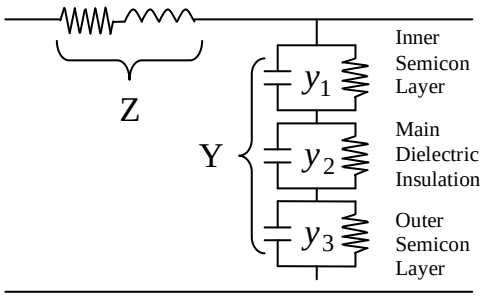

FIGURE 1.8 Equivalent circuit for an extruded power cable: the longitudinal impedance, Z, includes skin effect, while the parallel admittance, Y, includes losses due to insulation and semiconductive layers. All parameters are frequency dependent.

In order to evaluate correctly the parameters of this model it is necessary to know cable geometry and characteristics of each material as, e.g., insulation and semicon complex permittivity. While dielectric permittivity

can be assumed as frequency-independent up to some hundred of MHz [15] in polymeric cables, data on semicon complex permittivity are not available, in general, in literature, so that laboratory measurements have to be done.

This represents an important issue since all the analytical models which can be found in literature need the knowledge of semicon permittivity, which means that they are applicable only in laboratory, where it is possible to cut a sample of semicon and extract its permittivity. It will be thus aim of this work to find out an analytical method which can also be applicable on field and without cutting any piece of cable material.

In order to work out such a model, few samples of semicon were cut and the complex permittivity was extracted as suggested in [5,6] through the Network Analyzer, in order to try the existing methods. The obtained value of permittivity must be inserted in the equation 1.18, then modelling the frequency dependence of the shunt admittance, Y through 1.19:

$$y_k = j\omega C_{0k}\varepsilon_k^*(\omega) = j\omega C_{0k}(\varepsilon_k^{'}(\omega) - j\varepsilon_k^{''}(\omega)) \tag{1.18}$$

$$Y = \left(\sum_{k=1}^{3} y_k^{-1}\right)^{-1} \tag{1.19}$$

where C_{0K} and ε_k^* are, respectively, the geometrical capacitance and the complex permittivity of the k-layer (k=1, 2, 3 where: layer 1 and 3 are semicon layers, layer 2 is the dielectric).

The longitudinal impedance can be then calculated as:

$$Z = \frac{1}{2\pi R_{in}}\sqrt{j\omega\mu_0\rho_1} + \frac{1}{2\pi N R_S}\sqrt{j\omega\mu_0\rho_S} + \frac{j\omega\mu_0}{2\pi}\ln\frac{R_{out}}{R_{in}} \tag{1.20}$$

where R_{in} and ρ_1 are the radius of center conductor and its resistivity, respectively, R_S is the radius of each copper wire in the metallic sheath, N is the total number of copper wires, ρ_S is copper resistivity, R_{out} is the radius to the center of metallic sheath.

Eventually, the propagation constant γ is evaluated as:

$$\gamma = \alpha + j\beta = \sqrt{ZY} = \sqrt{(r + j\omega l)(g + j\omega c)} \tag{1.21}$$

The propagation constant obtained applying this method on the EPR-insulated MV power cable of Table 1.1 is reported in Figure 1.9.

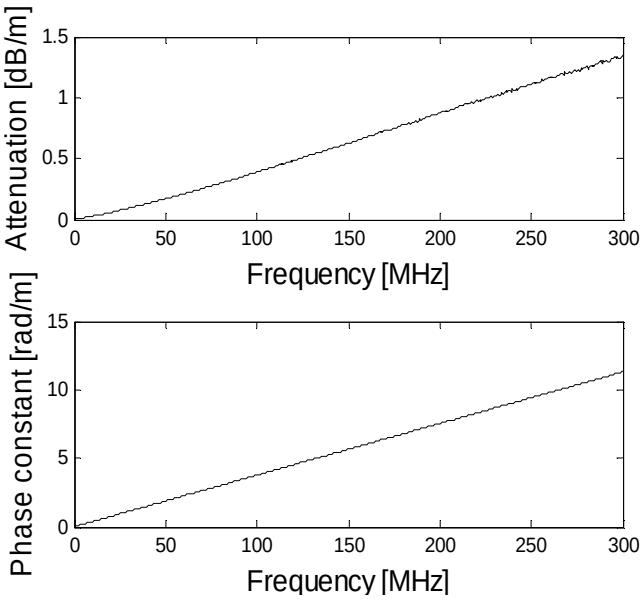

FIGURE 1.9 Attenuation and phase constant of an extruded MV cable obtained through the analytical model (equations 1.18-1.21).

In order to validate the model, pulses were injected in the EUT and detected by a DSO at the sending and receiving ends. The propagation of an injected pulse was simulated through the model and the results compared with experimental data.

As emphasized in Figures 1.10 and 1.11, the model is able to provide a very good prediction of traveling pulses in both time and frequency domain.

As confirmed by experimental results, the propagation constant evaluated by the above-described analytical model describes very well the pulse propagation characteristics along a cable. Figure 1.12 shows that the attenuation constant obtained by the TDR method fits well the analytical attenuation, but only up to 30 MHz.

This can be explained recalling that the EUT is 260 m long, thus frequency components above 30 MHz of the reflected pulse are strongly attenuated (making SNR very poor), thus attenuation constant estimated can be affected by significant error.

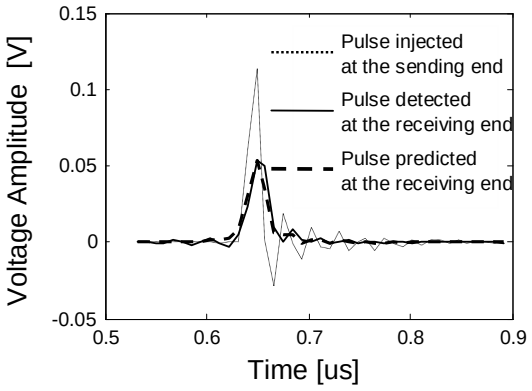

FIGURE 1.10 Predicted and experimental pulse detected at the receiving end in an EPR cable (Table1) 260 m long. Time domain.

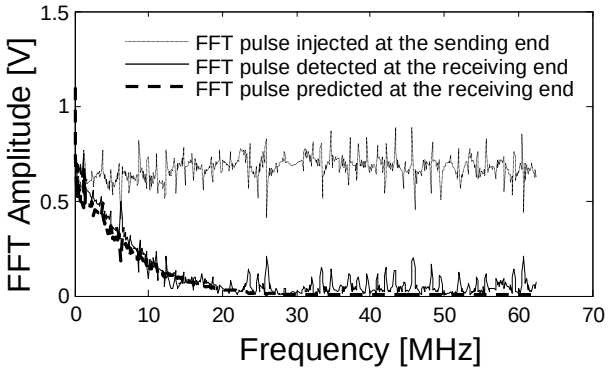

FIGURE 1.11 Predicted and experimental pulse detected at the receiving end in an EPR cable (Table1) 260 m long. Frequency domain.

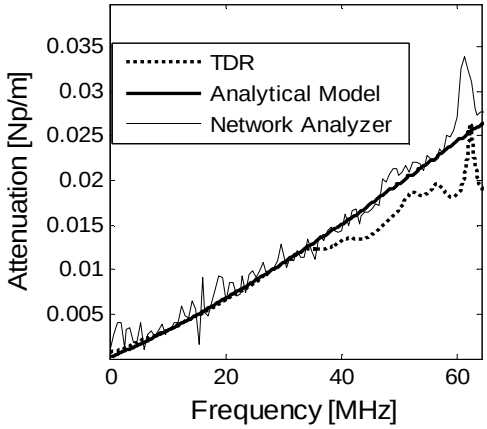

FIGURE 1.12 Comparison between the attenuation coefficients obtained through TDR, Network Analyzer and analytical model techniques.

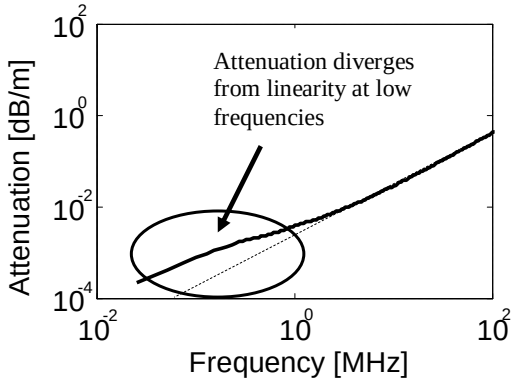

FIGURE 1.13 Attenuation displays non linear dependence on frequency below 1 MHz.

Summarizing the above considerations:

- The analytical expressions (1.18-1.21) fit very well the propagation properties of a power cable. The measurement of semicon permittivity is however necessary.
- TDR technique describes accurately propagation properties in the low frequency (0-30 MHz) range.
- NA techniques can describe accurately the cable attenuation, but it must be considered that NA measurements are very complex. The accuracy of this technique depends mainly on the quality of the open and short terminations and special adapters are required to minimize the geometrical discontinuities between the cable and the instrument. Furthermore, these kinds of instruments are very costly and not readily available in many labs.
- Attenuation and phase constants display a quasi-linear dependence on frequency, except for frequencies below 1 MHz where the attenuation has a non linear behavior, as shown in Fig. 1.13.

1.4 Determination of cable propagation constant through approximate analytical model

The complex nature of equations (1.18) - (1.21) may prevent from understanding in straightforward way propagation phenomena. Alternatively, if some parametric representation of attenuation and dispersion constants could be found, a more intuitive approach could be sought. Indeed, looking

at Figures 1.9, 1.12 and 1.13, it comes out that both attenuation and phase constants display a very small non-linear dependence on frequency for frequencies above 1 MHz (below 1 MHz, the skin effect can be predominant, and the behaviour of attenuation and dispersion constant as a function of frequency can become strongly non linear [13]). Thus, in order to provide an approximate, but still meaningful description of propagation phenomena, a linear approximation of propagation constant could be considered.

Attenuation constant

In preview works, the attenuation was already considered linear with frequency explaining that this behavior is “normal for solid dielectrics used in power cables at frequencies above 1 MHz” [16]. Thanks to equations (1.18)-(1.21) and to TDR measurements, it has been possible to characterize the cable under test and confirm the predominant behavior of skin effect with respect to the dielectric losses below 1 MHz.

It must be observed that such strong predominance of skin effect might not be generalized, as it can depend on cable manufacturing. Indeed, it may happen sometimes that attenuation could behave quite linearly also below 1 MHz. Anyway, for extruded medium voltage cables having characteristics similar to those reported in Table 1.1 and in [12-13], an approximate attenuation characteristic, that is non-linear up to 1 MHz and then linear with frequency, could be developed.

In order to model attenuation in a approximate, but simple way, attenuation constant can consider skin effect only, thus neglecting semicon losses (and getting rid of both measurements of this quantity, which can change cable by cable depending on manufactures) up to 1 MHz, using equations (1.18)–(1.21), while, above 1 MHz the attenuation constant can be approximated using a straight line that links two points:

- Point P1: value of attenuation at 1 MHz obtained by the above approximation.
- Point P2: Perform a TDR measurement with a very fast pulse (rise time less than 2 ns), choose the frequency range, above 1 MHz, where SNR is sufficient to obtain an accurate estimate of the reflected pulse spectrum and calculate an attenuation value within this frequency range.

The comparison between the results provided by model [3,4] (referred in the following to as the analytical model) and the linear approximation

obtained through the above procedure it is shown in Figure 1.14. The attenuation calculated through TDR measurement was accurate enough from 1 MHz up to about 30 MHz (see Figure 1.12), thus the second point, P2, was chosen within this range (i.e., 10 MHz). The figure emphasizes, in fact, that there is a good agreement in the 0-30 MHz range (relative error below 6 %).

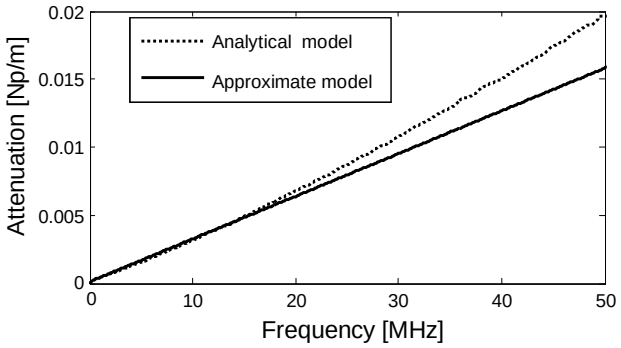

FIGURE 1.14 Comparison between the attenuation constants obtained through the linear approximation and the analytical model [13]. The two characteristics are in good agreement for frequencies below 20 MHz (relative error at 20 MHz = 6%).

Some considerations must be done concerning the choice of P2. As attenuation is not perfectly linear, but it shows a slight upwards concavity (see Fig. 1.14), if the second point lies in a frequency region between 5 and 30 MHz, the approximate linear model is closer to the analytical one at low frequencies, but approximation error increases with frequency.

On the contrary, if the second point lies in a frequency region higher than 30 MHz, the linear approximation tends to overestimate the values in the 1-30 MHz range.

Thus, in order to choose P2, it can be useful to see how the frequency components of an ideal pulse propagating along a cable are attenuated as a function of distance propagated (see Figure 1.15). If reference is made to an attenuation of 20 dB (i.e. 90%), the component at 10 MHz travels 800 m, that at 50 MHz travels 100 m, while the component at 100 MHz travels only 30 m. This means that as high frequencies can be completely attenuated after a few tens of meters, it is preferable to have the best fit at low frequencies, thus choosing P2 in a frequency range that can be considered reasonably between 5 and 20 MHz.

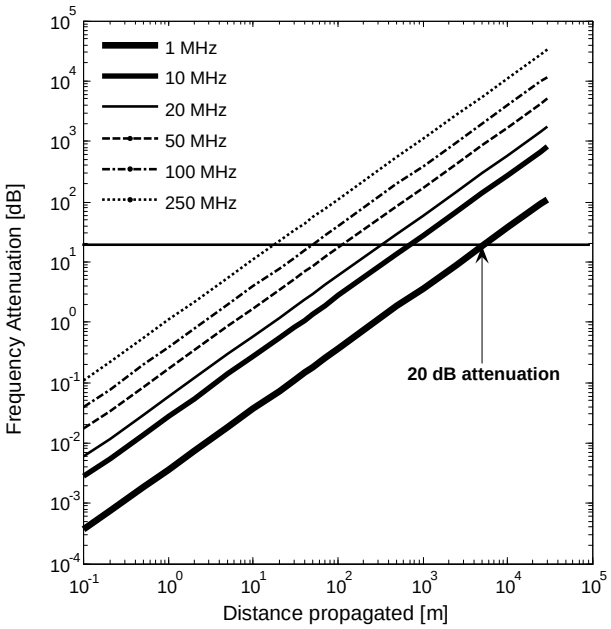

FIGURE 1.15 Attenuation (in dB) of the pulse frequency components as a function of the distance for the extruded MV power cable under test, obtained by the analytical model. As an example, the component at 20 MHz travels only 300 m.

To evaluate the accuracy of the linear approximation in predicting PD pulse peak voltages, a simulation was done applying both analytical and approximate models.

The voltage peak, V_d, of a pulse propagated after a given distance, d, can be calculated as:

$$V_d = \max\left|F^{-1}\{V_0(\omega)\exp(j\gamma_{\mathrm{mod}}(\omega)d)\}\right| \qquad (1.22)$$

Where γ_{mod} is the propagation constant obtained by the chosen model, F^{-1} is the inverse of the Fourier Transform and $V_0(\omega)$ is the Fourier transform of the starting pulse $V_{d=0}$, having amplitude and rise time equal to 1 V and 1 ns, respectively.

Figure 1.16 shows how peak voltage value decreases with the distance between the PD source and the detection point. This figure emphasizes that there is an excellent agreement except in the first 100 m of cable, where the linear approximation provides a slight overestimate. This can be explained recalling that the linear approximation underestimates frequency components larger than about 20 MHz (see Figure 1.14). These components, however,

suffer a very large attenuation in the first 100 meters of propagation (see Figure 1.16). Thus, the shape of pulses obtained through the approximate and analytical models are practically the same after 100 m.

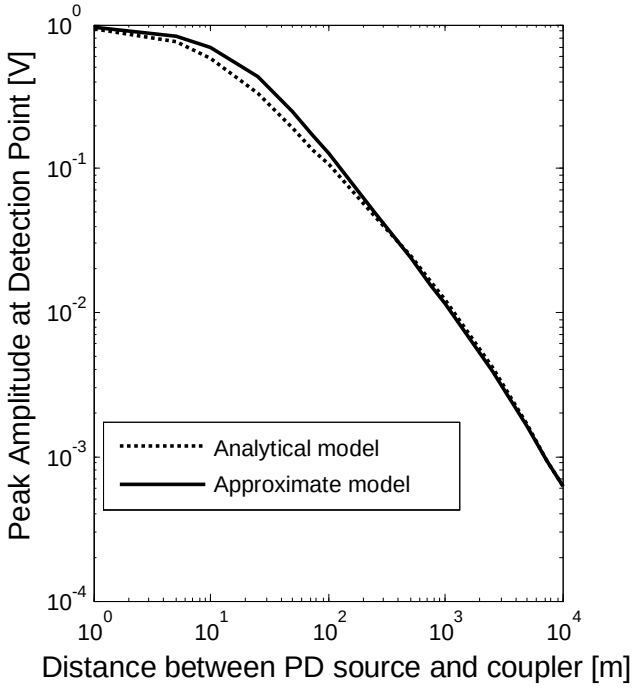

FIGURE 1.16 PD pulse peak voltage as a function of distance propagated (calculated using approximate and analytical model). Peak voltage at the source is 1 V.

Focusing on the objective of characterizing attenuation phenomena in power cables, that is, searching for the best detection bandwidth to perform PD detection and localization, it is appropriate to unravel the meaning of the optimum detection bandwidth, which, for a known PD pulse, can be defined as the frequency region where the most of the PD signal frequency content can be detected achieving an high SNR.

The best theoretical solution in PD detection is given likely by the use of matched filters. A good value of SNR may be achieved choosing a filter transfer function that matches the spectrum of a PD pulse [17]. However, such filters are often difficult to realize in practice. For PD-like Gaussian pulses overlapped to white noise, the advantages coming from the use of a rectangular filter of optimum bandwidth are very close to those obtained through matched filters [17].

Therefore it is necessary to develop a simple method able to indicate, for every PD pulses, the frequency region that best highlight the PD signal frequency behavior.

In previous works, [16] and [18], Boggs assumed that the frequency spectrum behavior of a PD pulse in the – 6 dB bandwidth can indicate approximately the optimum bandwidth. In this paper, the optimum detection bandwidth will be considered equal to the equivalent bandwidth, F, which represents the standard deviation of a PD pulse in the frequency domain. This quantity provides a direct, intuitive representation of the frequency properties of the detected signals. To evaluate F, the PD pulse energy must be normalized to 1 (so that F becomes scale-invariant):

$$\tilde{x}(t) = \frac{x(t)}{\sqrt{\int_0^L x(\tau)^2 \, d\tau}} \tag{1.23}$$

being *x(t)* the recorded pulse, *t* time and *L* the time length of the observation window.

Then, the equivalent bandwidth is calculated as

$$F = \sqrt{\int_0^\infty f^2 \left|\tilde{X}(f)\right|^2 df} \tag{1.24}$$

where $\tilde{X}(f)$ the Fourier transform of the normalized PD pulse $\tilde{x}(t)$. The equivalent bandwidth, *F*, is already used in [19-20] to reject noise and disturbance, to separate PD pulses associated with different sources and to locate PD in cable systems.

Figure 1.17 emphasizes the optimum detection bandwidth, calculated by equations (1.23) and (1.24), for a symmetric PD pulse having a rise time of 1 ns and propagated in the cable described in Table 1.1, as a function of the distance between the PD source and the coupler. The differences between the optimum bandwidth calculated using the exact ad approximate models are small and for distances longer than 100 m are negligible.

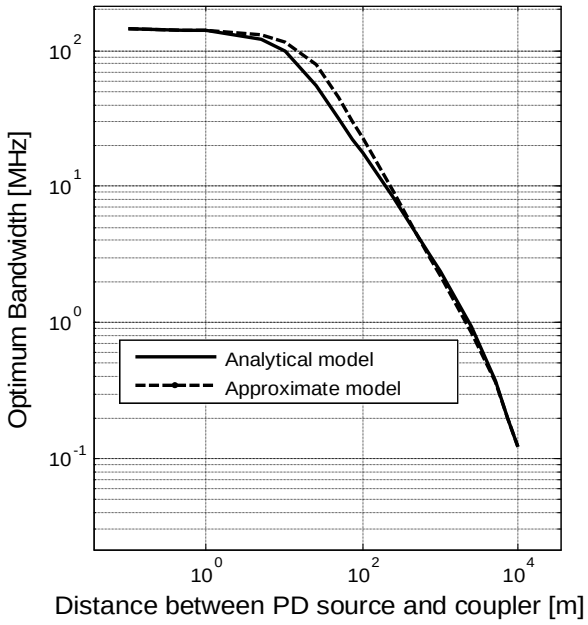

FIGURE 1.17 Optimum detection bandwidth: the high frequencies attenuation in power cable causes a reduction of the optimum bandwidth as a function of the distance propagated. The approximate linear attenuation fits well the exact attenuation.

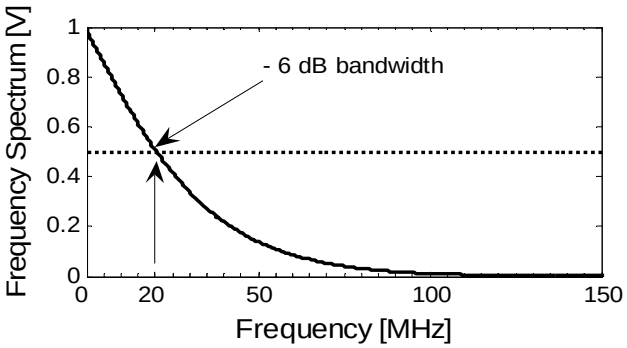

FIGURE 1.18 The – 6 dB bandwidth for a pulse propagated after 100 meters is equal to 20 MHz. The equivalent bandwidth (Figure 1.17) and the – 6 dB bandwidth are in good agreement.

As shown in Figures 1.17 and 1.18, after a propagation of 100 m PD pulses have an equivalent bandwidth equal to about 20 MHz, that corresponds also to the – 6 dB bandwidth at such distance.

Phase constant

In a lossless system the phase constant, β, is linear with frequency, which means that each frequency component travels along the line with the same speed, thus preserving the shape of the traveling signal (see Figure 1.19).

Equation 1.25 can be used to calculate β, where phase velocity, ν, is assumed to be frequency-independent.

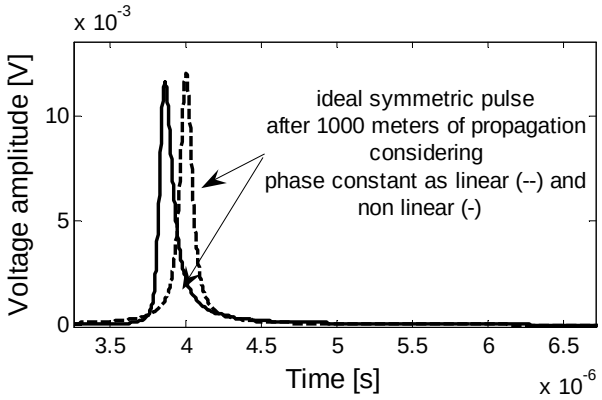

FIGURE 1.19 The non-linearity of phase constant β with the frequency is the cause of shape distortion in traveling pulses. This figure shows the comparison between the shape of two pulses considering phase constant as linear and non-linear: the first pulse (--) is the result of the propagation of an ideal symmetric pulse considering the phase constant linear with the frequency; its shape is preserved and after 1000 meters it is still symmetric. The second pulse (-) is the result of the propagation of the same symmetric pulse considering the phase constant as non linear with the frequency: after 1000 m, the shape is asymmetric because of the strong non linear behavior of the phase constant in low frequency region.

On the contrary, in lossy transmission lines, ν is frequency-dependent and the spectrum components of the signal travel with different velocity. This leads to a distortion of the signal and the phase constant is, in this case, non linear with frequency. Thanks to the analytical model, it is possible to separate the relative contribution of the different loss mechanisms on phase velocity. Neglecting the frequency dependence of longitudinal impedance (due to skin effect) and parallel admittance (mostly due to semiconducting layers), the phase velocity becomes constant with the frequency (Figure 1.20).

$$v = \frac{2\pi}{\beta} f \qquad (1.25)$$

Indeed, the presence of semiconducting layers causes a huge drop in phase velocity, while the skin effect phenomenon is the main cause of the strong non-linear behavior in the low frequency region (0-1 MHz, approximately).

Therefore, the main cause of shape distortion is not associated with dispersion phenomena occurring in the high frequency range, (where the phase velocity behaves almost linearly with frequency and the phase constant can be assumed frequency independent), but with those occurring in the low frequency region, where the strong non linear behavior associated with the skin effect has to be taken into account.

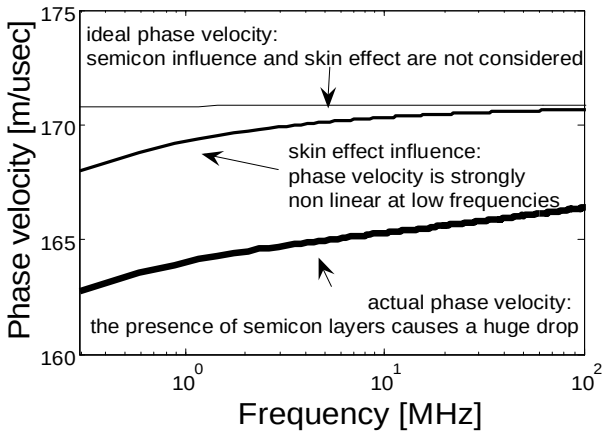

FIGURE 1.20 Comparison between the phase velocity behavior of the lossless line and that obtained keeping into account skin effect and semiconducting layers losses. The non-linearity in the low frequency region is mostly given by the skin effect phenomenon. The decrease of phase velocity is mostly due to the presence of semicon layers. In the high frequency region the phase velocity can be considered linear with the frequency.

Here a practical method is proposed to estimate the phase constant in an approximate way using both the analytical model and TDR measurement, assuming that the cable length is known with reasonable accuracy.

As the non-linear behavior in phase velocity at low frequencies is mainly caused by the skin effect phenomenon, the phase velocity of the cable is calculated by the analytical model neglecting the semicon layers influence.

Then, to consider the influence of semiconducting layers (that causes a drop in phase velocity), a TDR measurement is done to obtain the propagation speed of the cable: a fast pulse is injected into the cable and the

propagation speed, ν, is obtained dividing the time distance between the peaks of the injected and reflected pulse by two times the length of the cable.

The characteristic evaluated at point 1 is moved intersecting, at high frequencies, the value obtained by TDR measurement. Once that the parameter ν is calculated, it is feasible to evaluate β by the use of equation (1.25).

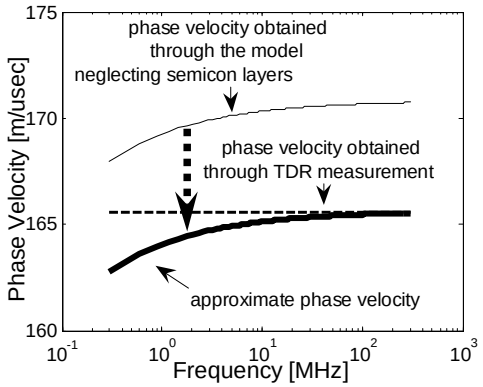

FIGURE 1.21 The phase velocity obtained by the exact model, neglecting the semiconducting layers, is strongly non linear at low frequencies and is the main responsible of the shape distortion of travelling pulses. In order to consider the semicon influence, the obtained characteristic must be moved down intersecting at high frequencies the value obtained from TDR measurement.

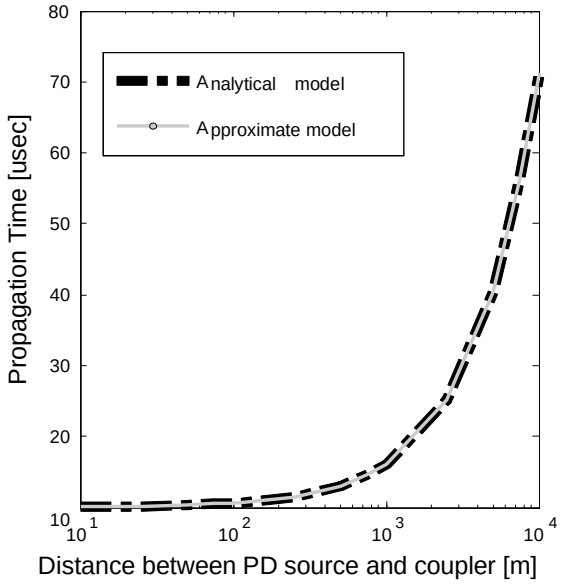

FIGURE 1.22 The propagation time of PD pulses, along the cable under test, evaluated through the approximate phase constant is coincident to that obtained by the analytical model.

The obtained characteristic was validated comparing the propagation time of a PD pulse (i.e. evaluating the time position of the peaks of the travelling pulses), as a function of the distance propagated, using the phase constants obtained by both models (i.e. exact and approximate): as emphasized in Figure 1.21, the results are in excellent agreement.

Another test was done simulating the propagation of an ideal symmetric PD pulse and observing the distortion of its shape using both models: the approximate model provides results that are again in excellent agreement with those obtained by the analytical model (see Figure 1.23).

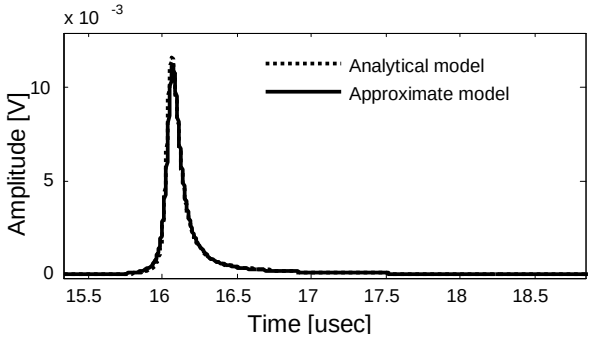

FIGURE 1.23 The shape distortion after a propagation of 1000 m evaluated with both models is the same.

1.5 Determination of cables optimum detection bandwidth

In order to show the effects of bandwidth on PD detection in power cables as a function of the distance between the PD source and the measurement point (traveled distance), analytical expressions for attenuation phenomena shall be obtained, which could allow PD pulse waveforms to be predicted in the time-frequency domain. Existing analytical models can be used for this purpose [4-8] in addition to the new approximate model developed in 1.4, based on the linear behavior with frequency of the propagation constant for frequencies above 1 MHz. The propagation constant, evaluated through said model, was thus exploited to highlight PD pulse propagation characteristics

for distances between 0 and 30 km in a MV cable having the characteristics reported in Table 1.1.

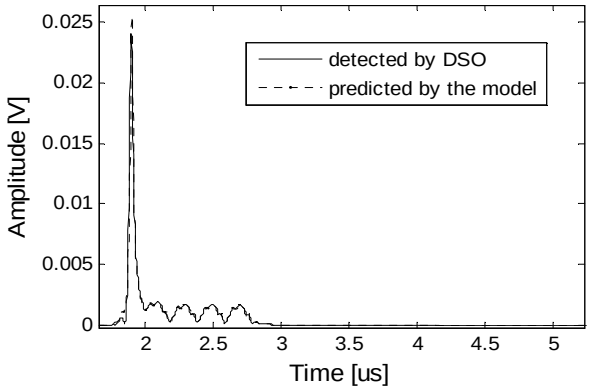

FIGURE 1.24 Validation test: a pulse is injected and detected at sending end of the cable under test (through a DSO), after a propagation of 280 m (two times the cable length). A propagation of 280 m is simulated through the model and the obtained pulses is compared to the detected one: the two results are in excellent agreement.

In the validation test, a pulse was injected at the sending end of the open-ended cable and its reflection was recorded by a Digital Sampling Oscilloscope (DSO). The propagation of the injected pulse and its reflection along the cable were then simulated by the use of an analytical model. As emphasized in Figure 1, the simulated reflected pulse is in excellent agreement with that recorded by DSO.

IEC standard 60270 gives recommendations about wide- and narrow-band measuring systems, indicating the bandwidth that can be chosen in order to perform apparent charge estimation. The action performed by filters conforming with the IEC standard, however, removes much information brought by the PD pulse, making localization, disturbances and noise rejection, and PD source separation practically impossible (here, noise are electromagnetic pulses not associated with PD, disturbances is associated with PD, but coming outside the equipment under test, EUT, and separation is the procedure of removing noise and disturbance from PD signals [17, 19, 20]). As an example, Figures 1.25 and 1.26 show, for different traveled distances, the time and frequency domain representation of a pulse having a rise time of 2 ns (thus having frequency spectrum amplitude constant at every frequency up to some GHz), filtered by a wide-band detector having

mid-band frequency at 300 kHz and a bandwidth of 400 kHz. The pulses show very small differences after propagation at distances of 10, 500 and 1000 m. Therefore, pulses coming from different distances with respect to the measurement point may show very similar waveform in time and frequency domain. In such way, any technique for separation and recognition of PD pulses coming from different sources cannot work properly.

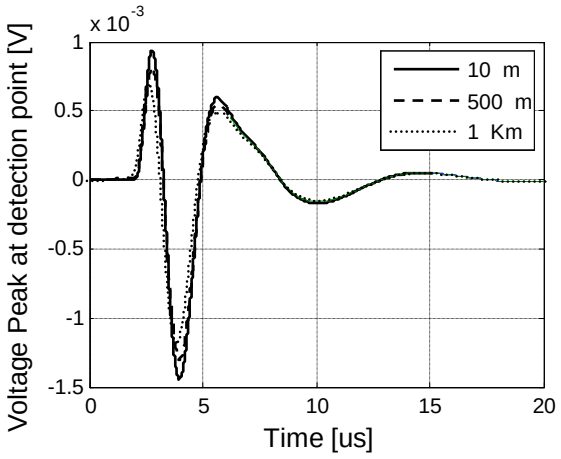

FIGURE 1.25 PD pulse detected using a wide bandwidth measurement system (100-500 kHz of bandwidth) after a propagation of 10, 500 and 1000 m. Time domain.

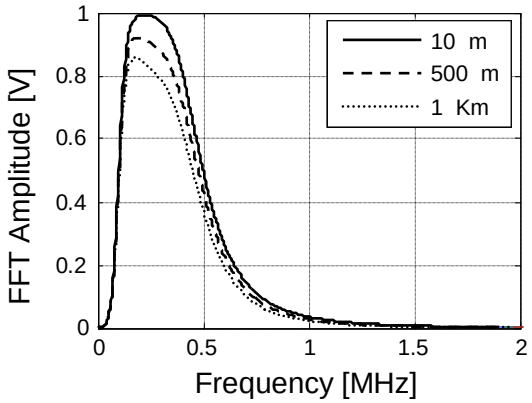

FIGURE 1.26 PD pulse detected using a wide bandwidth measurement system (100-500 kHz of bandwidth) after a propagation of 0, 500 and 1000 m. Frequency domain.

IEC 60270 detectors are not free from errors in apparent charge estimation associated with cable attenuation phenomena [7]. Indeed, as the voltage peak of PD signals decreases with the traveled distance, due to the

cable attenuation, pulses having the same charge, but coming from different PD sources, may show different charge value after filtering. As shown in [7], the apparent charge estimation is strongly dependent on the traveled distance, as well as on the choice of the detection bandwidth. Anyway, a discussion about the calibration and the charge estimation is still opened and will be addressed more explicitly in our next work.

According to IEC 60270, UWB detectors "do not directly quantify the apparent charge of PD current pulses". However, these detectors are characterized by higher sensitivity, particularly for near PD sources, and allow PD source location [20]. Moreover, when endowed with fast analog-to-digital converters and enhanced processing capabilities, they allow noise rejection and PD source separation [19-22]. Figures 1.27 and 1.28 emphasize that using an ideal UWB detector (i.e. having infinite bandwidth) the waveforms of pulses coming from, e.g., sources at 100 m of distance look very dissimilar in the time and frequency domain. Thus, it can be feasible to separate the two types of PD pulses through time-frequency transformation, allowing for noise and disturbances rejection, as well as for risk assessment to be performed on a PD source-per-source basis.

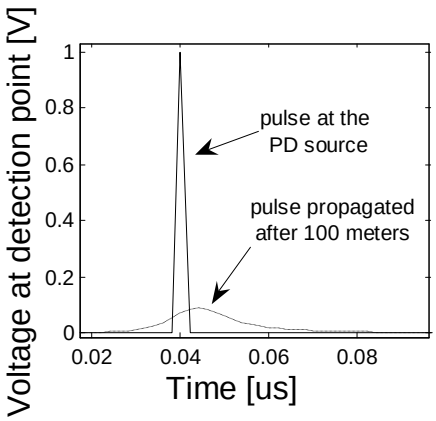

FIGURE 1.27 Effect of attenuation on pulse propagation in a MV power cable in time domain. After 100 m the pulse has a peak reduction of 90% and a large dispersion.

For UWB systems, PD detection sensitivity is closely related to the choice of the detector bandwidth and to the noise spectrum. Indeed, depending on noise characteristics, it could be quite difficult to detect signals coming from long distances since the frequency content of a pulse can

decrease from the GHz range to a few tens of MHz after traveling short distances (thus losing energy).

For example, in the presence of white noise having the amplitude shown in Figure 1.28, the frequency components above 50 MHz of a PD pulse 100 m far from the coupler are completely covered by the noise. This means that, choosing a detection bandwidth too large (e.g., higher than 50 MHz), the signal-to-noise ratio (SNR), defined as

$$(SNR)_{dB} = 10 \log \frac{\sigma^2_{x(t)}}{\sigma^2_{noise}} \tag{1.26}$$

where $\sigma^2_{x(t)}$ and σ^2_{noise} are the variance of the PD pulse and the noise respectively, could decrease and PD detection can be strongly compromised.

The dependence of optimum detection bandwidth on cable attenuation and cable circuit characteristics will be dealt with more detail in the following sections.

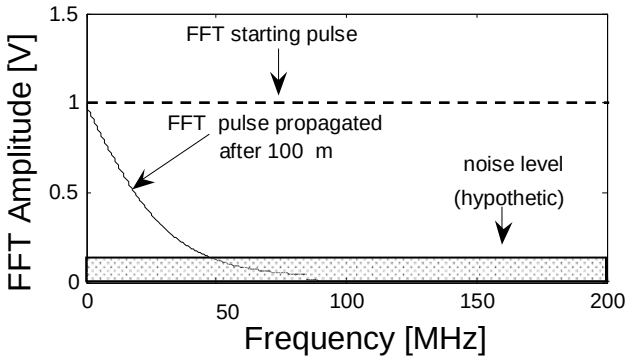

FIGURE 1.28 Effect of attenuation on pulse propagation in a MV power cable in frequency domain. After 100 m the pulse has lost most of its frequency content: e.g., the frequency components at 20 and 50 MHz are reduced to 50 % and 90 % respectively. In the presence of background noise as that depicted in the Figure, all the frequencies above 50 MHz are dominated by noise and SNR may decrease.

The bandwidth of a band-pass filter is defined as the difference between the upper and the lower cutoff frequencies of the filter itself. Assuming, for simplicity, that the lower cutoff frequency can be negligible if compared with the upper cutoff frequency (as it is customary in UWB pulse detection), the bandwidth corresponds to the upper cutoff frequency. For pulse

detection, the optimum bandwidth, Δf_{OPT}, is defined as the one which maximizes the SNR, thus detection sensitivity.

Ideally, in order to achieve the optimum detection sensitivity (highest SNR) it is necessary to employ filters having the transfer function that matches perfectly the PD pulse spectrum. This approach, however, works only in case of detection of deterministic signals, whose spectrum is known in advance. Alternatively, a good compromise between theory and practice is using rectangular filters having bandwidth that matches most of the frequency spectrum of a PD pulse [17,18]. The PD equivalent bandwidth, defined as the standard deviation of a PD pulse in the frequency domain, has been assumed in 1.4 to give a quantitative representation of the frequency content of the detected PD pulses. Therefore, rectangular filters having bandwidth equal to the pulse equivalent bandwidth can be considered as a good approximation of a matched filter and the equivalent bandwidth can be considered as the optimum one and evaluated using (1.23) and (1.24).

In literature, some proposals for the choice of PD detection bandwidth have been presented. As an example, the working group C-19W of the IEEE Insulated Conductors Committee (ICC) developed a guide, [23], that describes methods for detecting and locating PD sources in power cable systems. In this frame, two features are of utmost importance for filter design: overall sensitivity and PD location resolution (i.e. the capability of locating PD sources in time or frequency domain). The guide suggests that band pass filters having typical bandwidths in the 5-20 MHz range are, in most cases, capable to achieve good sensitivity and time resolution for source location. Other works indicate narrow systems at very high frequencies (e.g. UHF and VHF detectors) as optimum detectors [24-25], even if this solution is applicable only when the coupler is very close to the PD source. A few authors suggest using Matched Filter Banks (MFB) [26].

By using the analytical model developed in 4.1 fed by electrical and geometrical data relevant to MV extruded power cable, it can be evaluated quantitatively how the optimum detection bandwidth decreases with the distance between the coupler and the PD source (see Figure 1.29). This means that, for every distance, a different Δf_{OPT} value can be defined and, therefore, no optimal solution can be developed unless the distance between the source and the coupler is not specified.

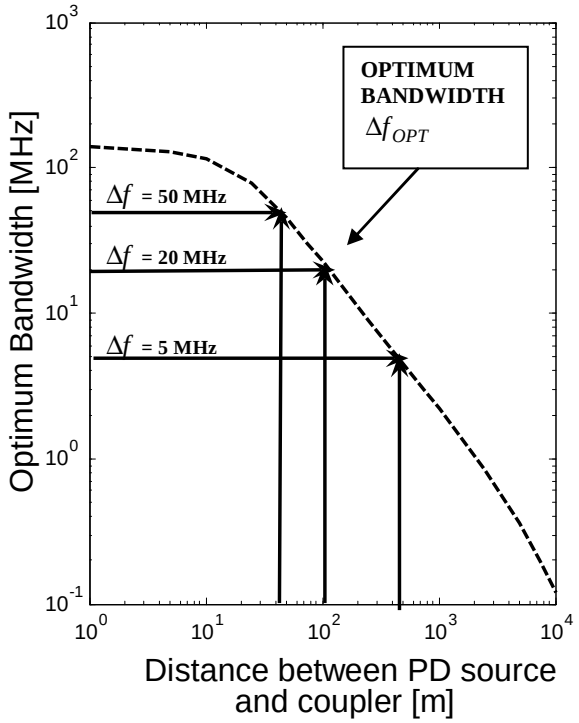

FIGURE 1.29 Optimum detection bandwidth as a function of the distance between the PD source and the coupler. Bandwidths equal to 5, 20 and 50 MHz are the optimum ones for PD pulses coming from 450, 100 and 40 m far from the coupler respectively.

Since the optimum detection bandwidth can be evaluated only if the traveled distance is known, some sub-optimal solution need be found. To do so, one must bear in mind that PD phenomena are generally located at accessories (due to inadequate assembly, to the presence of contaminants, etc.). However, they might occur also in cable splices (due to, e.g. protrusions at semicon screens, air pockets associated with thermal cycling, damage of sheath conductors during cable pulling, etc.). Accordingly, different in-field measurement configurations can influence the detection bandwidth choice.

- Measurements from joint capacitive taps. If joints are endowed with capacitive taps, very large bandwidths (provided they do not exceed the upper cutoff frequency of the sensor) could ensure good sensitivity for distances comparable with joint dimensions. However, if PD originate in cable splices, the distance between the PD sites can be very long as some hundreds of meters, and cable attenuation can

strongly reduce detection sensitivity, leading to false negative detection.

- Measurement from link boxes. The cross bonding coaxial cables can be exploited to achieve PD detection during after laying tests [27]. The attenuation of such coaxial cables, a few of tens meters long, can influence detection sensitivity, so that bandwidths of several hundreds of MHz are not advisable.

- Measurement from cable terminals. If a long transmission line has inaccessible joints (e.g., submarine HV cables, buried HV or MV cables), the measurements can be done only at the cable terminals. In this case, cable length and attenuation characteristics become the predominant factor in detection bandwidth choice. For long cables, it could be worthwhile trying to use relatively low bandwidths or MFB.

By comparing these cases, it comes out that cable attenuation characteristics play a major role in PD detection. In fact, due to cable attenuation, when using bandwidths as large as several hundreds of MHz, noise can dominate PD signals if the source is few meters far from the coupler. Therefore, such bandwidths can be appropriate only if PD sources are very close to the coupler, but ineffective when PD sources are some meters away. Some tens of MHz could allow detecting with sufficient sensitivity PD coming from the joint and the neighboring splices when measurements are performed from capacitive taps or at link boxes. For long cable systems, accessible from terminations only, it would be advisable to use different detection bandwidths, the larger ones to detect near defects (e.g. in the terminations), the lower ones to detect PD originated at some distance from terminations. According to these considerations, a methodology to design filter bandwidth for UWB detectors is proposed in the following section.

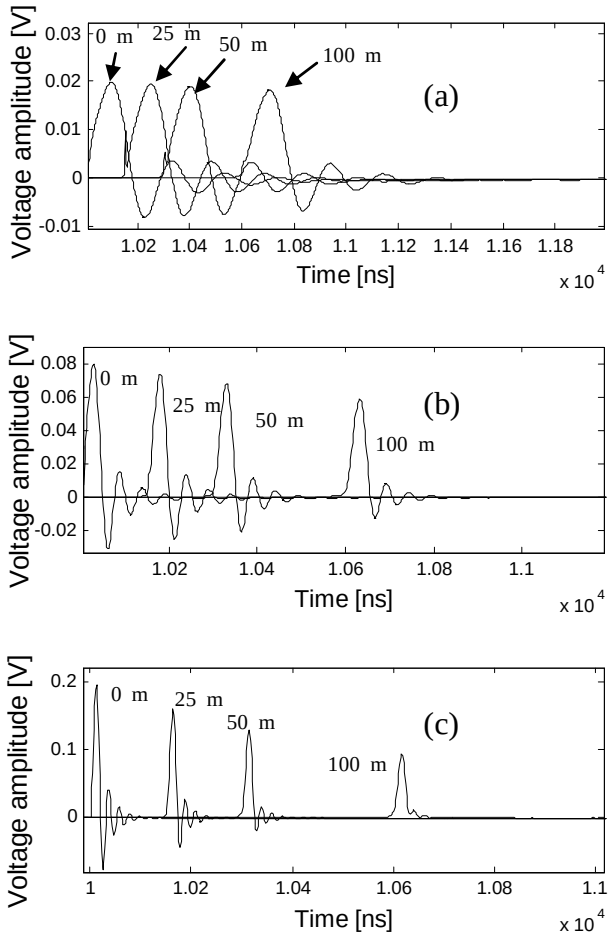

FIGURE 1.30 Ideal PD pulses detected at 0, 25, 50 and 100 m far from the coupler through a bandwidth of 5 MHz (a), 20 MHz (b) and 50 MHz (c). Lower cutoff frequency is 30 kHz. Time domain.

In order to clarify the effect of bandwidth, simulation of pulses as received by detectors having different bandwidths are reported in the following. The simulations make reference to a MV cable 100 m long. Environmental noise and disturbances are assumed to be negligible. As emphasized by Figure 1.29, pulses coming from distances equal to or shorter than 100 m have optimum bandwidth equal to or greater than 20 MHz. Here, three different detection bandwidths, Δf, are dealt with:

- Δf=5 MHz (<20 MHz). The chosen bandwidth is lower than the optimum one. Using such detector, all the PD pulse frequency components above 20 MHz are filtered out. This means that, independently of distance, but particularly for PD signals coming

from sources close to the coupler (which can have frequency components up to hundreds of MHz), most of the frequency spectrum is lost. Thus, (a) the peak voltage of the detected PD pulses can be strongly reduced (compare Figure 1.27 to Figure 130a) and (b) pulses coming from different points can be detected with similar time-frequency domain features. As depicted in Figures 1.30a and 1.31a, the waveforms of PD pulses, coming from 0, 25, 50 and 100 meters far from the detection point, look very similar in both the time and the frequency domain.

- Δf=20 MHz. The chosen bandwidth equals the optimum one. Also in this case each pulse coming between 0 and 100 m has a frequency spectrum larger than the chosen bandwidth and many frequency components are filtered out. However, differently from 5 MHz bandwidth detectors, pulses coming from different distances result much dissimilar in the time and frequency domain (Figures 1.30b and 1.31b), allowing for PD pulse separation and localization.

- Δf=50 MHz (>20 MHz). The chosen bandwidth is larger than the optimum one (it is the optimum bandwidth for a distance of about 40 m, see Figure 1.29). By this way, it is possible to preserve most of the frequency spectrum of the PD signals. As emphasized in Figures 1.30c, by choosing 50 MHz bandwidth the PD pulse peak value at detection point is 10 times greater than that detected by 5 MHz detector. Furthermore, pulses coming from different points are very dissimilar in time and frequency domain (allowing for sources separation and, if needed, localization). However, in the presence of white noise, the signal-to–noise ratio can strongly decrease if the chosen bandwidth is significantly higher than the optimum one. As example, assuming a fixed SNR of about 5 dB for pulses coming 100 m far from the coupler and detected with an optimum bandwidth of 20 MHz (as suggested in Figure 1.29), the signal–to-noise ratio is reduced to 2 dB and – 1 dB if bandwidths of 50 and 100 MHz are chosen, respectively (see Figure 1.31).

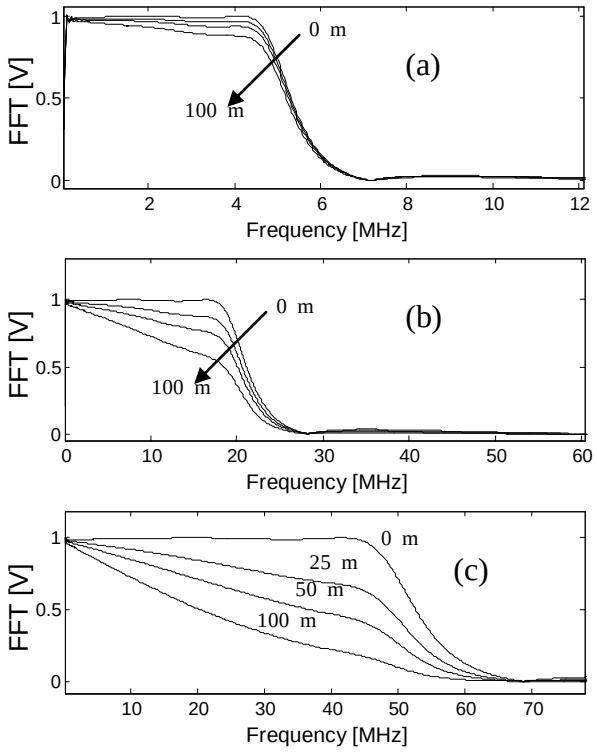

FIGURE 1.31 Ideal PD pulses detected at 0, 25, 50 and 100 m far from the coupler through a bandwidth of 5 MHz (a), 20 MHz (b) and 50 MHz (c). The lower cutoff frequency is 30 kHz. Frequency domain.

From these examples, it comes out clearly how the knowledge of cable length and propagation characteristics is essential to determine the optimum detection bandwidth. Using a large bandwidth it is possible to preserve most of the frequency components of the PD pulses, so that the separation of different PD sources can be performed more accurately thanks to the techniques developed in 4.1.

It is important to stress, however, that such experiments have been done without accounting for environmental noise that is always found in on-field measurement. In fact, as emphasized in Figure 1.32, in the presence of background noise detection sensitivity can be less than optimal if a bandwidth much larger than the optimum one is chosen. In practice, to achieve a good compromise, when making measurements on accessory-per-accessory basis, it can be feasible to choose a detection bandwidth equal to the equivalent bandwidth for a length equal to half the distance between two cable accessories.

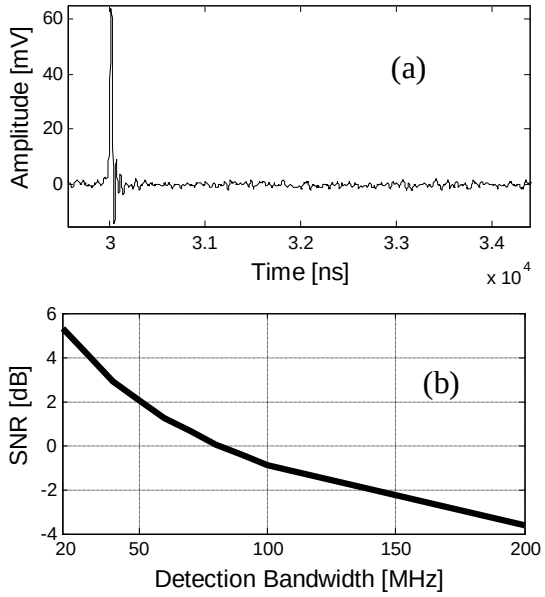

FIGURE 1.32 A PD pulse, 100 m far from the detection point, overlapped to a Gaussian white noise, is detected through a bandwidth ranging from 20 to 200 MHz. (a). As the bandwidth increases, the SNR, evaluated using (1.26), decreases (b). If the detection bandwidth is chosen close to the optimum one, the SNR improves.

As an example, for HV power cable having accessories at a distance of 500 m one from the other one, the detection bandwidth can be established by evaluating the optimum one for a distance of 250 m. Using the data relevant to the MV cable described here, the optimum bandwidth is about 10 MHz. Thus, since HV cables are less attenuated than MV ones, the 20 MHz value proposed by the IEEE ICC does seem in line with the evaluation reported in this paper.

1.6 Coupling mechanisms for PD in cables

Alternative solutions for picking up PD signals may resort to the use of antenna sensors. However, the mechanism of coupling between PD sources and cables has to be established in order to design antennas in the most effective way. With this respect, one has to consider that two different types of PD sources can be found in power cable systems: internal and surface PD [23]. Surface PD are generally due to flaws in stress grading systems and

occur in accessories on the boundaries of the insulation system. The current pulse generated by these sources is likely to flow through the semiconductor and returning through the shield of the cable. Internal PD are due to internal defects as voids. In this case, PD pulses tend to flow through the internal conductor and return through the shield of the cable.

These two different mechanisms through which PD pulses can drive a cable to irradiate electromagnetic field (similar to those observed for electromagnetic field radiated from printed circuit boards with cables attached, [28-30]), can interact in different ways with antennas, providing different sensitivities and, possibly, highlighting the need for different antenna types to achieve an optimum solution. This paper will focus on how the two different mechanisms couple the PD to one termination of the cable. To achieve that, models are postulated and studied first, validated then through measurements in the lab. Results indicate that, generally, surface PD can be detected with larger sensitivities than internal PD, although sufficient sensitivity for PD detection could be achieved through appropriate antenna/amplifier selection.

In order to quantitatively evaluate the coupling between PD and cables, it is necessary to postulate the geometry of the system and, in particular, how a PD event can be schematized. A reasonable approximation for PD discharges resorts to a pulsed current flowing in an open-ended filamentary conductor behaving similarly to an elementary small antenna. In particular, for internal PD, the filamentary conductor is inside the insulator, orthogonal to the axis of the cable. For surface PD, the filamentary conductor is parallel to the axis of the cable and lies between the insulator and the semiconductor.

Following the above considerations, two different equivalent circuits have to be considered to model how PD pulse couple with power cables. For surface PD, it is assumed that the PD current pulse travels in the loop made by the discharge itself and part of the cable shield. This current loop couples magnetically with the loop made by cable core and shield, transferring part of the PD energy to the cable itself. This coupling mechanism can be modeled as a current-controlled voltage generator V_E within the shield-core loop:

$$\hat{V}_E = j\omega M \hat{I}_{PD} \tag{1.27}$$

being M the mutual inductance between the two aforementioned loops, I_{PD} the PD current and ω is the angular frequency of the source. Accordingly, the equivalent circuit depicted in Fig. 1.33 can be studied to evaluate quantitatively PD-cable coupling.

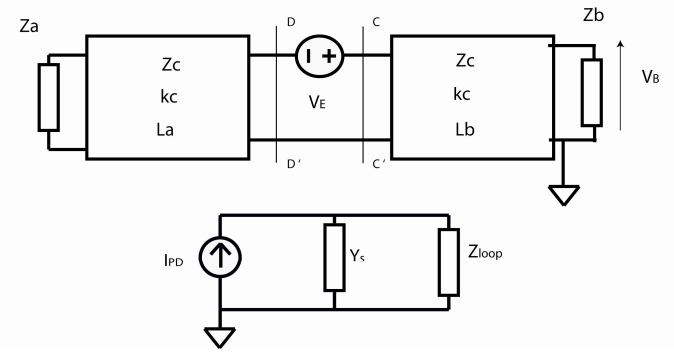

FIGURE 1.33 Equivalent circuit representing how surface PD couple to the cable.

The MV cable is represented by a transmission-line model with its Z_c characteristic impedance, k_c propagation constant and lengths L_a and L_b. The admittance Y_S is assumed to be infinite for a PD event (that is to say, it is the PD current that drives the current-controlled voltage source). Finite admittances will be considered later on dealing with measurements performed through network analyser (in that case, Y_S will be equal to 1/50 S).

For internal PD, it is speculated that the PD pulse couples with the cable through the electric field established between the PD site and the core, thus in a capacitive way. Assuming that the PD pulse is an ideal Norton generator, the internal PD can be described as a current generator in parallel with the two branches of the cables. However, in order to provide a unified treatment with the measurements carried out in the following, the scheme of Fig. 1.34 will be employed. In this scheme, the current generator is controlled by the voltage established across the mutual capacitance C between the PD source and the cable core by the PD and can be evaluated through (1.28), where V_C is the voltage across the mutual capacitance.

$$\hat{I}_E = j\omega C\hat{V}_C \tag{1.28}$$

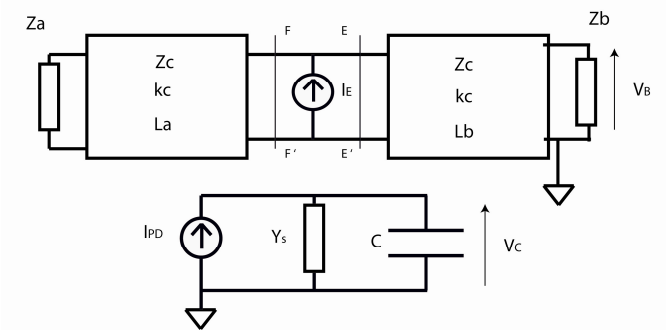

FIGURE 1.34 Equivalent circuit for representing internal PD coupling to the cable.

In the following, the accuracy of the proposed models is verified through experimental measurements. In particular, internal and surface PD were simulated in a 2-meter long EPR insulated cable as sketched in Fig. 1.35. The filamentary conductors were energized through the signal generation stage (RFOUT) of a Network Analyzer Agilent 4862B. In order to validate the model, the cable input impedance and the S21 parameter between cable and equivalent PD source ports were evaluated analytically and compared with measurements carried out using the NA with test set S parameter HP 85046A. The measured frequency range is 10-500 MHz with a resolution bandwidth of 1 kHz. The accuracy of the measurement is ±1.2 dB and ±3 degrees for magnitude and phase respectively.

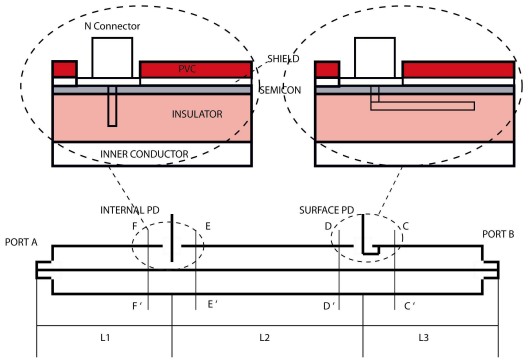

FIGURE 1.35 Experimental setup used to investigate coupling between PD sources and power cables.

The S parameter between the equivalent surface PD source and cable termination B can be computed as:

$$\hat{S}_{SUP-B} = \left.\frac{\hat{V}_B^-}{\hat{V}_{NA}^+}\right|_{\hat{V}_B^+=0} = \frac{\hat{Z}_{CC'} \cdot j\omega M}{\hat{Z}_{CC'} + \hat{Z}_{DD'}} \cdot \frac{2 \cdot \left(1 + \hat{\Gamma}_L\right)}{\frac{1}{\hat{Y}_S} + \hat{Z}_{loop}} \tag{1.29}$$

being $\hat{Z}_{CC'} = \hat{Z}_{in}(\hat{Z}_b, L_B)$ and $\hat{Z}_{DD'} = \hat{Z}_{in}(\hat{Z}_a, L_A)$ the input impedances at ports CC' and DD' respectively with

$$\hat{Z}_{in}(\hat{Z}_L, L) = \hat{Z}_c \frac{\hat{Z}_L + \hat{Z}_c \tanh(\hat{k}_c L)}{\hat{Z}_c + \hat{Z}_L \tanh(\hat{k}_c L)} \tag{1.30}$$

Z_a and Z_b are the cable terminations, L_b=L_3, L_a=L_1+L_2, Z_s the source impedance and Z_{loop} the impedance of the PD source loop.

The S parameter between the equivalent internal PD source and cable termination B can be computed as follow

$$\hat{S}_{INT-B} = \left.\frac{\hat{V}_B^-}{\hat{V}_{NA}^+}\right|_{\hat{V}_B^+=0} = \frac{\hat{Z}_{EE'} \cdot \hat{Z}_{FF'}}{\hat{Z}_{EE'} + \hat{Z}_{FF'}} \cdot \frac{2 \cdot \left(1 + \hat{\Gamma}_L\right)}{\frac{1}{\hat{Y}_S} + \frac{\hat{Z}_{EE'} \cdot \hat{Z}_{FF'}}{\hat{Z}_{EE'} + \hat{Z}_{FF'}} + \frac{1}{j\omega C}} \tag{1.31}$$

being $\hat{Z}_{EE'} = \hat{Z}_{in}(\hat{Z}_b, L_B)$ and $\hat{Z}_{FF'} = \hat{Z}_{in}(\hat{Z}_a, L_A)$ the input impedances at ports EE' and FF' respectively, L_a=$L1$, L_b=L_2+L_3. Γ_L is the reflection coefficient seen at section BB'. The input impedance of the cable at section BB' can be evaluated by (1.32).

$$\hat{Z}_{in,B} = \hat{Z}_{in}(\hat{Z}_a, L1 + L2 + L3) \tag{1.32}$$

Given these premises, the parameters for the equivalent circuits of Figs. 1.33 and 1.34 are calculated using the values listed in Tab. 1.2.

The additional parameters (M, C, L_{loop}) needed to evaluate the S parameters of the system can be calculated either analytically or through numerical simulations. In particular, the source loop for surface PD (formed by the filamentary conductor and small part of the cable shield) was estimated to be a rectangular path of dimensions 30 x 2 mm whose self and mutual (with the loop formed by the internal conductor, the termination

loads and the shield of the cable) inductance was estimated by well known formulas [31]. The mutual capacitance between the internal PD and the cable core can be estimated analytically as explained as in [32]. These values were also computed by numerical simulations using the Finite Integration Technique (FIT) [33] and compared with the estimated ones showing a fairly good agreement (see Table 1.3). Eventually, the characteristic impedance and propagation constant of a power cable can be measured as in paragraph 4.1 taking into account attenuation effects due to skin effect, semiconductor layers and dielectric insulation losses.

TABLE 1.2 Parameter values

Parameter values for MV EPR insulated power cable			
L1 [mm]	1000	Ys [S]	1/50
L2 [mm]	700	Za [Ω]	Open
L3 [mm]	750	Zb [Ω]	50
kc [1/m]	as in [9]	Zc [Ω]	20

TABLE 1.3 Computed and simulated parameters values

Computed and Simulated values for sources		
Parameter	Computed	Numerical simulation
M [nH]	0.1	0.2
C [pF]	0.5	0.6
Lloop [nH]	3	3

The first evaluation carried out was a comparison between (1.32) and the cable input impedance measured at port A. This was made using both a purely imaginary propagation coefficient ($k_c=j\beta$, lossless case) as well as a complex one ($k_c=\alpha+j\beta$, lossy case). It was observed that a very good agreement between model and measured data could be obtained when cable losses are accurately modeled (the results are not reported here for the sake of brevity).

Coming to results that are more related to the issue of PD detection, the comparisons of measured and calculated S21 parameters (between equivalent PD source and cable termination) are reported in Figs. 1.36-1.39 for both surface and internal PD. In both cases, there is a very good agreement between model data and measurement results, showing that both capacitive and inductive coupling modes between PD sources and cable systems can be studied through equations (1.29)-(1.32).

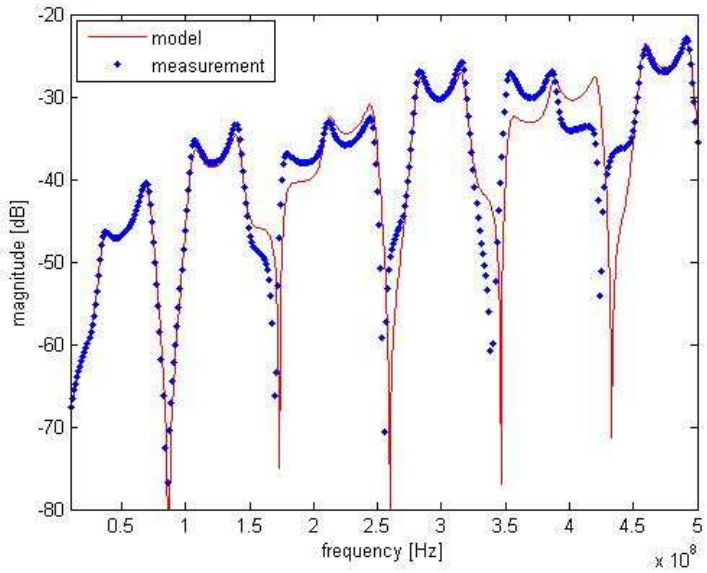

FIGURE 1.36 Magnitude of S21 parameter between the surface PD equivalent source and cable port B.

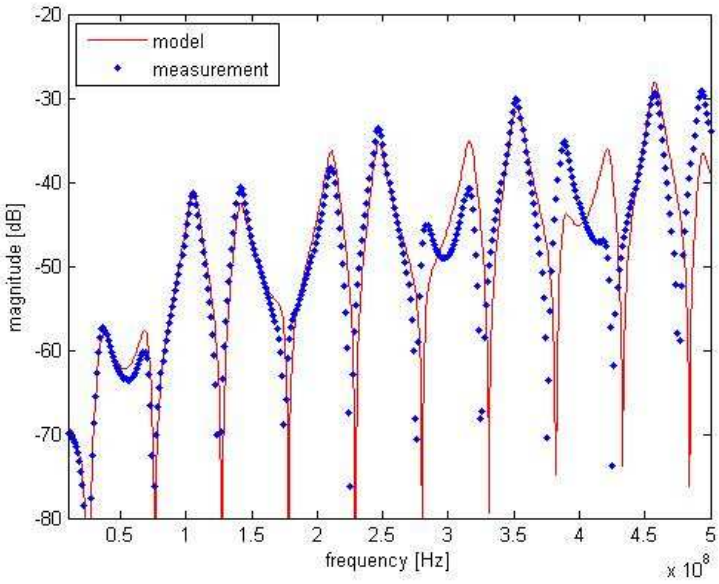

FIGURE 1.37 Magnitude of S21 parameter between the internal PD equivalent source and cable port B.

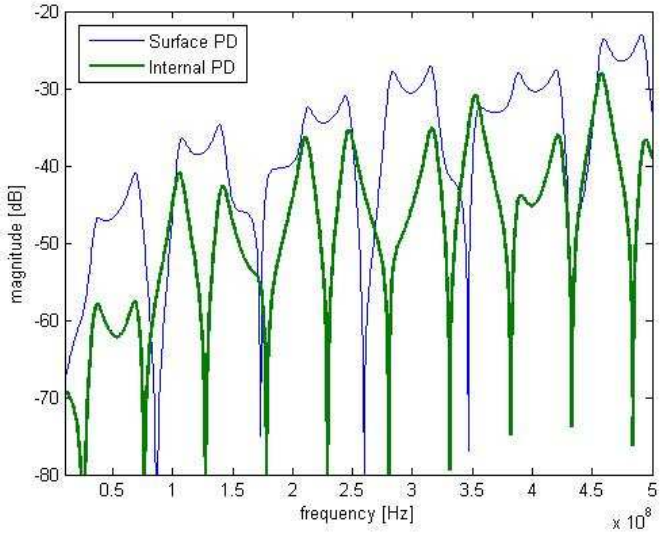

FIGURE 1.38 Comparison of coupling to port B of the cable for surface and internal PD.

When the cable is not perfectly shielded, radiated emissions due to PD from the cable can be measured using antennas. In this case, the cable behave as an antenna and the larger the energy transferred from the PD source to the cable the larger is the detection sensitivity (if we disregard, by now, radiation patterns). The practical implications for PD detections coming from the analysis reported here are emphasized through Fig. 1.38, which shows the comparison between the S21 parameter for the two different types of PD. It can be observed that, at large frequencies, surface PD tend to couple more energy to cable terminations (larger S21 values) than internal PD, this effect being less marked at the lowest frequencies. Therefore, surface PD are generally detected with larger sensitivity at larger frequencies, whereas there is no significant difference at the lowest ones (i.e., at those frequencies where conventional measurements of conducted signals are carried out). Moreover, detection at large frequencies can be favored for both types of PD but, in particular, for those of surface type (thus, it can be expected that radiated pulses from surface PD display a larger frequency content than those from internal PD).

Partial Discharge Measurements

The practical conclusions inferred from the above analysis can be accepted if the filamentary conductor approximation used to build up the model is a realistic approximation of PD phenomena. Since a direct proof of this is impossible, an indirect one was sought. In particular, PD measurements performed on a cable with artificial defects using a high frequency current transformer and an antenna were compared to verify if the general statement that surface PD can be detected with larger sensitivity and at larger frequencies than internal PD could be accepted. For this purpose, PD were artificially induced in a 2-meters long cable. Internal PD were created by drilling a hole in the dielectric, inserting a metal object and filling the hole with rubber. Eventually, the shield was recreated using semicon tape. Surface PD were created by shortening the electrical distance between the high voltage conductor and shield through semicon tape. A log-periodic antenna (100 MHz-3 GHz) was placed near the termination B of the cable and the electromagnetic radiation was received using an R&S FSH3 Spectrum Analyzer. Conducted PD signals were detected through a high frequency current transformer (HFCT) having lower and upper cutoff frequencies of 16 kHz and 40 MHz, respectively. The complete PD pulses were recorded and stored through an Ultra-Wide Band (40 MHz) detector.

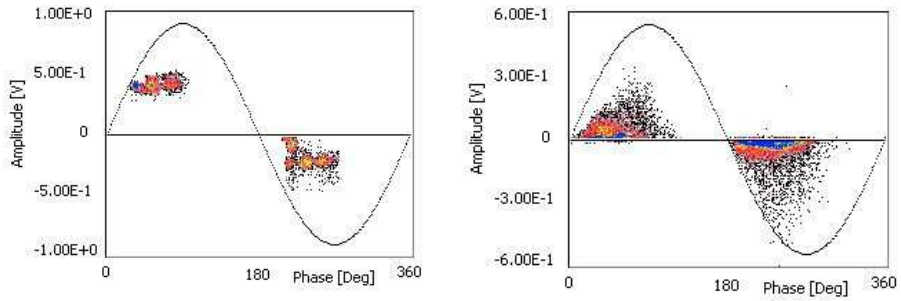

(a) (b)

FIGURE 1.39 PRPD pattern relevant to (a) internal PD, (b) surface PD. Sensor: HFCT placed around the ground connection of the cable.

The results of conventional measurements (i.e., those performed on conducted signals through HFCT) are presented in Fig. 1.39, which shows the so-called Phase-Resolved-Partial Discharge (PRPD) Pattern [19-22]. As can be seen, internal PD display, on average, a magnitude that is larger

(almost two times) than that of surface PD. Measurements performed through the log-periodic antenna, however, behave exactly in the opposite way (see Fig. 1.40), that is to say, surface PD detected by the spectrum analyzer (using the Max-Hold mode and 1 MHz resolution bandwidth) mode display a much larger magnitude than internal PD. This finding indirectly confirms that internal PD can be detected through antennas with a lower sensitivity than internal PD. Furthermore, Fig. 1.40 emphasizes that, as predicted by the model, surface PD are detected with larger frequency content.

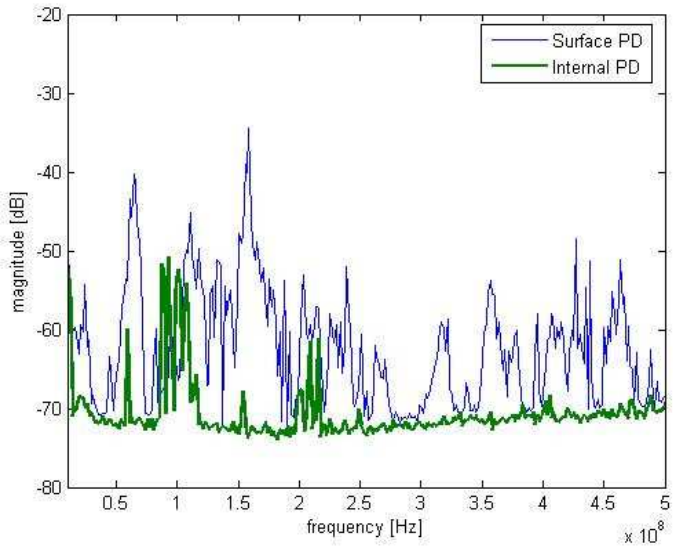

FIGURE 1.40 Spectrum of internal and surface PD as received through a logperiodic antenna.

1.6 Typical sensors for PD detection in MV cables

Standard circuit analysis shows that a HFCT (represented by a pair of coupled inductors having self-inductances at the primary and secondary winding L1 and L2, respectively, mutual inductance M) excited by an ideal current generator at port 1 and closed on a 50 Ohm resistor at port 2 (detector port), as shown in Fig. 2.1, will display a voltage across the terminals of port 2 given by (1.33).

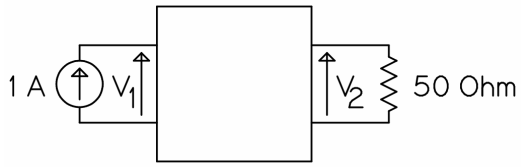

FIGURE 1.41 Equivalent circuit for the HFCT connected on port 1 to an ideal current generator, on port 2 to a 50 Ω resistance representing the detector input.

$$V_2 = \frac{j \cdot \omega \cdot 50 \cdot M}{50 + j \cdot \omega \cdot L_2} \tag{1.33}$$

The ideal system will thus behave as a high-pass filter having gain at very large frequencies:

$$V_2(\infty) = 50 \cdot M / L_2 = 50 \cdot \frac{N_1}{N_2}\left(1 - \frac{R_{FE}}{R_{FE} + R_{A_2}}\right) \tag{1.34}$$

and cutoff frequency

$$f_c = \frac{1}{2 \cdot \pi} \cdot \frac{50}{L_2} \cdot \frac{1}{2 \cdot \pi} \cdot \frac{50}{N_2^2 \cdot \left(\frac{1}{R_{FE}} + \frac{1}{R_{A_2}}\right)} \cdot \approx \frac{1}{2 \cdot \pi} \cdot \frac{50}{N_2^2} \cdot R_{FE} = \tag{1.35}$$

$$= \frac{1}{2 \cdot \pi} \cdot \frac{50}{N_2^2} \cdot \frac{l}{\mu_{FE} \cdot A}$$

being R_{FE} the reluctance of the ferrite core, R_{A_1} (R_{A_2}) that of the stray fluxes at the primary (secondary) circuit of the HFCT, respectively, μ_{FE} , l, A the magnetic permeability, length and area of the iron core. Ideally, the reluctance of the iron core could be neglected with respect to that of the air, leading to the ideal transformer equation:

$$V_2(\infty) = 50 \cdot \frac{N_1}{N_2} \tag{1.36}$$

In reality, the core of the HFCT, which will be realized in ferrite, at some

critical frequency will display decreasing permeability levels. At high frequencies, this feature of ferrite cores will turn into higher core reluctances and, therefore, poor coupling factors, *k*:

$$k = \frac{|M|}{L_1 \cdot L_2} = \frac{1}{\sqrt{\left(1 + R_{FE} / R_{A_1}\right) \cdot \left(1 + R_{FE} / R_{A_2}\right)}} \tag{1.37}$$

According to (1.35) this will also lead to a reduction of the voltage at the detector port, that is to say, the PD detection circuit will show decreasing sensitivity.

In selecting ferrites used in HFCT cores, a compromise between bandwidth and permeability needs to be achieved. As a matter of fact, ferrite cores with very large bandwidths are generally characterized by low magnetic permeability values (see Fig.1.42). They will provide, therefore, HFCTs having low gain (1.34) and high lower cutoff frequency (1.35). The compromise will be dictated by the characteristics of the pulses that have to be detected, as shown in the next section.

The 50 Ohm resistor to which the HFCTs must be closed is necessary in order to achieve best coupling, i.e. avoiding signal energy reflections due to the impedance mismatch, which can result in a reduction of transmitted power and, thus, sensitivity.

Transfer impedance of a lot of 25 HFCT sensors commercially available are shown in Fig. 1.43, where the boxplot for the voltage gains (V2/V1) measured in the lot are reported. The measurements have been performed using a network analyzer. Port 1 was short circuited (Rout=50 Ω). The HFCT was clamped around the jumper wire short-circuiting port 1 and closed on port 2 (Rin=5 Ω). Note that the transfer function of the sensor show very good coupling up to few tens of MHz, thus, matching the optimum bandwidth for PD detection in MV cables, according to the investigation carried out in this chapter.

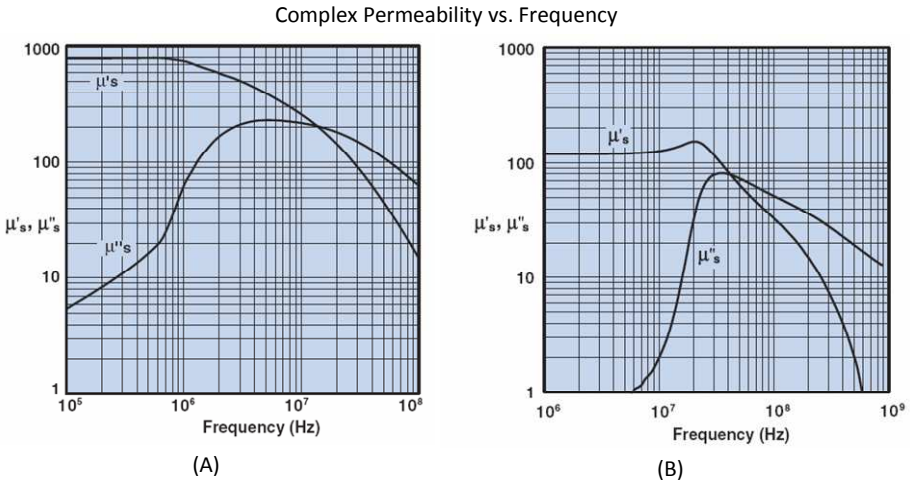

FIGURE 1.42 Complex permeability of two different ferrites: ferrite (A) has larger permeability than (B), but on a narrower frequency range.

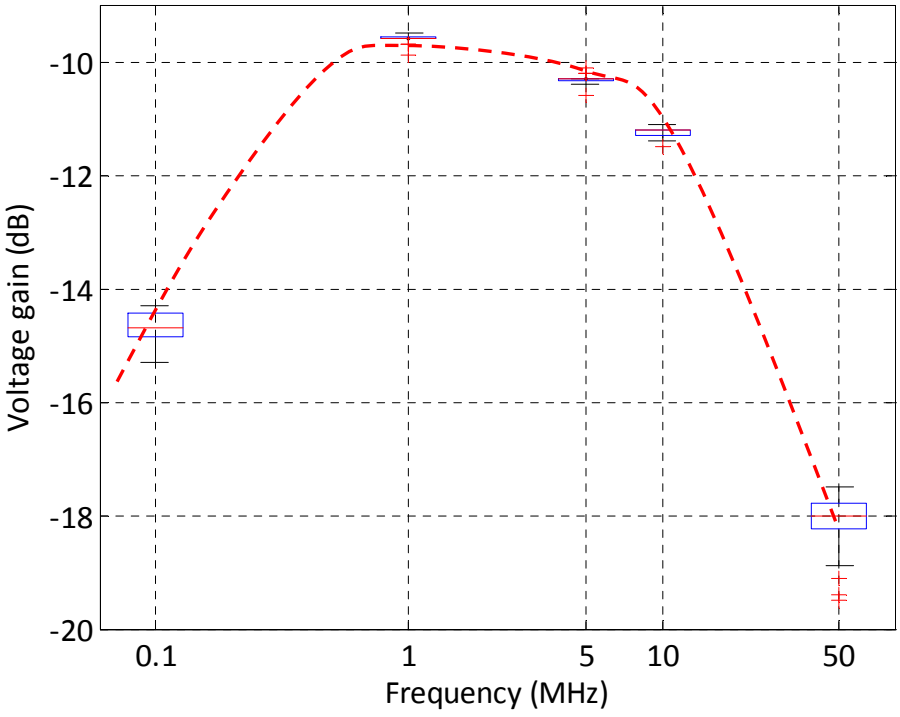

FIGURE 1.43 Transfer impedance of a lot of 25 HFCT sensors commercially available.

Chapter 2

PD Pulse propagation and detection in Medium Voltage transformers

2.1 Premise

Investigation on PD pulse propagation in distribution transformers is described in the forthcoming paragraphs. Both conducted and irradiated phenomena generated by PD events within the transformers will be taken into account to give a complete view of the problem. The target of such a study is to introduce new and effective detection methods which allow non intrusive on-line PD measurements to be successfully carried out, achieving best SNR and, thus, gaining the largest number of diagnostic information about the system under test. In particular, such new methods will be based on the possibility of detecting EM radiation, produced by PD sources occurring inside transformers, from outside through properly designed UHF couplers. In order to design proper sensors it is necessary to know the frequency range where EM waves, due to PD events, may propagate. Several ways to evaluate the electric and magnetic field inside HV/MV transformers exist, based on resonance cavity theory, but no reference in literature exist regarding the possibility and methods to evaluate the electric and magnetic field radiated outside distribution transformers. Indeed, in the following paragraphs it will be shown that MV transformers can be analytically studied as shielded enclosures with circular apertures (which allow bushings or cable termination entrance). It will be shown that such methods can easily give

accurate solution of the problem in far field region, but very complex numerical treatment is necessary to solve the problem accurately in near field region as well. A further analytical innovative approach will be then considered, applying an analytical transmission line model to the transformer, showing both good fitting with experimental results and the possibility to give also significant information relevant to the near field region. Such an approach takes inspiration from numerous problems dealt with in literature regarding shielding efficiency problems. The main difference between the literature approach and the one considered in the following work is the source location. Indeed, literature authors use to place emitting sources outside the enclosure and evaluate the penetration of the electric field, radiated through an aperture on the wall, inside the enclosure. On the contrary, in this work the emitting source, simulating PD events inside the transformer, will be placed inside the shielded enclosure and the radiation through the aperture will be studied outside the cavity.

However, it will be shown that although such methods are potentially accurate, the numerical computation can become significantly complicated when the whole complex structure inside the transformer is considered, particularly when near field region is investigated. Therefore simulation through proper Computer Aided Design (CAD) software, based on Finite Element Methods (FEM), were carried out to represent thoroughly the transformer with all its components (e.g., iron core, windings, bushings, oil, etc…) showing very good agreement with experimental data. Owing to the results obtained from the simulations it is therefore possible to design proper sensors, as it will be described in 2.5.

Before starting, it must be emphasized the applicative aspects of the following work, since IEC international standards do not require any Partial Discharge test in factory for MV/LV oil insulated distribution transformers, differently from cast resin and HV/MV oil insulated transformers. Therefore it is possible that distribution transformers affected by significant PD activities due to bad manufacturing issues might be installed on field and, thus, experience unexpected premature failures. Furthermore, no after-laying test is required by the standards, which means that any problem due to either bad assembling operations on field or damages, occurring during transportation from the factory to the working site, could not be detected after the installation, thus increasing considerably the failure risk, especially over the first period of life. Hence, the study carried out in the following

work can be extremely helpful to carry out PD measurements on line with very good sensitivity through new detection methods, in order to assess transformers conditions after the installation on field and during their life time, thus preventing premature failures that sometimes lead into economical losses which can be comparable to those observable in HV systems.

A brief summary of the existing detection methods is given in 2.2, before describing the new ones.

2.2 Overview on existing PD detection methods

Existing PD detection methods are considered in the following along with their major advantages and criticalities.

2.2.1 PD detection from capacitive taps in power transformers

Power transformer bushings are often provided with embedded capacitive taps [34], which can be treated as a capacitive voltage divider connected in parallel to the transformer. They consist of a certain number of paper layers, wrapped around the main conductor within the bushing, between two conducting layers, as sketched in Fig. 2.1. Such multiple layers of paper and conducting materials constitute, therefore, a series of cylindrical paper insulated capacitors in parallel to the transformer. The voltage can be picked up across one of them, C_b, constituting a pure capacitive voltage divider.

A measuring impedance, Z_m, is then connected in parallel to the low voltage capacitor C_b. Such measuring impedance is integrated in an external tap adapter, which consists of a customized plug to be fixed directly to the tap, including proper designed surge protections. The measurement impedance Z_m is generally composed by a resistance, R, which may vary from 100 to 200 Ω. The rated values of the above mentioned electrical components are chosen on the basis of the bushing tap capacitance value C_b, to be provided by the either the customer or the transformer manufacturer. Oil insulated distribution transformers are generally not provided with such embedded sensors.

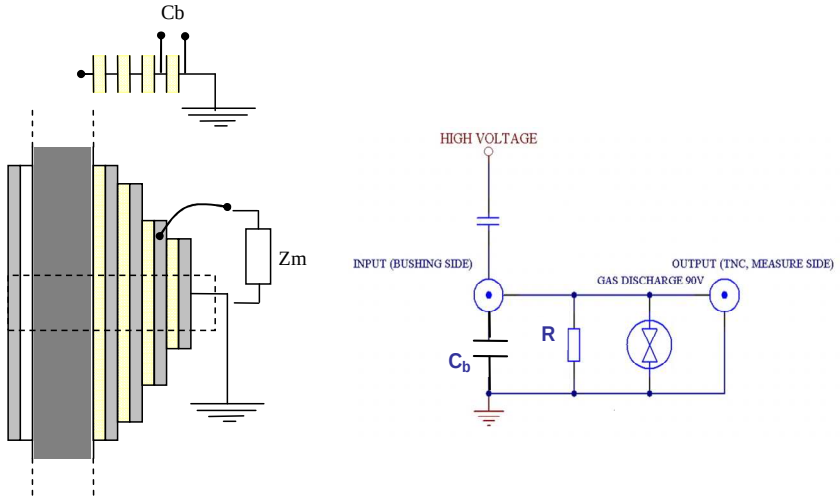

FIGURE 2.1 Layout schemes of capacitive taps installed inside power transformer bushings around the central conductor (left) and relevant electric circuit (right). Paper layers are represented in yellow, conductive layers in grey.

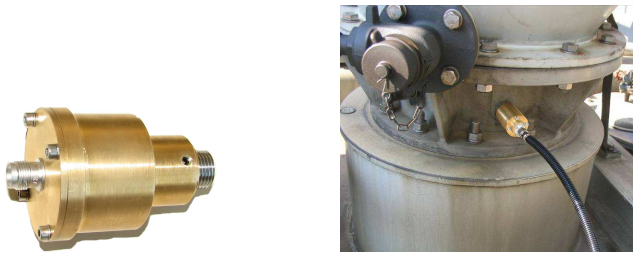

FIGURE 2.2 Pictures of a commercially available Tap Adapter and its installation.

2.2.2 UHF detection using internal and external sensors in power transformers

Investigation in Ultra High Frequency (UHF), i.e., between 300 and 3000 MHz, and Very High Frequency (VHF), i.e., between 30 and 300 MHz, ranges was extensively carried out in the past to allow PD detection to be performed in HV Gas Insulated Systems (GIS) [35-38]. In particular, Gas Insulated Lines (GIL) present the same geometrical characteristics of a coaxial waveguide which can allow electromagnetic waves propagation, with very low attenuation above a certain cutoff frequency, when excited by an internal source. In the case of GIS or GIL apparatuses, the EM wave propagation can be originated by impulsive and repetitive PD pulses

occurring inside the system which may have rising time less than several *ns* and, thus, containing frequency components up to few GHz at the source. Indeed, thanks to their broadband frequency, such pulses can excite the resonances of the GIS and propagate along the system according to different modes, such as Transverse Electrical Magnetic (TEM), Transverse Electrical (TE) and Transverse Magnetic (TM). The TE and TM modes cut-off frequencies, above which attenuation is low enough to allow EM waves to propagate for longer distances than TEM mode, depend on the system geometry and size. TEM mode can however propagate at lower frequencies in coaxial GIL chambers especially when the PD source is close to the central HV conductor bar [39].

Since the effectiveness of PD detection in GIS systems, through proper both internal and external UHF sensors, has been widely demonstrated in literature, similar works were proposed for HV transformers [40]. Indeed, transformer tanks can be considered as resonant cavities, where TE and TM propagation modes can be excited by internal high frequency PD events, allowing, thus, electromagnetic waves propagation inside the transformer. Three kinds of sensors are mostly used to carry out PD measurements on power transformers:

- UHF internal disc couplers (Fig. 2.3): Their frequency range may vary depending on their size and design. They can be installed only in pre-existing sites according to the manufacturer. Sensitivity is excellent but global system reliability could be slightly affected since such sensors are intrusive.
- UHF external disc couplers: similar to those internal, but properly design to be coupled with existing circular dielectric windows (Fig. 2.4) . They are non-intrusive and can detect PD events occurring inside the transformer in UHF range. Their sensitivity can vary significantly with the window size.
- VHF oil valve sensors: such sensors are designed for large HV transformers, where TE and TM lowest cutoff frequencies are evaluated to be within the VHF range. They can be installed on-line, internally to the transformer, through the oil-valve placed at the bottom. Their sensitivity is maximum for PD occurring at the bottom of the transformer. They represent in general an optimum solution when combined with the capacitive taps, which are more sensitive for PD occurring in the upper part of the tank.

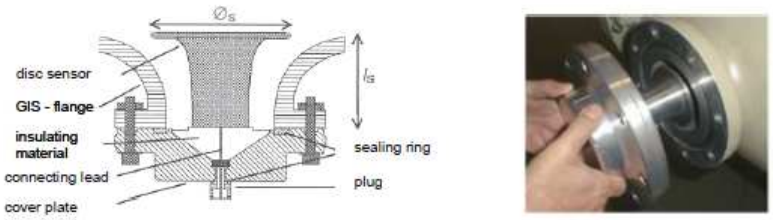

FIGURE 2.3 UHF internal sensor scheme (left) and its installation (right) for PD detection purposes in GIS systems and power transformers.

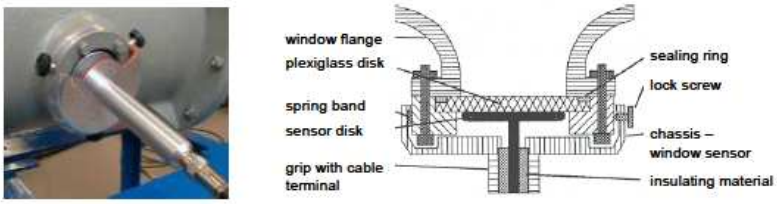

FIGURE 2.4 UHF external sensor, for PD detection purposes in GIS systems and power transformer, to be coupled to existing dielectric windows.

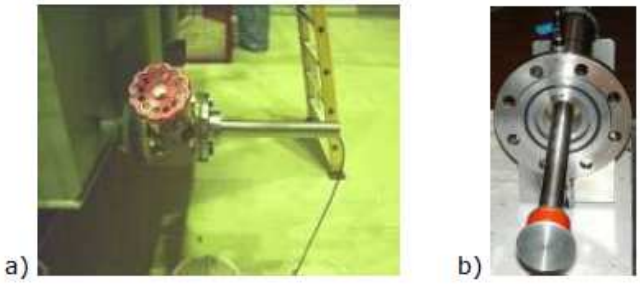

FIGURE 2.5 Internal VHF sensor for power transformer, to be introduced inside the oil valve at the transformer bottom.

2.2.3 Acoustic techniques

Acoustic sensors (10-300 kHz) are commonly used for PD detection and localization in HV transformers, through the measurement of the acoustic waves generated by PD activities within the transformer tank [41]. The resulting measured signal will depend on the PD source type (i.e., corona, surface PD, bubbles in the oil, etc…) and on the propagation path (distance between the PD source and the sensor). Acoustics signals can be picked up

through sensors placed either insode or outside the transformer tank. Acoustic emissions produced by PD events cause mechanical vibrations and can be sensed by means of piezoelectric transducers as well as fiber optic acoustic sensors, accelerometers, condenser microphones and sound-resonance sensors.

FIGURE 2.6 A commercially available acoustic sensor for PD detection in power transformers.

The frequency range, where acoustic sensors generally work, lies 10 kHz and 300 kHz. It must be pointed out that the acoustic wave propagation from the PD source to the acoustic sensor (transducer) is strongly influenced by the geometry of the test object. Reflections and refractions at the tank boundaries lead to distorted sound propagation that determines the resulting damping, absorption and scattering effects on the measurable acoustic compression wave. The main application for acoustic PD detection is localization through Time of Arrival methods. However it must be stressed that such sensors have generally poor sensitivity, being able to detect and localize only phenomena of very large magnitude.

2.2.4 Detection through HFCT sensors installed on power cables at transformer termination

When distribution transformers having nominal power below or equal to 1 MVA are tested, it is possible to achieve significantly good sensitivity by acting on the MV cables connected to the transformer. In particular, High Frequency Current Transformer (HFCT) sensors can be placed either around the cable ground lead or directly around the cable. The PD measurement can be carried out on-line and PD inside the transformer can be sensed. Anyway,

whenever PD are detected, a significant state of uncertainty can exist about the source location.

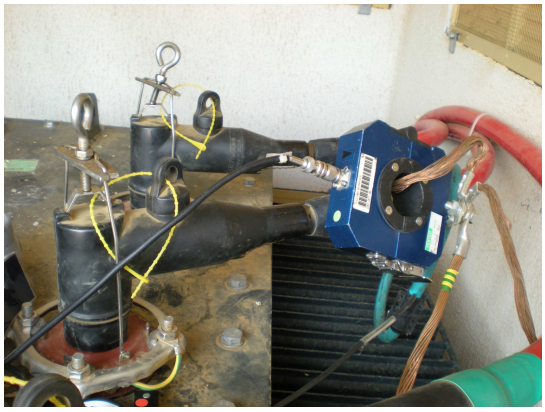

FIGURE 2.7 HFCT installation around ground leads of MV cables connected to distribution transformers.

Indeed, both PD sources inside the transformer and the cable may give rise to PD pulses traveling along the MV cables and, thus, that can be sensed by the HFCT clamped around the MV cable ground lead (Fig. 2.7). In case of PD detection, it can be significantly difficult to distinguish PD events caused by PD source within the cable termination to those occurring inside the transformer due to the fact that the distance between the PD source and the HFCT is within few meters in both cases, leading to comparable time and frequency characteristics of the PD pulses. In such cases, it is usually recommended to perform an off-line test feeding the transformer from the low voltage side and leaving open-circuited the MV terminals.

2.3 Investigation of irradiation properties of a metallic shielded enclosure with apertures

As mentioned in 2.2.2, Partial Discharge detection can be carried out in HV/MV power transformers by means of appropriate UHF sensors permanently installed inside the tank or coupled externally to pre-existing dielectric windows. Distribution transformers are provided generally with neither internal sensors nor dielectric windows and retro-fitting on transformers already in service to install internal sensors is usually not

allowed. Therefore Partial Discharge detection is carried out most commonly through HFCT sensors clamped around the cables ground lead or directly around the cables achieving good sensitivity but introducing a degree of uncertainty regarding the source location when PD activities are detected (conducted signals detected by the HFCT can be originated from defects in the transformer or in the cable). It is thus necessary to develop alternative sensors able to detect and localize PD sources, as well assess transformer condition on-line although they are not provided with preinstalled sensors or dielectric windows. This can be achieved by means of non-intrusive sensors which can capture the electromagnetic irradiation produced by PD sources within the transformer from outside, through, as an example, the apertures placed at the transformer top to allow bushings entrance. In order to properly design such sensors it is necessary to investigate on the frequency range at which irradiation outside the transformer tank can occur, depending on transformer size and design.

Before starting, it is necessary to point out briefly the differences between far-field and near field radiation [42]. Let assume a standard dipole emitting antenna, in the free space, having a maximum dimension D, resonance frequency f_0 and relevant wavelength λ_0, as shown in Fig. 2.8.

It is possible to divide the three dimensional space around the antenna in three regions as follows, where r is the distance from the antenna:

- Reactive near-field region ($r < R_1$): the reactive components of the electrical field predominate on the radiating fields. Reactive fields decay with the cube of the distance from the source (see eq.2.1).
- Radiating near-field (Fresnel) region ($R_1 < r < R_2$): radiation fields dominate, but strongly dependent upon the distance from the source and the observation angle. Indeed distances and angle between the observer and the parts of the antenna can vary considerably, thus varying proportionally phase and amplitude of the radiated fields.
- Far-field (Fraunhofer) region ($r > R_2$): where the angular field distribution is essentially independent of distance from the source. The field decays monotonically with an inverse dependence on distance.

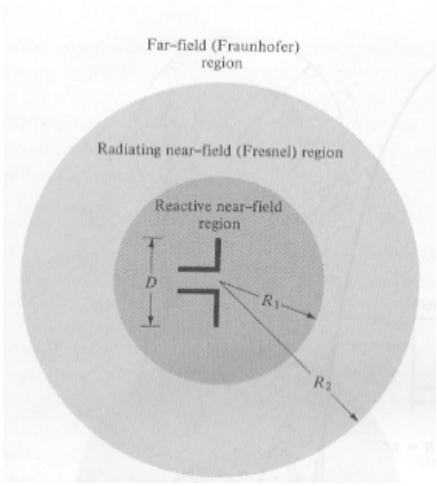

FIGURE 2.8 Reactive-, Near- and Far- Field region around a dipole of length D in free space.

The commonly accepted boundaries between the field regions are [43]

$$R_1 = 0.62\sqrt{\frac{D^3}{\lambda_0}} \tag{2.1}$$

$$R_2 = \frac{2D^2}{\lambda_0} \tag{2.2}$$

When receiving antenna systems are considered, it is generally assumed that the receiver is located in far-field region with respect to the emitter, i.e., at distances above R_2. However, when the receiving antenna is placed in the near- or reactive- field region, i.e., at distance smaller than R_2, the capacitive coupling start to predominate, especially if the receiving antenna is placed so close to the emitter to fall into the reactive field. In such a case, the sensors works as a sort of electric or magnetic field probe and the effectiveness of the signal reception depends mostly on its capacitive coupling properties with the close source. In the following work, the transformer tank will be considered as a resonant cavity wherein standing waves can be originated as a consequence of Partial Discharge events. Investigation will be carried out on the EM propagation outside the transformer through its apertures, both in far field region (irradiated waves) and in the reactive field region (electrical field perturbation close to the aperture).

2.3.1 Analytical evaluation of electric and magnetic fields within a metallic box with a circular aperture

To start with, a transformer mock up was realized in laboratory to carry out experimental irradiation tests. In particular, the irradiation pattern of a high frequency pulse generated inside a metallic box with a circular aperture on its top is investigated both inside and outside the box. The diameter of the circular aperture was chosen at 75 mm to fit the external diameter of a ceramic bushing which will be used next, to study its influence on the irradiation properties. The box was chosen 260 mm high, 240 mm large and 240 mm deep, with metallic walls 7 mm thick. The box can be considered as a shielded enclosure and its resonance frequencies can be calculated resorting to resonant cavity and waveguide theory.

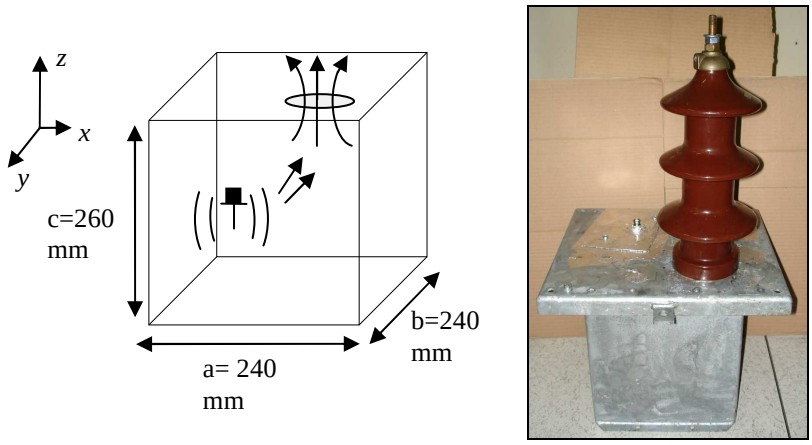

FIGURE 2.9 Metallic box used for experimental irradiation test through the aperture on its top.

In particular, it is possible to consider the box as formed by a section of rectangular waveguide (with lateral dimensions *a* and *b* laying in the *x* and *y* axis, respectively), having its back and front faces enclosed with conducting plates [42]. Various field configurations (modes) can exist inside a rectangular waveguide except the TEM (Transverse Electro Magnetic) mode, which does not satisfy the boundary conditions on the waveguide wall. On the contrary, Transverse Electric (TE) or Transverse Magnetic (TM) modes can satisfy the boundary conditions of a rectangular cavity and, consequently, of a resonant cavity derived from a section of waveguide.

There are no differences in terms of analytical treatment between rectangular waveguides and cavities in the *x* and *y* axis. Therefore, the field forms along the *x* and *y* directions and boundary conditions on the *yz* and *xz* walls are identical to those of the rectangular waveguide. On the contrary, it must be considered that, differently from the waveguide, standing waves, instead of traveling waves, exist inside a cavity along its length (*z* axis) and additional boundary conditions must be imposed along the front and back walls.

The resonance frequency $(f_r)_{mnp}^{TE}$ of the mode TE_{mnp}^{z}, where the subscripts m, n and p are designated to describe the modes along the x, y, z axis, respectively, can be evaluated as follows [42]

$$(f_r)_{mnp}^{TE} = \frac{1}{2\pi\sqrt{\mu\varepsilon}}\sqrt{\left(\frac{m\pi}{a}\right)^2+\left(\frac{n\pi}{b}\right)^2+\left(\frac{p\pi}{c}\right)^2}\quad \left.\begin{matrix} m=0,1,2,... \\ n=0,1,2,... \\ p=1,2,3,... \end{matrix}\right\} m,n \neq 0 \qquad (2.3)$$

where a, b and c are the box dimension along x, y, z axis, respectively, and μ and ε are the permeability and permittivity of the medium inside the box, respectively.

In addition to TE_{mnp}^{z} modes inside a rectangular cavity, TM_{mnp}^{z} modes can also be supported by such a structure. The corresponding resonant frequency $(f_r)_{mnp}^{TM}$ can be written as

$$(f_r)_{mnp}^{TM} = \frac{1}{2\pi\sqrt{\mu\varepsilon}}\sqrt{\left(\frac{m\pi}{a}\right)^2+\left(\frac{n\pi}{b}\right)^2+\left(\frac{p\pi}{c}\right)^2}\quad \begin{matrix} m=1,2,3... \\ n=1,2,3... \\ p=0,1,2,... \end{matrix} \qquad (2.4)$$

As can be seen in Table 2.1, the lowest frequency which can propagate inside the metallic box is 851 MHz, relevant to the TE011 mode. Thus, the system can be considered as a sort of high pass filter allowing propagation of electromagnetic waves only at frequencies higher than the cutoff frequency at 851 MHz, evaluated through eq. 2.3.

The same procedure can be carried out to work out the TE and TM resonant frequency when the box is filled with mineral oil, simulating the real oil insulated transformers. It is enough to replace the permittivity of air in (2.3) with that of the mineral oil, which can be considered constant at all frequencies (ε_{oil} = 2.3) according to [44]. TE and TM resonant frequencies

are collected in Table 2.2. It can be observed that the lowest resonant frequency is now dropped from 851 to 561 MHz, as an effect of the introduction of the oil.

TABLE 2.1 TE and TM Propagation modes – Empty box

m	n	p	TE^{z}_{mnp} Frequency [MHz]	TM^{z}_{mnp} Frequency [MHz]
1	0	1	851	/
1	1	0	/	883
1	1	1	1056	1056
2	0	1	1312	/
2	0	2	1377	/
1	2	0	/	1397
1	1	2	1453	1453
1	2	2	1812	1812
2	2	1	1859	1859

TABLE 2.2 TE and TM propagation modes - Oil filled box

m	n	p	TE^{z}_{mnp} Frequency [MHz]	TM^{z}_{mnp} Frequency [MHz]
1	0	1	561	/
1	1	0	/	582
1	1	1	696	696
0	2	1	865	/
2	0	2	907	/
1	2	0	/	921
1	1	2	958	958
1	2	2	1194	1194
2	2	1	1225	1225

Indeed, the transformer behaves like a sort of high pass filters and, in case of internal sensors design, it is important to take into account such TE and TM cutoff resonance frequencies, since no EM waves can propagate inside at frequencies below such values. In case of external sensors design, the influence of both the circular aperture and the bushing has to be taken into account as well.

When an aperture is cut in one of the conducting walls of the enclosure, it is possible that perturbation of the electric and magnetic fields outside the enclosure could be detected, both close to and far from the aperture. Further

perturbation of the fields can arise from the introduction of a dielectric material into the aperture such as the introduction of ceramic bushings into the transformer tank apertures. Therefore, in order to design external sensors, able to sense PD activities occurring inside the transformer, it is necessary to evaluate or analytically predict the perturbation of the electric and magnetic fields outside the transformer apertures.

Analytical models exist which allow to evaluate the fields radiated outside an aperture in a conducting wall [45-53]. To apply such models it is necessary to consider the aperture as a circular slot antenna, thus having a resonant frequency above that it can irradiate EM waves in the free space if properly excited by a feeding source. By considering the aperture as an antenna, the free space around the aperture can be still divided in reactive-, near- and far- field region. The boundaries between the regions can be evaluated according to (1) - (2), where D is the diameter of the aperture.

EM fields in proximity and beyond the aperture can be therefore investigated through the aperture polarizability theory, developed by Bethe [45], below the resonance frequency of the aperture, while, for frequencies higher than the fundamental resonance, waveguide theory can be used. Bethe's theory, which adopts the concept of the polazirability of an aperture, consists of replacing the aperture with electric and magnetic dipoles placed at the center of the aperture, which can be done only for apertures electrically small (i.e., when the highest frequency investigated is lower than the aperture resonance frequency). Hence, the field transmitted at the other side of the conducting wall may be considered a dipole field and can be calculated from the electric- and magnetic- dipole moments induced by the incident field on the complementary area of infinite permeability, as shown in Figures 2.10 and 2.11.

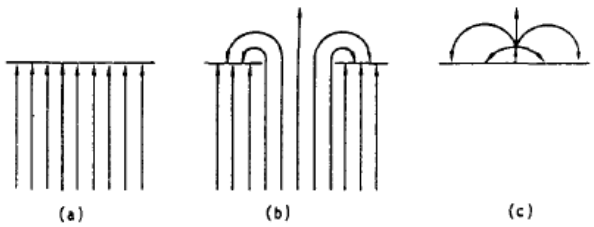

FIGURE 2.10 Electric Field aperture-coupling geometry: impressed electric field perpendicular to a metallic wall with no apertures (a), electric field near the aperture in the wall (b), equivalent electric dipole.

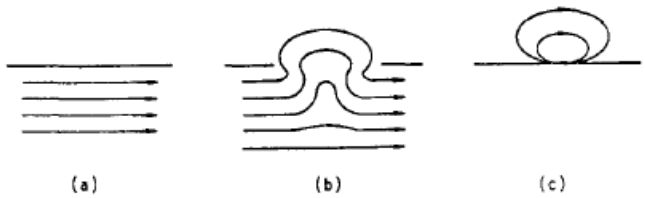

FIGURE 2.11 Magnetic Field aperture-coupling geometry: impressed magnetic field parallel to a metallic wall with no apertures (a), magnetic field near the aperture in the wall (b), equivalent magnetic dipole.

The induced magnetic and electric moments, resulting from an incident electric field normal to the plane of the aperture and from a magnetic field parallel to the aperture, respectively, are given by

$$\mathbf{P} = \alpha_e \varepsilon_0 \mathbf{E}_0 \tag{2.5}$$

$$\mathbf{M} = -\alpha_m \mathbf{H}_0 \tag{2.6}$$

Where α_e and α_m are the electric (scalar) and magnetic (vector) polarizability, respectively. The original electric and magnetic fields, ($\mathbf{E}_0$ and $\mathbf{H}_0$, respectively) inside the enclosure can be evaluated through Dyadic Green's function, at the location of the aperture (before cutting off the aperture) [45]. The values of aperture polarizability for different shapes and sizes have been determined by Montgomery [54] and Cohn [55]. In case of circular aperture, such values are collected in Table 2.3.

TABLE 2.3 Electric and magnetic polarizability for a circular aperture

Aperture shape	α_e	α_m
Circular with diameter *d*	$\frac{D^3}{6}$	$\frac{D^3}{3}$

Therefore, at frequencies lower than the aperture resonance, it is necessary, first, to evaluate the fields inside the cavity by solving Green functions (generally through complex computations programs) and, then, to use (2.5) and (2.6) to evaluate the equivalent aperture source. In such a way it is possible to get information on the electric and magnetic field close and

far from the circular aperture, evaluating the fields radiated by equivalent dipoles as:

$$\mathbf{E}(r, j\omega) = -\frac{1}{\varepsilon}\nabla\times[\mathbf{P}\times\nabla(e^{-\gamma r}/4\pi r)] + j\omega\mu\mathbf{M}\times\nabla(e^{-\gamma r}/4\pi r) \qquad (2.7)$$

$$\mathbf{H}(r, j\omega) = -j\omega\mathbf{P}\times\nabla(e^{-\gamma r}/4\pi r) - \nabla\times[\mathbf{M}\times\nabla(e^{-\gamma r}/4\pi r)] \qquad (2.8)$$

When the wavelength of the incident radiation on the circular aperture becomes comparable with the size of the aperture, it will induce a resonating current around the aperture and Bethe's theory will no longer be applicable. The transition wavelength, which can be evaluated applying the waveguide theory [50], corresponds to the cutoff wavelength of the lowest order mode of a circular waveguide having transverse section equal to the aperture in the box. The cutoff wavelength relevant to the TE11 mode, which is the lowest propagation mode in circular waveguides [48] , can be worked out as follows,

$$\lambda_{cutoff} = 3.41\, D/2 \qquad (2.9)$$

where D is the diameter of the circular aperture. It can be therefore assumed that the aperture, which behaves like a slot antenna, can irradiate in far field region EM waves in a frequency range, in general considerably narrow, around its resonance frequency. Considering the metallic box having a circular aperture with a diameter of 75 mm, it is easy to work out the aperture resonance frequency f_0 and, therefore, the transition limit between aperture polarizability and waveguide theory, through equation 2.10.

$$f_0 = \frac{c_0}{\lambda_{cutoff}} = 2.34\,GHz \qquad (2.10)$$

Summarizing, when a source inside an enclosure can excite its resonances and an aperture is into one wall, radiation both inside and outside the tank can occur. If it is aimed to investigate the radiation outside the shielded box below the aperture resonance, calculable through (2.10), electric and

magnetic field values near and far from the apertures can be worked out using Bethe's theory, which means replacing the aperture with an equivalent electric or magnetic dipole; above its resonance frequency, the aperture can considered a circular slot antenna which can irradiate EM waves around its resonant frequencies which is can be evaluated as the fundamental mode TE11 of a circular waveguide having the same section.

2.3.2 Experimental irradiation test

EM field distribution in far- and reactive- field

A series of measurements was performed on the metallic box by placing an emitting, ground plane, monopole inside and detecting the EM radiation outside the aperture through a similar receiving monopole, in order to validate the investigation carried out in 2.3.1. The length of both monopoles was chosen short enough to work below their resonance frequency (i.e., electrically small monopoles). In particular, since all the experiments were carried out in a frequency range over 2.5 GHz, 20 mm long monopoles were chosen, being the resonance frequency of such short antennas much higher (7.5 GHz) than the maximum frequency investigated, thus preventing any field perturbation due to the monopole resonances. The emitting monopole was connected to a noise generator, which produces, at its output, a white noise in a frequency range up to 3 GHz. The receiving monopole was connected to a 3 GHz Rhode & Swartz Spectrum Analyzer (SA). Sweep time was chosen at 30 kHz and resolution bandwidth at 30 kHz..

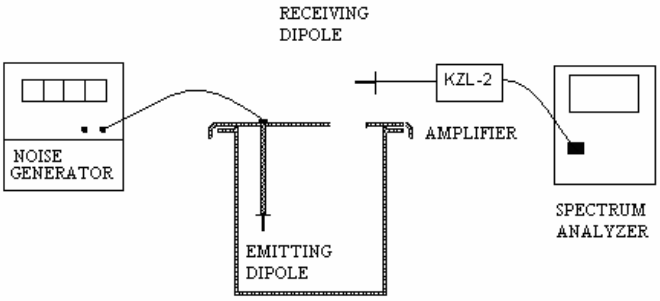

FIGURE 2.12 Experimental irradiation measurement setup

The measurement setup is sketched in Fig. 2.12. Figure 2.13 shows the noise generator spectrum when it is connected directly to the spectrum analyzer through an UHF coaxial cable.

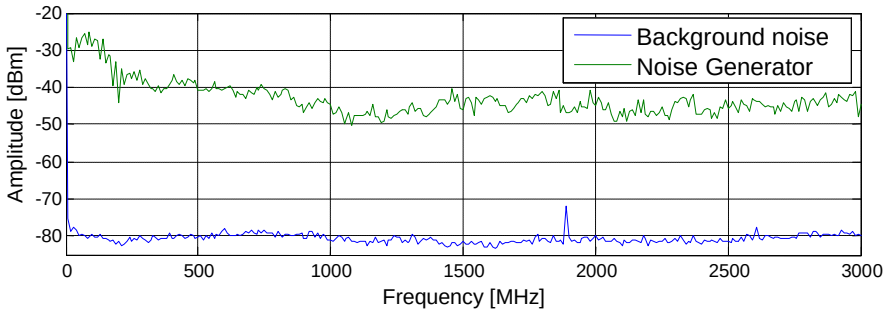

FIGURE 2.13 Signal produced at the output of the noise Generator when connected directly to the spectrum analyzer.

The emitting monopole was placed 15 mm far from the aperture and 15 mm far from both the side walls. The receiving monopole was placed outside the box at a distance, *d*, of 10 mm and 200 mm from the aperture simulating reactive and far field conditions. Indeed, considering the aperture as a slot antenna with maximum dimension D=75mm, it can be evaluated, according to (2.1) and (2.2) that the reactive field region ends at R_1=35 mm from the aperture, while the far field region starts at R_2= 87 mm from the aperture, with both R_1 and R_2 evaluated at the aperture resonance frequency. Spectra detected by the receiving monopole are shown in Fig. 2.14.

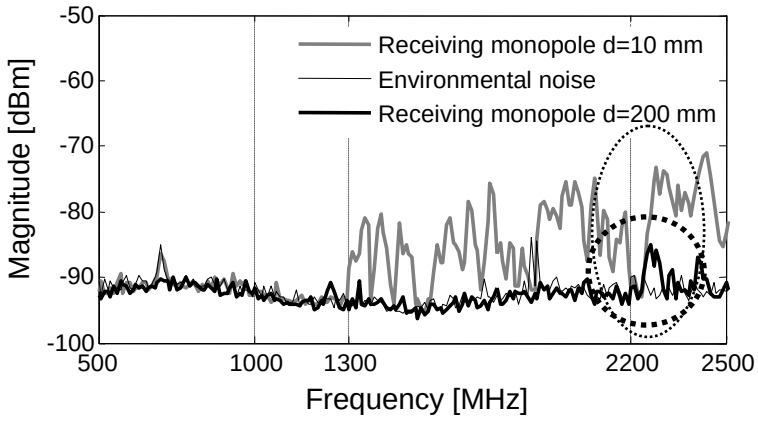

FIGURE 2.14 EM field detected outside the metallic box through an electrically small monopole in the reactive field region (d=10 mm) and in the far field region (d=200 mm).

It can be observed that when the receiver is placed 200 mm far from the aperture, in far field region, the detected frequency spectrum lies in the range between 2.2 and 2.5 GHz, i.e., significantly close to the resonance frequency of the aperture evaluated by (2.10) at 2.34 GHz.

When the receiving monopole is placed 1 cm far from the aperture, i.e., within the reactive field region, broadband spectrum can be sensed from the aperture, from 1.3 to 2.5 GHz. Indeed, resonance frequencies inside the box, relevant to the TE and TM modes, excited by the internal source, can influence significantly the electric and magnetic field in the region just beyond the aperture. Therefore, from the first experiment it is confirmed that the far-field radiation is mostly dominated by the aperture resonance, while electric and magnetic fields in the reactive region could be mostly influenced by the box characteristics.

Dependence of EM field distribution outside the aperture one oil and bushing

A further experiment was carried out on the box, by measuring the scattering parameter through a Network Analyzer (NA). The emitting and receiving monopoles were connected to the port 1 and 2, respectively, of the NA and the transmission coefficient S21 was evaluated in three different situations: box empty, box filled with oil and box with both oil filling and ceramic bushing put into the aperture. The emitting monopole was placed inside the box in the same position of the previous experiment with the Noise Generator, while the receiving monopole was placed at 5 cm far from the aperture as shown in Fig. 2.15.

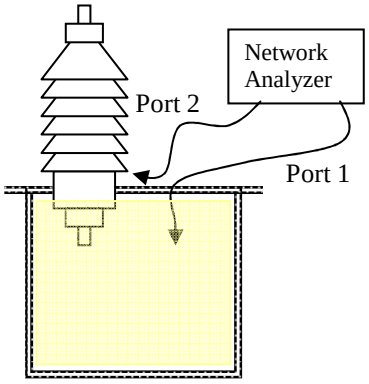

FIGURE 2.15 Sketch of the measurement setup when using two ports Network Analyzer

The purpose of the test was to verify the influence of the box internal resonances on the electric field perturbation outside the box aperture. In particular, contributes of the insertion of the oil and the bushing to such a field perturbation were investigated.

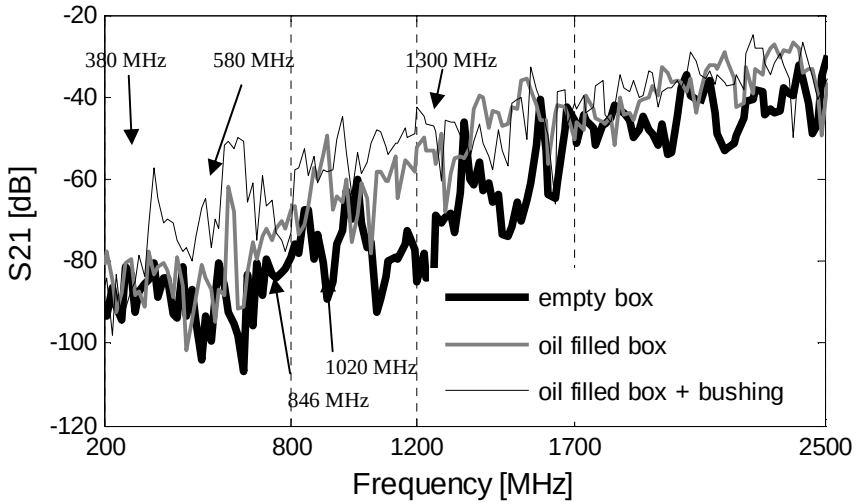

FIGURE 2.16 Insertion loss (S21) measurement through Network Analyzer between the monopole inside the metallic box and the monopole close to the aperture with the box empty, filled with oil, and with both oil filling and bushing into the aperture.

The results of the measurements are reported in Fig. 2.16 and summarized as follows:

- The first two peaks in the S21 trend relevant to the empty box are observable at 846 MHz and 1020 MHz. According to Table 2.1, such peaks correspond reasonably to the cutoff frequency of the TE10 and TE11 modes, which were evaluated approximately at 851 MHz and 1056 MHz. At 1300 MHz another peak is observable, likely relevant to the TE20 mode, with amplitude significantly higher if compared to that of the previous peaks. Indeed, when the measurement through the noise generator was carried out (Fig. 2.14), it was noticed that the first frequency component detectable above the background noise was 1.3 GHz. It is therefore possible that all the frequency components below 1.3 GHz were so low in amplitude to be completely shielded by the metallic box and completely covered by the environmental noise outside the aperture. Indeed, the NA is able to provide more energic signals, leading to significantly higher sensitivity. However, there is

good agreement between the measurement through the NA and the noise generator.

- When the box is filled with mineral oil, two main changes in the radiation pattern can be observed: the first resonant peak moved from 846 MHz to 580 MHz, according to the TE cutoff frequency collected in Table 2.2; between 800 MHz and 1700 MHz the S21 amplitude increased significantly, thus allowing radiation outside the aperture at lower frequencies if compared to the empty box results. At last, it must be noticed that no significant changes occurred above 1700. Therefore, it can be summarized that the insertion of the mineral oil influenced mostly the frequency range between 580 and 1700 MHz, resulting in a general increase of the transmitted energy within that frequency range.

- When the ceramic bushing is introduced inside the box aperture, it is possible to observe a general increase in S21 transmitted power at low frequencies. In particular, the most significant increment of S21 amplitude was found between 380 and 1000 MHz. The effect of such enhancement at low frequency is given by the combination of the dielectric properties of ceramic material in addition to the presence of the central conductor within the bushing. Indeed, when a wire penetrates a resonant cavity, an induced current flows in the conductor exciting new frequencies correlated with the position of the source inside the cavity with respect to the wire, with the cavity size and with the wire length, as shown in [56-57]. This effect is particularly significant at lower frequencies, where the wire exhibits its resonance. Note that the first resonance dropped from 580 to 380 MHz, which is roughly the resonant frequency value of the part of conductor leaning out of the tank (38 cm long).

The main result given by the measurement carried out through the Network Analyzer is that the insertion of both the mineral oil and the ceramic bushing does not influence the transmission coefficient above 1700 MHz. It is therefore possible that irradiation above such frequency is mainly due to the aperture in the box excited by the box higher resonances modes. Indeed, the higher TE and TM propagation modes inside the box, with cutoff

frequency relatively close to that of the aperture, can enhance the electric field outside the box near the aperture and, thus, be detected through proper sensors placed close to the aperture. On the other side, it is clear that both the oil and the bushing can influence significantly the S21 parameter below 1700 MHz. In particular, between 800 and 1700 MHz major increase occurred when the box was filled with oil, while between 300 and 800 MHz the highest contribute to the irradiation was given by the introduction of the ceramic bushing. Table 2.4 summarizes the results.

TABLE 2.4 Dominant effects on irradiation

300-800 MHz	800-1700 MHz	1700-2500 MHz
Bushing + Conductor	Mineral oil	Circular Aperture + Box resonances

According to the results obtained from the experimental tests it can be speculated that:

- The circular aperture at the top of the tank behaves like a slot antenna which can radiate outward electromagnetic waves in far field region within a narrow frequency range around a fundamental resonant frequency which can be evaluated through equation 2.10. An electric monopole placed inside the shielded enclosure can excite the resonances of both the enclosure and the aperture. Antenna sensors could be properly designed to detect such irradiation in far field region by matching the resonance frequency of the aperture.

- If the receiving monopole is placed near the aperture, within the near- or reactive- field region, it is possible to sense the EM field variation close to the aperture in a wide frequency spectrum due to the contribute of both the aperture and the internal resonances of the metallic enclosure. In particular, higher TE and TM modes can contribute significantly to the electric field outside the box near the aperture. As an example, it has been shown in Fig. 2.14 that, by placing the receiving monopole 20 mm far from the aperture, it was possible to detect frequency components from 1.3 GHz, i.e. well below the resonance frequency of the aperture (approximately at 2.3 GHz).

- Through measurements by means of the Network Analyzer it has been ascertained that the introduction of the oil and the bushing does not influence the frequency spectrum above 1700 MHz. On the other side, it can enhance significantly the coupling at lower frequencies. In particular, it has been found that coupling between the internal and external monopoles has been generally improved between 800 and 1700 MHz due to the presence of the oil and between 300 and 800 due to the introduction of the bushing.

It is therefore possible, for PD detection purposes, to design either proper antennas able to detect the irradiation from the transformer apertures in far-field region, or proper sensors, placed close to the aperture (i.e., in the reactive-field region), able to detect the EM field perturbation in a broadband frequency range. The first solution is the simplest in terms of computation and design since, once the size of the aperture is known, it is enough to apply equation 2.8 and design a narrow bandwidth antenna matching the resonance frequency of the aperture, f_0. On the other side, working in far field region could present evident disadvantages during on-field PD detection. As an example, an antenna properly designed to work in a narrow bandwidth around a central frequency f_0 , can sense external disturbances or PD phenomena related to other systems, especially in a substation, where the system under test can be near to HV overhead lines or HV cable outdoor terminations where corona phenomena generally occur. Hence, both the Signal-to-Noise-Ratio (SNR) and localization accuracy can be significantly reduced. Furthermore, detection within a wide frequency spectrum is generally to be preferred to narrow band systems, since a larger number of information relevant to the PD phenomenon can be collected, thus improving identification and localization effectiveness. For these reasons, PD detection carried out within the reactive field region by placing sensors close to the transformer apertures is to be preferred. Analytical methods and simulation tools are investigated in the following in order to predict the EM field distribution within the reactive field region close to the transformer apertures.

2.3.3 Analytical model of a shielded enclosure with a circular aperture

Several problems relevant to shielding effectiveness of metallic enclosures with apertures in the walls are treated in literature [58-61]. The problem is generally studied taking into account a planar EM wave which illuminates the enclosure from outside and a receiving dipole placed inside the enclosure detecting the EM waves which penetrate through the apertures. The ratio between the electric field measurable in correspondence of one point inside the enclosure, both in presence and in absence of the shielding box, is then evaluated. The Shielding Effectiveness (SE) can be then calculated according to equation 2.11, where E_0 and E_P are the electric field value in correspondence of a point P inside the cavity without and with the enclosure, respectively. The SE values are calculated for a large range of frequency.

$$SE = 20\log\left|\frac{E_0}{2E_P}\right| \tag{2.11}$$

The problem can be treated analytically resorting to the model developed by Robinson et al., where the enclosure is considered as a short-circuited length of rectangular waveguide and the aperture as a length of coplanar strip transmission line shorted at both ends [58-62]. In particular, this analogy has been explored for the dominant TEl0 mode by Dawson et al. [63] in the context of radiated emissions, and by Robinson et al. [58-61] in the context of shielding effectiveness investigation. Further extension of the model allowed De Smedt et al. [64] to develop the transmission line analogy for the TEI0 mode in case of many apertures. Other modes than TE10 were then studied by Konefal [65] along with the coupling between two electric monopoles inside an enclosure. The electric field of each mode is assumed to be proportional to the voltage on its analogous transmission line. Therefore, by choosing appropriate values for characteristic impedances of the modeled transmission line, it is indeed possible to obtain the proportionality constants relating the electric field to the voltage and evaluate Shielding Effectiveness through (2.11). Once the equivalent circuit of both the enclosure and the aperture are determined, the values of the

voltage in correspondence of the point P within the enclosure can be calculated through Thevenin circuit reduction method.

Analytical model similar to that developed by Robinson will be used in the following, but with two main differences: the source will be represented by an electric monopole with its internal impedance, thus modeled through an equivalent monopole circuit and it will be placed inside the enclosure, thus evaluating the electric field detected from a receiving monopole in a point P external to the enclosure,

In particular, the four element equivalent circuit developed by Tang et al. in [66] and shown in Fig. 2.17 can be used for modeling the feed-point impedance of the electric monopole inside the cavity. The advantage of this simple model is the ability to represent the monopole antenna at frequencies below its resonance. Indeed, the equivalent circuit takes into account only the physical dimension of the monopole and it is independent of the frequency of operation. Empirical equations allow working out the four elements as follows:

$$C_1 = \frac{12.0674h}{\log(2h/a) - 0.7245}\ pF \tag{2.12}$$

$$C_2 = 2h\left\{\frac{0.89075}{[\log(2h/a)]^{0.8006} - 0.861} - 0.02541\right\} pF \tag{2.13}$$

$$L = 0.2h\left\{[1.4813\log(2h/a)]^{1.012} - 0.6188\right\}\mu H \tag{2.14}$$

$$R = 0.41288[\log(2h/a)]^2 + 7.40754(2h/a)^{-0.02389} - 7.27408\,k\Omega \tag{2.15}$$

where h and a are the length and radius of the monopole, respectively, expressed in meter. The monopole internal impedance evaluates through the model is shown in Fig. 2.18.

The simplest prediction of the transmission parameters between the two monopoles can be found by considering only one mode of the rectangular waveguide, i.e., the dominant TEl0 mode. The metallic box with the circular aperture is sketched in Fig. 2.19, while Fig. 2.20 shows its equivalent circuit, where *a*, *b*, *d* are the dimensions of the metallic box, P is the point where the source is placed, A is the point where the electric field is evaluated, *x* is the distance between the aperture and the point P, *r* is the radius of the circular

aperture, *t* is the wall thickness, *Z0* is impedance of the air (377 Ω), *Zg* and *Kg* are the impedance and propagation constant, respectively, of the short circuited waveguide for the TE01 mode, *Zap* is the aperture impedance, *Zin* is the internal impedance of the monopole evaluated with (2.12) - (2.15) and *Vs* is the voltage across the feeding monopole.

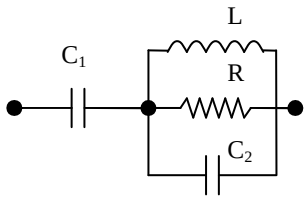

FIGURE 2.17 Equivalent circuit representing an electric monopole

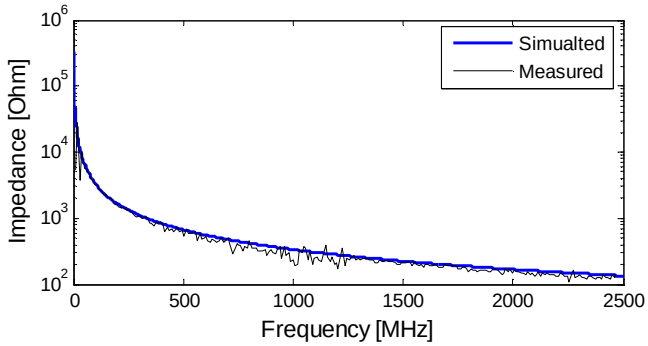

FIGURE 2.18 Comparison between measured and simulated monopole impedance

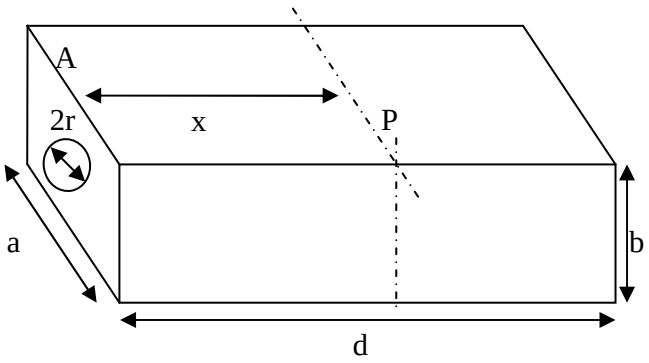

FIGURE 2.19 Rectangular box with a circular aperture, representing the metallic box

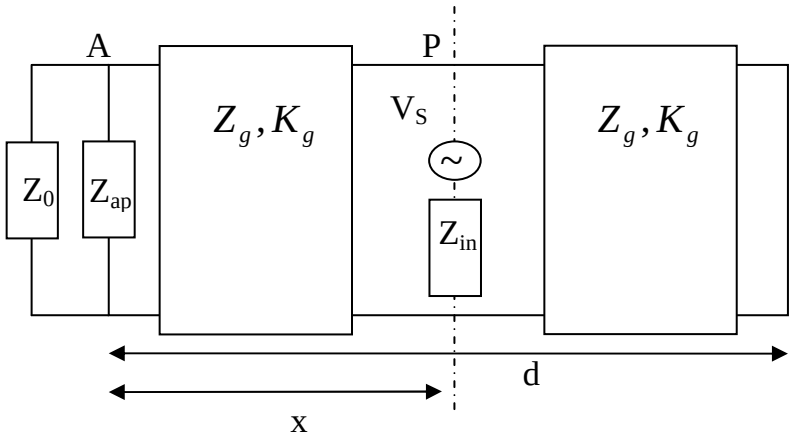

FIGURE 2.20 Equivalent circuit of the rectangular box

The slot impedance Zap can be worked out by (2.16)-(2.18), where Z_{0S} is its characteristic impedance given by Gupta et al. [67].

$$Z_{ap} = \frac{1}{2}\frac{l}{a} jZ_{0s} \tan(k_o l/2) \tag{2.16}$$

$$Z_{0S} = 120\pi^2 \left[\ln\left(2\frac{1+\sqrt[4]{1-(w_e/b)^2}}{1-\sqrt[4]{1-(w_e/b)^2}} \right) \right]^{-1} \tag{2.17}$$

$$w_e = w - \frac{5t}{4\pi}\left(1+\ln\frac{4\pi w}{t}\right) \tag{2.18}$$

$$Z_g = \frac{Z_0}{\sqrt{1-\left(\frac{\lambda}{2a}\right)^2}} \tag{2.19}$$

$$k_g = \frac{k_0}{\sqrt{1-\left(\frac{\lambda}{2a}\right)^2}} \tag{2.20}$$

$$Z1 = jZ_g \tan(k_g(x-d)) \tag{2.21}$$

$$V2 = V0\frac{Z1}{Z1+Z0} \tag{2.22}$$

$$Z2 = \frac{ZoZ1}{Z1+Z0} \tag{2.23}$$

$$V3 = \frac{V2}{\cos(k_g x) + j(Z2/Z_g)\sin(k_g x)} \tag{2.24}$$

$$Z3 = \frac{Z2 + jZ_g \tan(k_g x)}{1 + j(Z2/Z_g)\tan(k_g x)} \tag{2.25}$$

$$V4 = V_A = V3\frac{Zap}{Zap + Z3} \tag{2.26}$$

$$S21 = 20\log\left|\frac{V_0}{2V_A}\right| \tag{2.27}$$

Note that equations 2.16 – 2.18 account for a rectangular aperture with length *l* and width *w*. It can be assumed during the calculation that circular apertures behave similarly to square apertures, as demonstrated in [67]. Therefore it can be approximated $w = l = r\sqrt{\pi}$, where *r* is the radius of the aperture. The characteristic impedance and propagation constant of the short circuit waveguide can be evaluated through (2.19) and (2.20), where k0 is the characteristic propagation constant of the air (k0= 2π / λ). Thevenin's reduction equations are described in (2.21)-(2.26), where the equivalent circuit at the aperture can be described through the equivalent impedance Z3 and the equivalent generator V3, as shown in Fig. 2.21. At last, the transmission coefficient can be evaluated through equation (2.27), where V_S is the voltage source and VA is the voltage at the aperture site.

The result of the simulation for the empty box is plotted in Fig. 2.22. Note that it is possible to recognize clearly the resonance frequencies of the box approximately at 850 and 1300 MHz, as evaluated in the previous paragraphs. Furthermore, there is an emission peak in correspondence of the circular aperture resonant frequency, i.e., at about 2200 MHz. It is also possible to observe that below the first resonance of the box the attenuation is strong enough to not allow any frequency to be detected from the aperture.

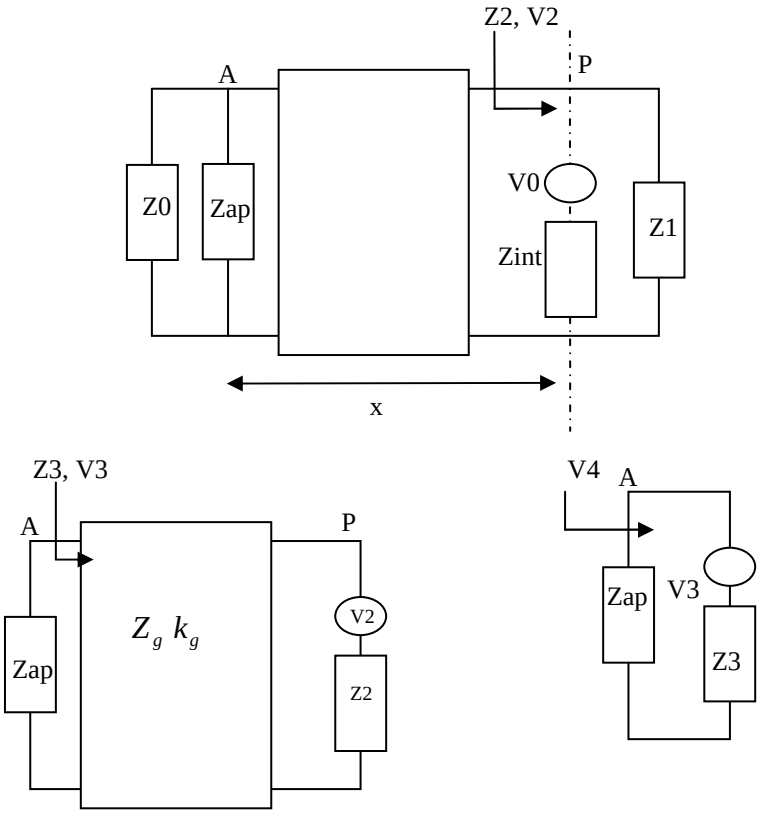

FIGURE 2.21 Thevenin circuit reduction.

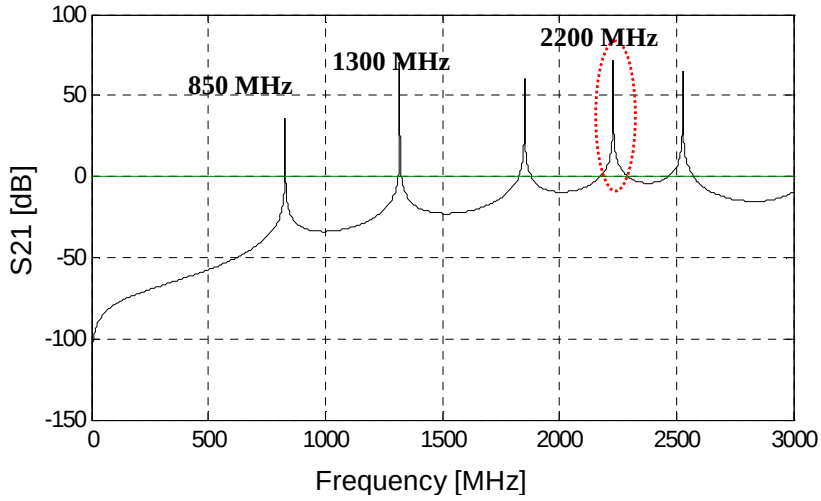

FIGURE 2.22 S21 parameter between the emitting and receiving monopoles predicted by the analytical model

The model can be used also in presence of the mineral oil, as shown in Fig. 2.23, just changing properly Kg and Zg by the introduction of the relative permittivity of the oil.

Note that in both the empty and oil-filled box, the highest emission peak is in correspondence of the aperture resonance, i.e. approximately around 2200 MHz. As shown in Fig. 2.23, the analytical model can also predict the internal resonance of the box in presence of oil, being the first peak moved from 850 to 550 MHz, according to the results obtained in the previous paragraphs.

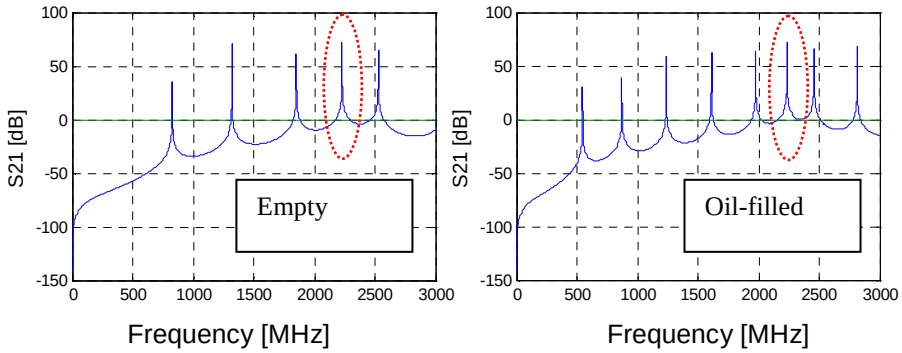

FIGURE 2.23 Comparison between S21 parameter predicted by the analytical model with the box empty (left) and filled with oil (right)

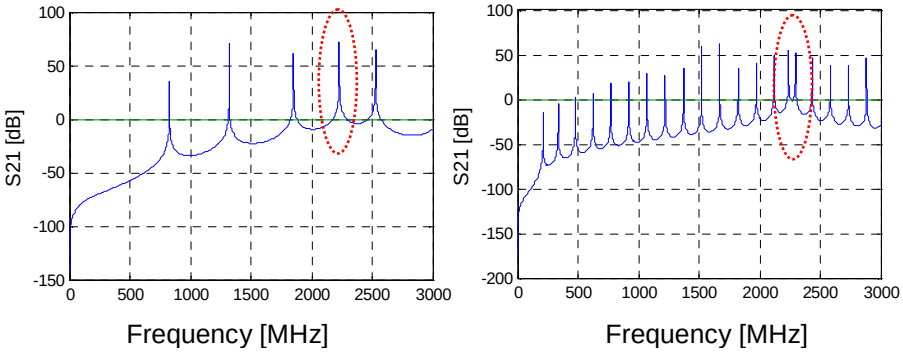

FIGURE 2.24 Comparison between S21 parameter predicted by the analytical model for a (0.24 x 0.24 x 0.26 m) and a (1 x 1 x 1 m) metallic box with the same aperture

At last, the analytical model can be used to investigate systems having different sizes. Figure 2.24 shows the difference between the metallic box and a bigger enclosure (1 m x 1m x 1m) having the same circular aperture. Higher number of internal resonances can be observed inside the bigger box

due to a lower TE10 cutoff frequency. It can be still noticed the presence of an irradiation peak, outside the aperture, in correspondence of the aperture resonant frequency.

2.3.4 Simulations using CAD systems

Computer Aided Designed softwares, aimed at EM field simulation, exist, which can based on the Finite Element Method [68-69], i.e., a numerical techniques suitable for finding approximate solutions of partial differential equations as well as of integral equations. The solution approach is based either on eliminating the differential equation completely (steady state problems), or transforming the partial differential equations into an approximating system of ordinary differential equations, which can be then numerically integrated using standard techniques (i.e., Euler's method or Runge-Kutta, etc). Basically, the infinite dimensional linear problem is replaced with a finite dimensional version in a discretization process through a creation of a mesh grid which includes finite elements with well known geometries and characteristics. The solution within each element is assumed to be a linear combination of well known shape functions. The simulation accuracy can be increased significantly with the number of mesh (in the detriment of the duration of the simulation). In order to carry out simulations able to describe the electric field distribution outside the metallic box, the CST Microwave Studio software was chosen. The metallic box can be thus modeled accurately and two discrete ports can be used for simulating both the receiving and emitting monopoles. The emitting monopole has been placed in the same position of the real one used in the experiments on the box, while the receiving monopole has been placed 20 cm far from the aperture, according to the experimental tests carried out with the noise generator. Irradiation properties at four chosen frequencies are investigated (750, 1500, 2200 and 2500 MHz). The simulation results are shown in Fig. 2.25, where the color bar at the right side of each figure indicates the intensity of the electric field.

It can be observed that:

- At 750 MHz, variations of the electric field did occur neither in the far field region nor in the close proximity of the aperture.
- At 1500 MHz, there are no variations in the far field region. On the contrary, it is possible to note the perturbation of the electrical field

just outside the box, in proximity of the aperture, according to Fig. 2.14.

- At both 2200 and 2500 MHz, i.e., approximately around the aperture resonance, radiation in far field region occurs, according to Fig. 2.14. The radiation is stronger, as expected, at 2200 MHz.

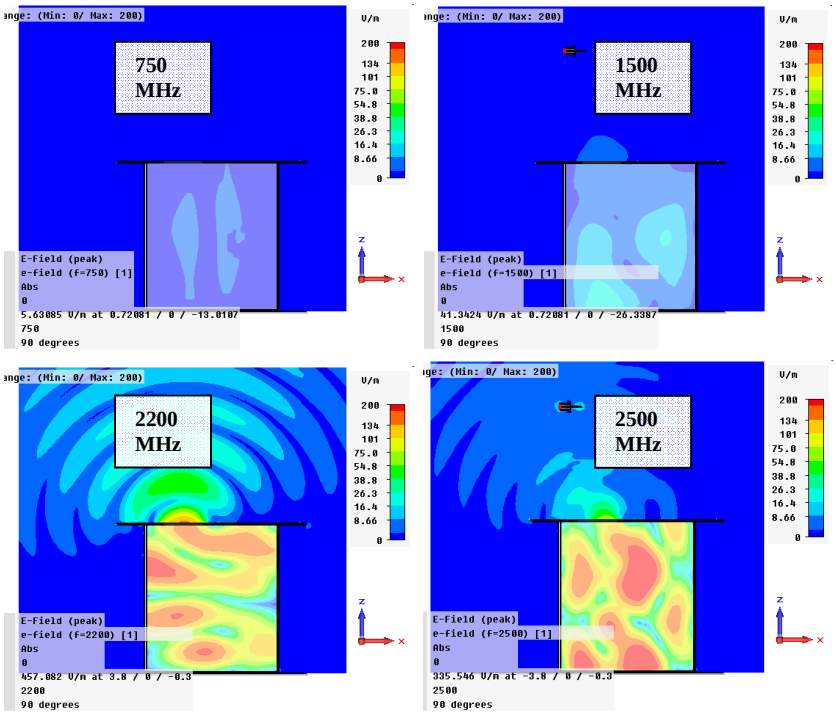

FIGURE 2.25 Emission properties simulated for a metallic box excited by an internal electric source

The simulation results show excellent agreement with the experimental data. In particular, all the considerations done after the experimental test with the noise generator are here confirmed, i.e.: detection in far field region is allowed only at frequencies close to the aperture resonance; detection in near field region is possible well below the aperture resonant frequency (approximately from 1300 MHz) and over a wider frequency range.

Further simulations were carried out filling the box with oil and introducing the bushing into the aperture. The transmission coefficient was simulated between the monopole inside the box and a receiving monopole 5 cm far from the aperture according to the measurement setup shown in Fig. 2.15. The results (Fig. 2.26) show very good agreement with those obtained in 2.3.2 and collected in Fig.2.16.

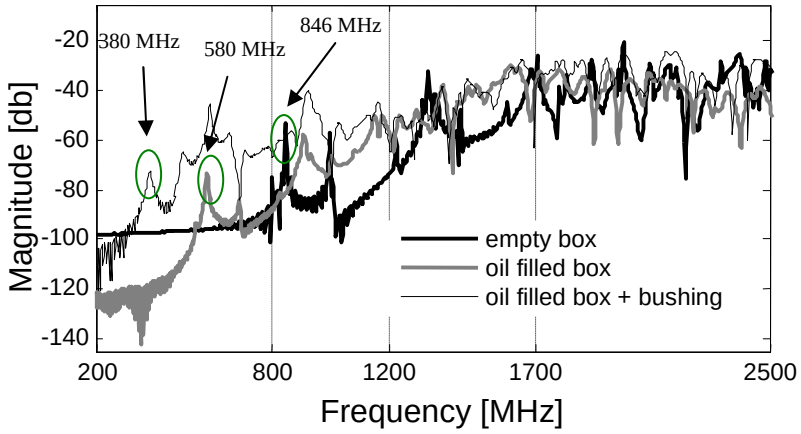

FIGURE 2.26 S21 simulation between the monopole inside the metallic box and the monopole close to the aperture with the box empty, filled with oil, and with both oil filling and bushing into the aperture.

In particular, it can be observed that:

- The first resonance peak of the empty box is at 846 MHz, due to the TE101 fundamental resonant. Maximum coupling between the two monopoles starts above 1300 MHz, similarly to Fig. 2.16.
- The introduction of the oil leads to a general increase between 800 and 1700 MHz and to a drop of the first resonance peak from 846 to 580 MHz, according to the experimental results collected in Fig. 2.16.
- The bushing insertion leads to a coupling increase at lower frequencies. In particular, the first resonance can be observed at 380 MHz, in accordance with Fig. 2.16.
- Maximum coupling between the two monopoles occur above 1700 MHz, where the transmission coefficient is not influenced significantly by the introduction of the oil and the bushing.

The patterns obtained from the simulations, showing the electrical field values inside the box, close to the aperture and in far field region are collected in Figs. 2.27-2.29

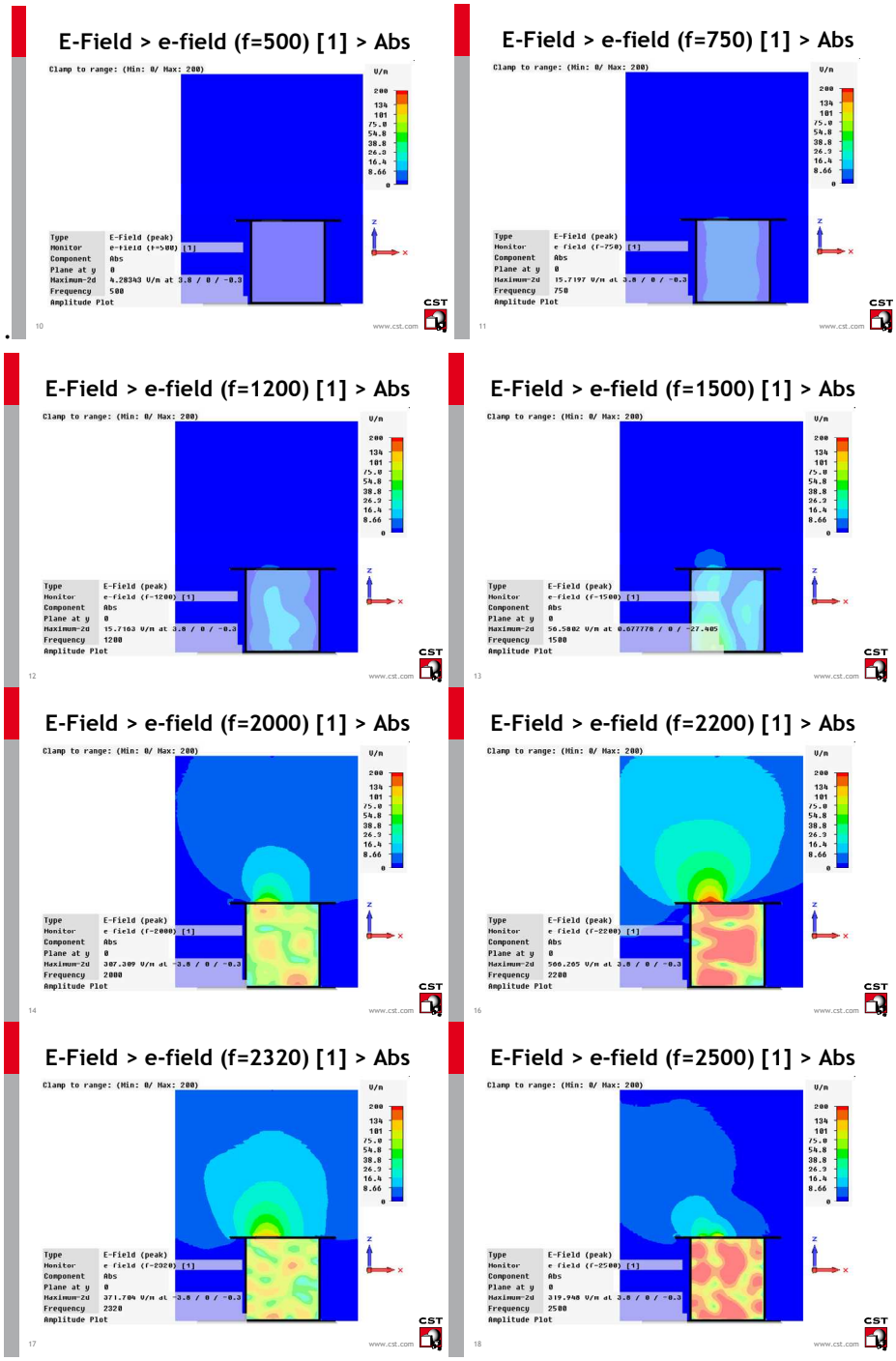

FIGURE 2.27 Simulated irradiation pattern inside and outside the metallic empty box. Note that the maximum electric field value outside the aperture is at 2200 MHZ, i.e. at about its resonant frequency.

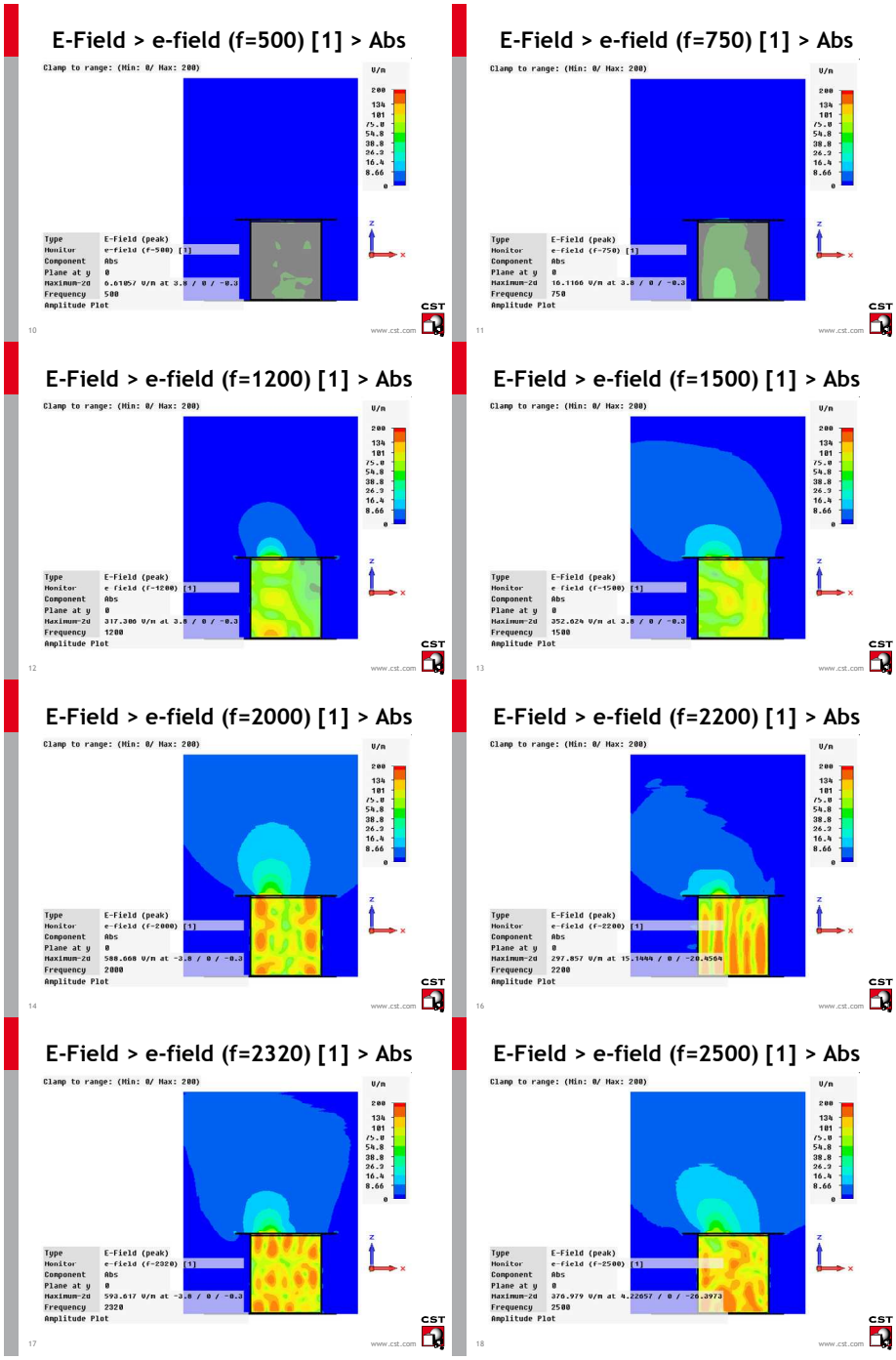

FIGURE 2.28 Simulated irradiation pattern inside and outside the metallic oil filled box. Note that higher values of electric field can be detected outside the aperture at lower frequency compared to the empty box, due to the influence of the oil on the TE and TM modes inside the box.

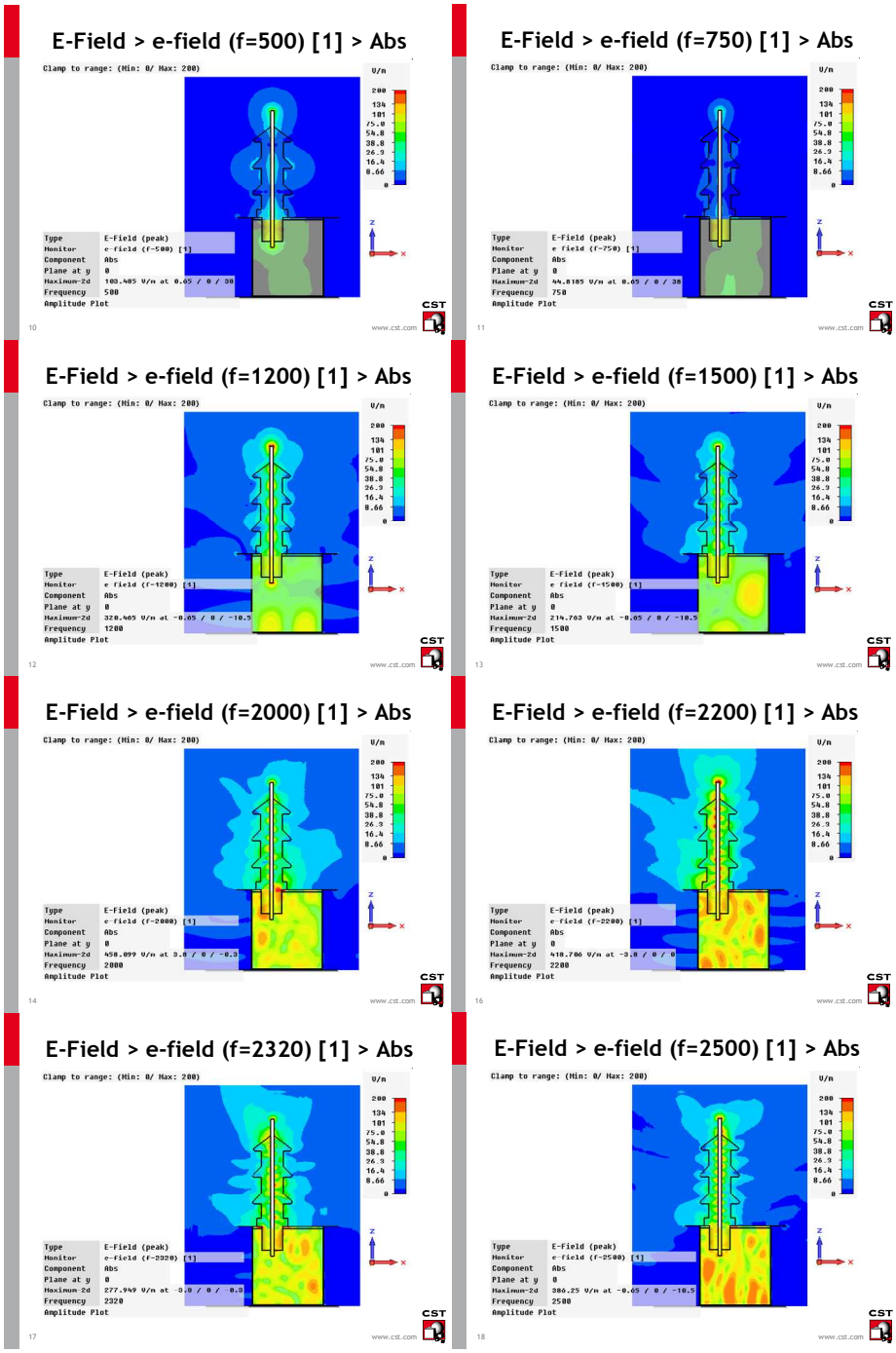

FIGURE 2.29 Simulated irradiation pattern inside and outside the metallic oil filled box with bushing. Note that higher values of electric field can be detected outside the aperture already at 500 MHz due to the induced current traveling along the bushing conductor.

2.4 Investigation of PD irradiation properties of a three-phase distribution transformer

Experimental and simulation tests were carried out on a real three-phase oil insulated transformer, in order to verify the simulation tool, effectiveness even in presence of the magnetic core and the windings.

TE and TM propagation modes inside the transformer tank can be evaluated resorting to equation 2.3 and 2.4, even in presence of the mineral oil. The cutoff frequencies for TE modes inside a shielded cavity having the same dimensions of the transformer under test (770 x 285 x 585mm) are collected in Table 2.5. Oil filling is already taken into account.

TABLE 2.5 Te Propagation Mode Inside The Transformer Under Test

m	n	p	TE^{z}_{mnp} Frequency [MHz]	TM^{z}_{mnp} Frequency [MHz]
1	0	1	212	/
1	1	0	/	370
0	1	1	386	/
2	0	1	307	/
0	1	1	386	/
1	1	1	406	406
2	0	2	424	/
2	1	1	463	463
0	1	2	484	/
1	2	0	/	705
0	2	1	714	/
1	2	1	725	725
2	2	1	760	760
1	2	2	782	782

It can be seen that differently from the TE modes inside the metallic box (Table 2.2), resonances occur at significantly lower frequencies, due to the bigger size of the tank.

2.4.1 Experimental irradiation tests

The transformer under test, shown in Fig. 2.30, has an oil conserver which is connected to the top of the tank through two pipes, one close to the MV bushings side and one in the LV side.

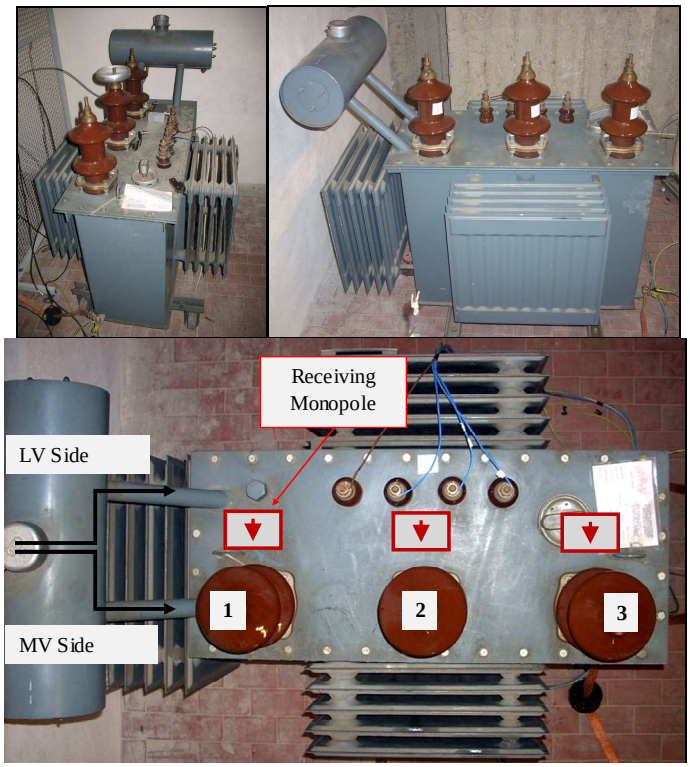

FIGURE 2.30 Pictures of the1000 kVA distribution transformer under investigation

An emitting monopole, 5 cm long, connected to the same noise generator used in the previous tests, was introduced inside the transformer tank, as sketched in Fig. 2.31, first into the conserver pipe in the MV side and, then, into the pipe in the LV side, in order to simulate a PD source occurring inside the transformer close to the MV and LV connections to the bushings, respectively. The irradiation outside the transformer was sensed through another 5 cm long monopole connected to a Spectrum Analyzer. A 20 dB high frequency amplifier was connected to between the receiving monopole and the spectrum analyzer.

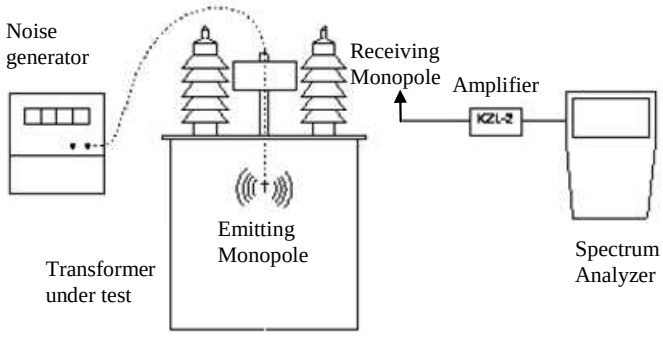

FIGURE 2.31 Measurement setup during the experimental irradiation test through Noise Generator.

Detection was carried out in correspondence of all the three bushings in order to investigate possible differences in the EM field distribution outside the tank. Figure 2.32 shows the results of the emission test when the monopole was introduced inside the tank through the pipe at the MV side. In such a case the monopole inside the tank was reasonably close to the metallic connection between the MV winding and the MV bushing. It can be observed that:

- The amplitude of the EM field sensed in correspondence bushing 1 was significantly higher if compared to that detected close to the other two bushings, being bushing 1 the closest to the source. In terms of frequency range, the lowest frequency detected above the background noise (500 MHz) is much lower than the aperture resonance (2300 MHz), likely due to the contribute at lower frequency of the ceramic bushing along with the oil, the windings and the magnetic core, according to the results collected in Table 2.2 relevant to the experimental tests on the metallic box.
- The spectrum detected close to bushing 2 is as wide as that detected close to bushing 1, but is significantly lower in amplitude, especially at frequencies below the aperture resonance. Indeed, the coupling between the source and the bushing, which generally enhances the EM field at low frequencies, is strongly reduced between the monopole and bushing 2 due to their distance. Anyway, it can be noted that the EM field outside the bushing is still high within the frequency range between 2000 and 2500 MHz, i.e., around the resonance frequency of the aperture which is likely excited by the higher propagation modes inside the tank.

- The EM field detected in correspondence of bushing 3 has even lower amplitude than that outside bushing 2 due to the larger distance from the source. However it can be noted that higher EM field amplitude can be sensed within the frequency range around the aperture resonance.

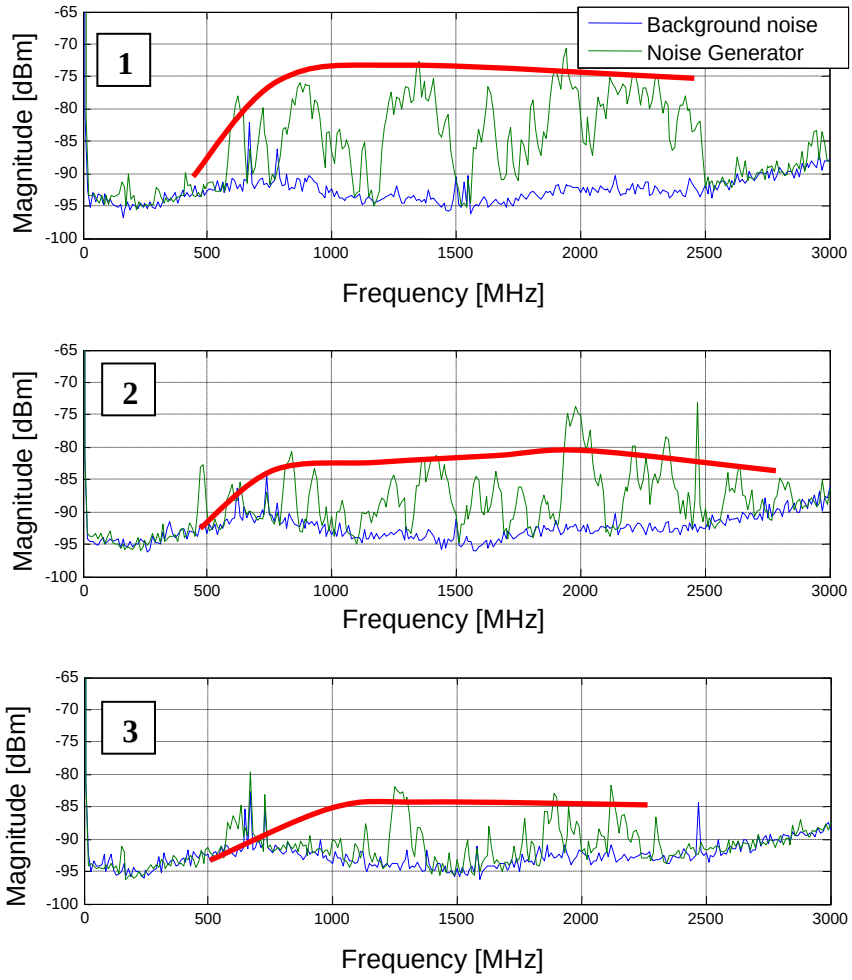

FIGURE 2.32 EM frequency components detected outside the tank at the base of the bushings during the experimental test carried out with a noise generator. Emitting monopole was placed close to the MV windings through the pipe at the MV side.Note that maximum amplitude was sensed in correspondence of the bushing 1, i.e., the one close to the source

The emitting monopole was then inserted through the pipe at LV side, simulating a source inside the transformer located at the top of the tank but far from the connections between the MV windings and the MV bushings.

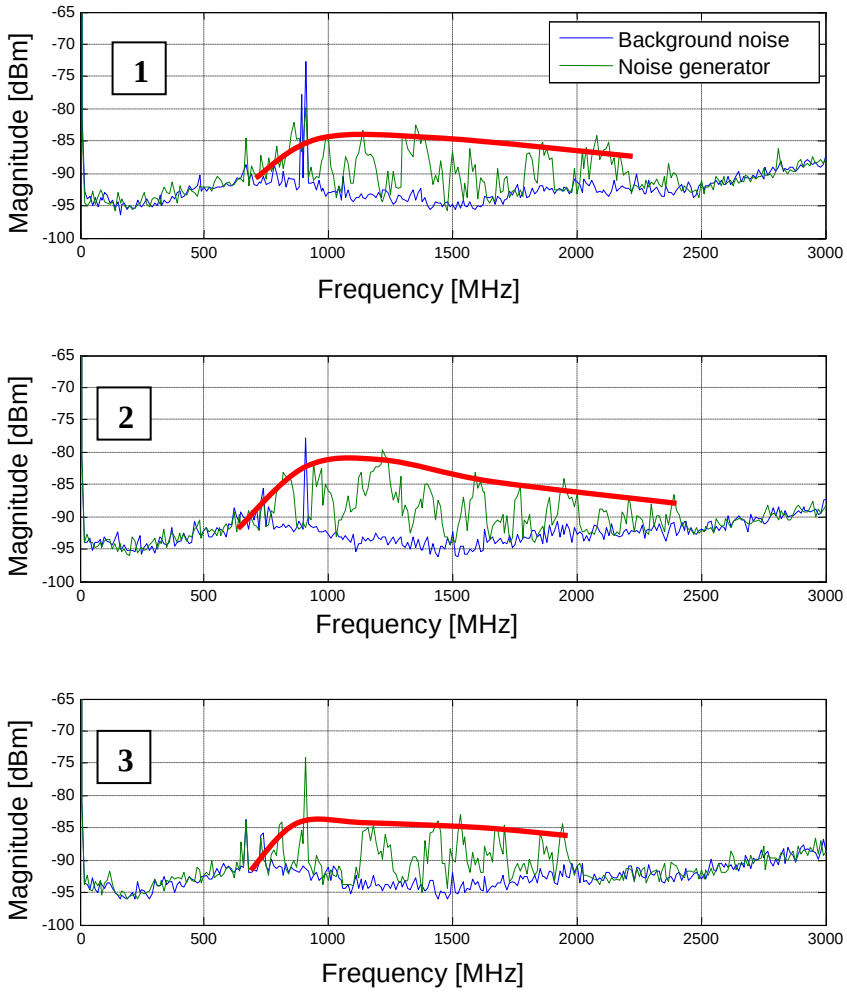

FIGURE 2.33 EM frequency components detected outside the tank at the base of the bushings during the experimental test carried out with a noise generator. Emitting monopole was placed into the pipe at LV side. Note that the amplitude is similar in all the three bushings

Results are collected in Fig. 2.33, where it is possible to note that:

- EM field was detected in correspondence of bushings 1 and 2 with similar amplitude and frequency range. A slight reduction in amplitude was noted close to bushing 3, due to the larger distance between the bushing and the source.
- The detected spectrum presented in general lower amplitude and smaller bandwidth than that measured when the monopole was placed

into the pipe at the MV side, due to the lower coupling between the source and the MV connections. Indeed, the lowest frequency where the EM field can be detected with appreciable SNR is around 800 MHz, i.e., higher than the lowest frequency sensed when the monopole was introduced into the pipe close to the MV bushing (500 MHz).

It can be therefore speculated that a source located close to the MV bushing could allow emission outside the apertures in a wider frequency range and with higher amplitude compared to a source located far from the MV bushings. In particular, EM fields are enhanced at lower frequencies (from 500 MHz) when the source is located close to the MV bushing due to the induced currents on the conductors inside the bushing.

Prediction of EM field distribution outside the transformer through the analytical model is not trivial and analytical methods described in 2.3.1 and 2.3.3 can be inadequate to describe such complex geometries. In particular, the transmission line model should take into account equivalent circuits for complex structures such as the presence of multiple apertures (three per transformers), presence of the MV and LV windings, presence of magnetic core and internal coupling between sources and windings.

On the other hand, it has been shown in 2.3.4 that CAD simulations can predict accurately the EM emission outside the aperture accounting for both the presence of oil and the bushing. Simulations will be carried out therefore in the following in order to verify their effectiveness in describing a complex structure such as a real three phase transformer.

2.4.2 Simulations using CAD systems

Effect of distance between the source and the MV conductors inside the transformer

The three phase transformer structure was designed through the CAD software, including the magnetic core, LV and MV bushings, MV and LV windings, mineral oil and mechanical supports, as shown in Fig. 2.34.

To start with, a discrete port, simulating the emitting monopole was placed inside the transformer at about 5 cm far from the top (thus, above the magnetic core) close to the MV and LV windings, in order to reproduce the experimental setup used for to the test carried out in 2.4.1. A receiving

monopole was placed, in both cases, close to the base of the first MV bushing (indicated with the number 1 in Fig 2.30).

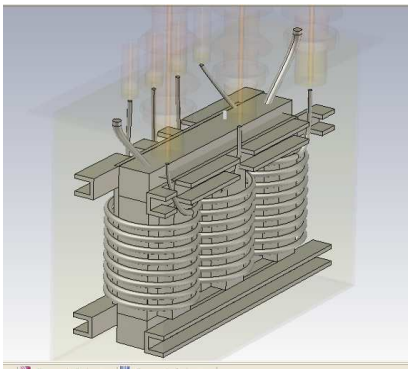

FIGURE 2.34 Tree phase transformer designed through CAD software basing on the structure of the transformer investigated in 2.4.1

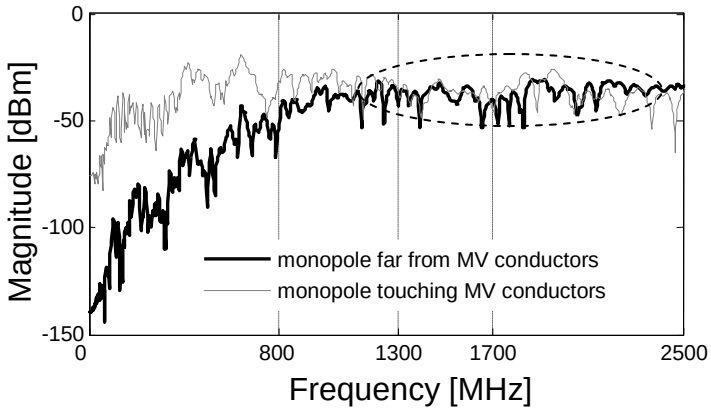

FIGURE 2.35 Irradiation from a three phase transformer simulated through CAD software

Simulation results are reported in Fig. 2.35, where it is possible to see that:

- the EM field distribution outside the bushing presents much higher amplitude in the low frequency region (<800 MHz) when the monopole is placed close to the MV conductor, due to the capacitive coupling between the source and the MV bushing.
- No significant differences can be noticed above 1300 MHz, which means that the geometrical structure of the transformer tank along with the apertures have a major role in the EM field outside the tanks in such a frequency range.

- Comparing Fig. 2.33 to 2.35, it can be noted that the simulation results fit very well the experimental results when the source is placed far from the MV conductors. Indeed it can be observed in both figures that when the source is placed far from the MV conductors the lowest detectable frequency is around 800 MHz.
- Comparing Fig. 2.32 to 2.35, it can be note that the simulation results fit very well the experimental results even when the source is placed close to the MV conductors. Indeed it can be observed in Figure 2.35 a peak in the EM emission between 500 and 800 MHz, due to the contribute of the MV conductor inside the bushing, which behaves like an antenna. Similarly, it can be noticed that EM field distribution outside the bushing starts at 500 MHz in Figure 2.32 as well. The only difference between the experimental and simulated results lies in the amplitude of the frequency components between 500 and 800 MHz. As a matter of facts, simulation shows that such components are even higher than those at high frequencies, while experimental results show that they are definitely higher than the background noise but with amplitude comparable to those at high frequency. The reason of such slight differences lies in the different position of the monopoles in the simulation and experimental setup. Indeed, the irradiation power outside the transformer strongly depends from the distance between the source and the MV connection, that is to say, on their capacitive coupling. In the case of the experimental test, it is supposed that the monopole is reasonably close to the MV conductors since evident changes in EM emission were noted between 500 and 800 MHz with respect to the case of monopole introduced into the pipe close to the LV side, but it is not possible to quantify the exact distance between the monopole and the MV connections. On the other side, simulation were carried out by placing the source touching the MV conductor, in order to maximize the coupling between the source and the bushing and emphasize its contribute to the EM field detectable outside.

Resorting to simulation and experimental results, sensors can be designed to optimize detection sensitivity. If PD detection was carried out below 800 MHz, only PD sources close to the MV windings could be detected with good SNR being the irradiation produced by the monopole placed far from the MV winding much lower than that originated by the monopole close to the windings. It is therefore convenient to carry out PD measurement within

a wider frequency range, in order to detect PD sources both close and far from the MV conductors. In particular, it could be useful, for identification and localization purposes, to design suitable detectors covering both high frequency range (>1300 MHz), where the EM field outside the aperture has been shown to have, in general, maximum amplitude, and the lower frequency range (500-1300 MHz) in order to enhance the differences between the PD phenomena, occurring close and far from the MV conductors, resorting to their different frequency spectrum.

Effect of monopole orientation and position

Further simulations were carried out placing the emitting monopole with different orientation and position within the transformer tank in order to investigate the differences in the irradiated pattern. Figures 2.36 -2.41 shows the effect of the monopole orientation on the electrical field inside and outside the transformer, evaluated at different frequencies (500, 1000, 1500, 2200 and 3000 MHz). The monopole was placed below the central bushing close to (but not touching) the MV connection between the windings and the bushing in order to investigate also the effect of three different orientations on the capacitive coupling between the source and the bushing. It is interesting to observe that the EM field distribution inside and outside the transformer can vary significantly with the orientation of the monopole. Better resolution and understanding of the results can be obtained through the 3D representation, shown in Figs. 2.42-2.45 .

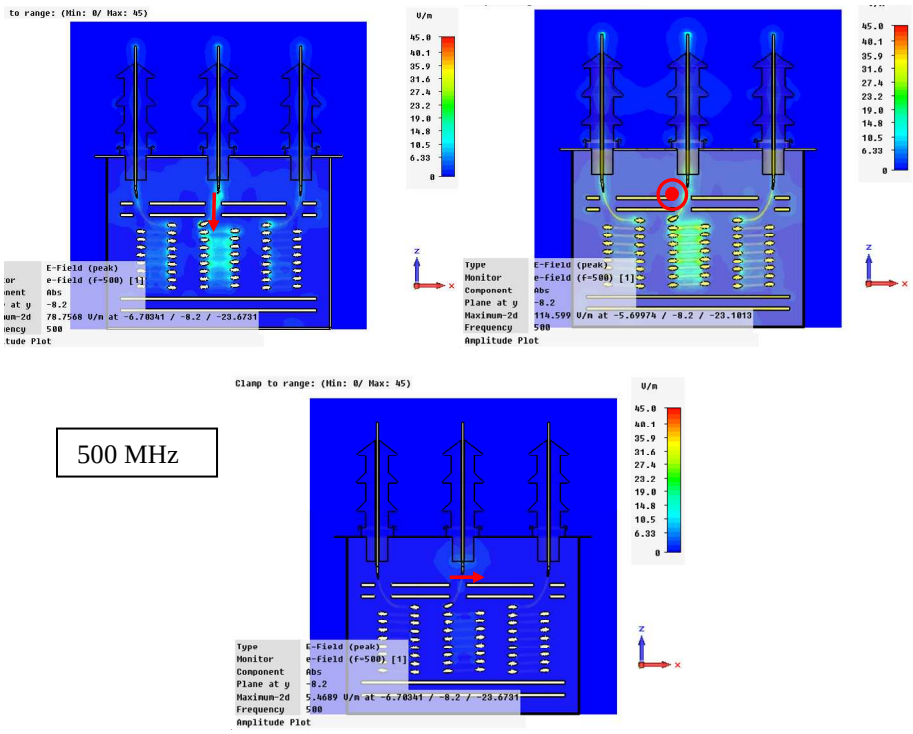

FIGURE 2.36 Simulated irradiation pattern inside and outside the three phase transformer @ 500 MHz depending on source orientation.

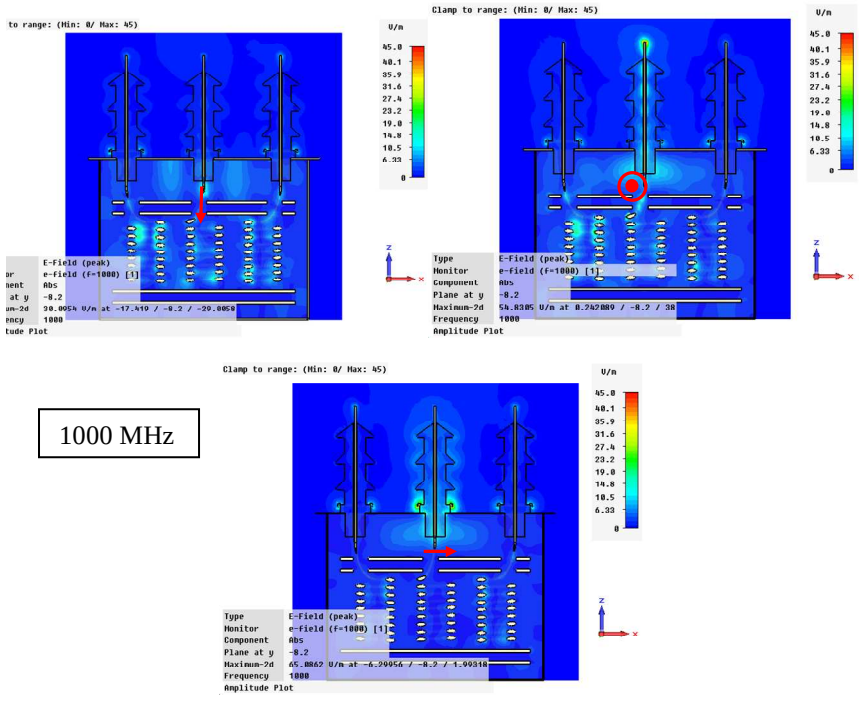

FIGURE 2.37 Simulated irradiation pattern inside and outside the three phase transformer @ 1000 MHz depending on source orientation.

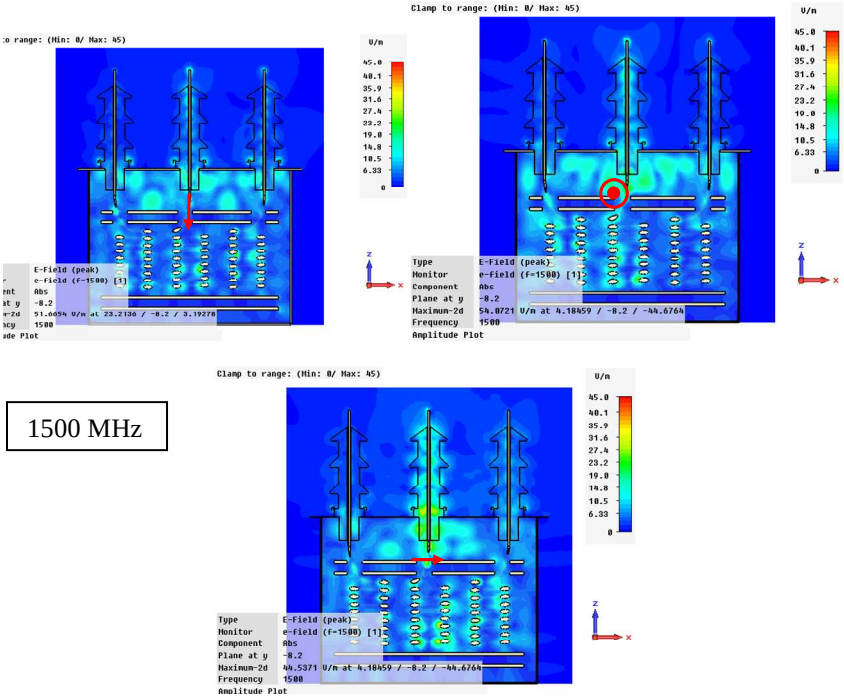

FIGURE 2.38 Simulated irradiation pattern inside and outside the three phase transformer @ 1500 MHz depending on source orientation.

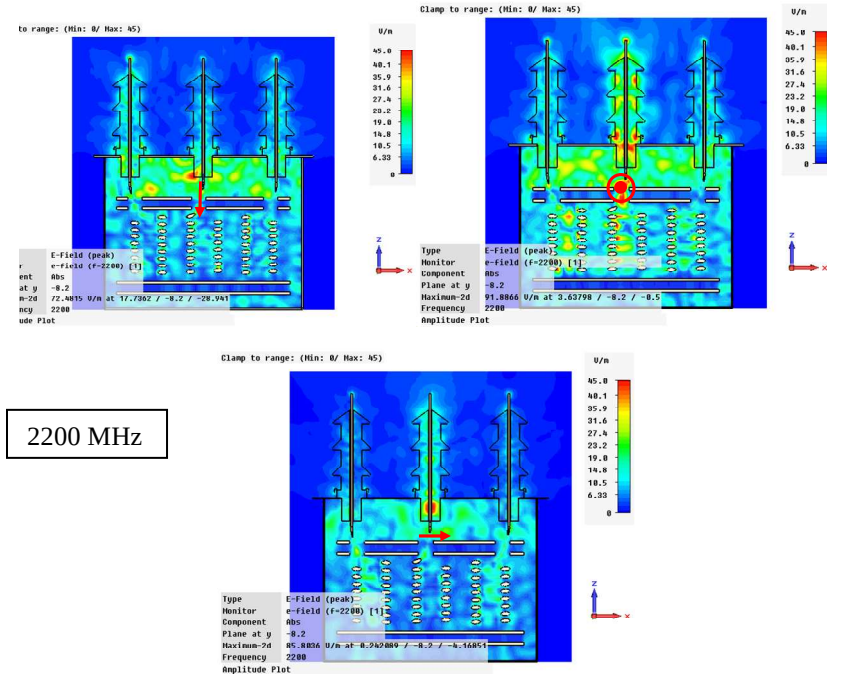

FIGURE 2.39 Simulated irradiation pattern inside and outside the three phase transformer @ 2200 MHz depending on source orientation.

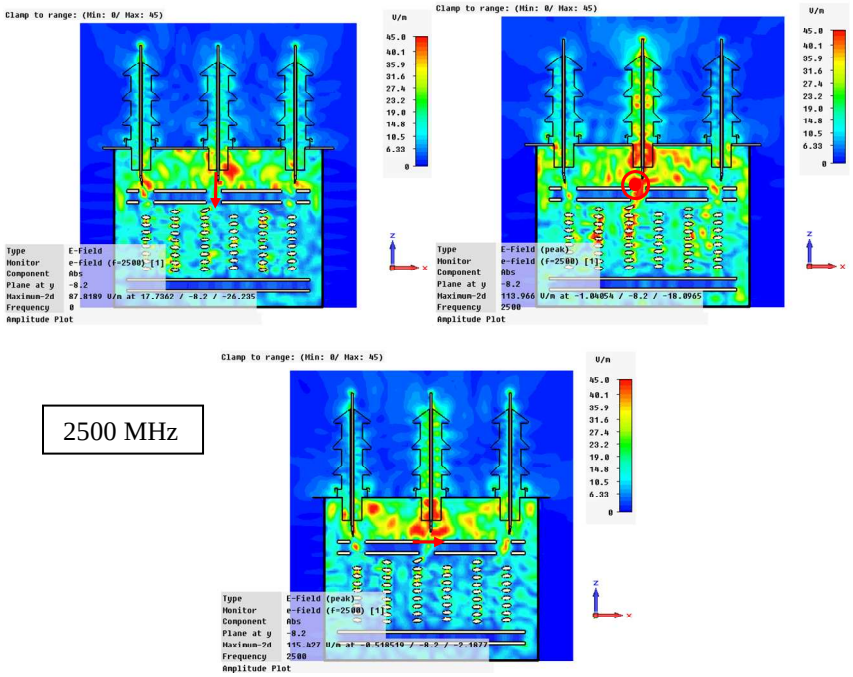

FIGURE 2.40 Simulated irradiation pattern inside and outside the three phase transformer @ 2500 MHz depending on source orientation.

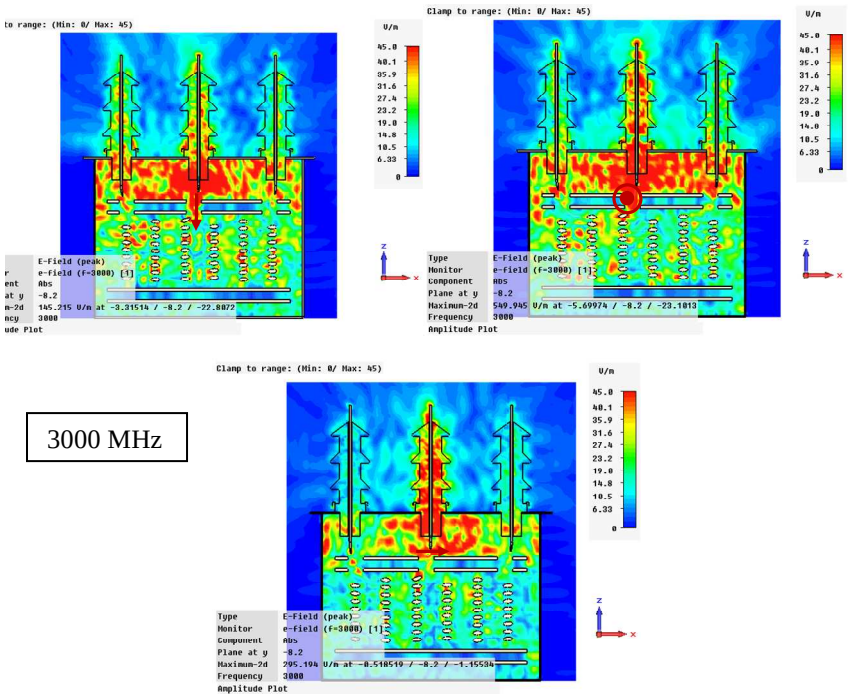

FIGURE 2.41 Simulated irradiation pattern inside and outside the three phase transformer @ 3000 MHz depending on source orientation.

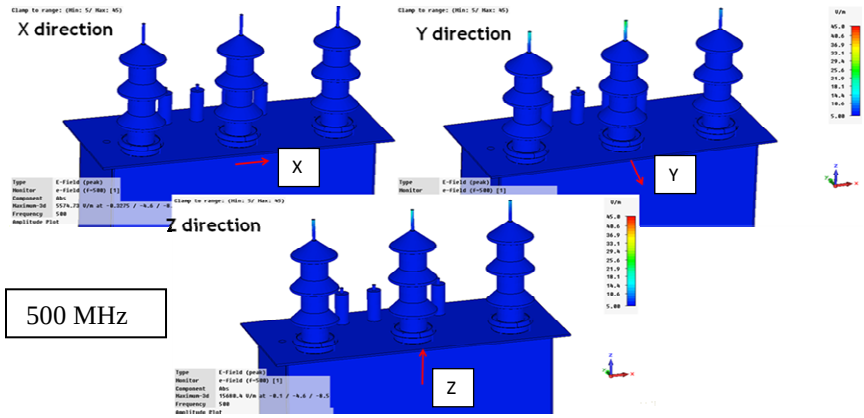

FIGURE 2.42 Simulated irradiation pattern inside and outside the three phase transformer @ 500 MHz depending on source orientation.

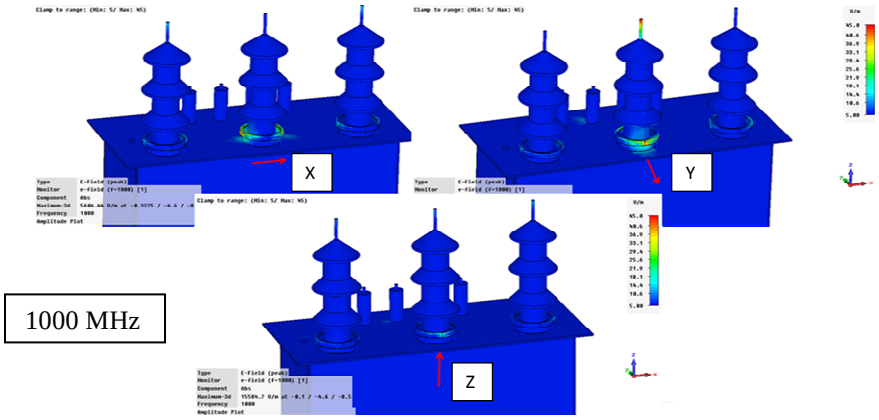

FIGURE 2.43 Simulated irradiation pattern inside and outside the three phase transformer @ 1000 MHz depending on source orientation.

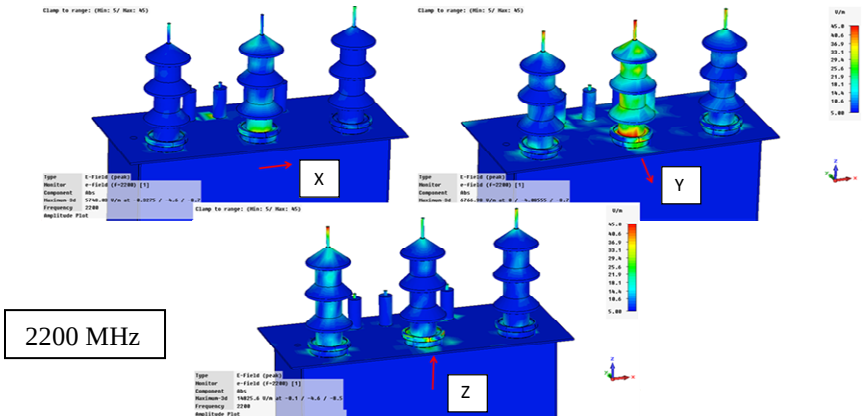

FIGURE 2.44 Simulated irradiation pattern inside and outside the three phase transformer @ 2200 MHz depending on source orientation.

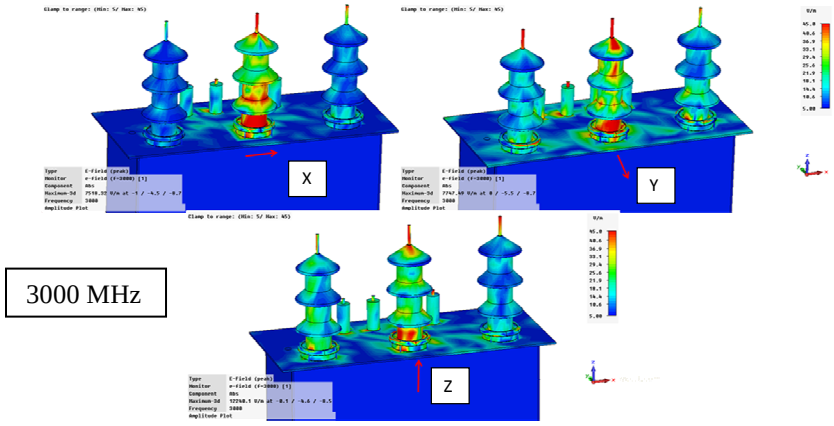

FIGURE 2.45 Simulated irradiation pattern inside and outside the three phase transformer @ 3000 MHz depending on source orientation.

Figures 2.46, 2.47 and 2.48 show the simulation results of the effect of the position of the monopole on irradiation pattern. In particular the monopole was placed below one bushing in three different positions: just below the bushing, in the middle of the tank and near the tank bottom, always with the same orientation along *x* axis.

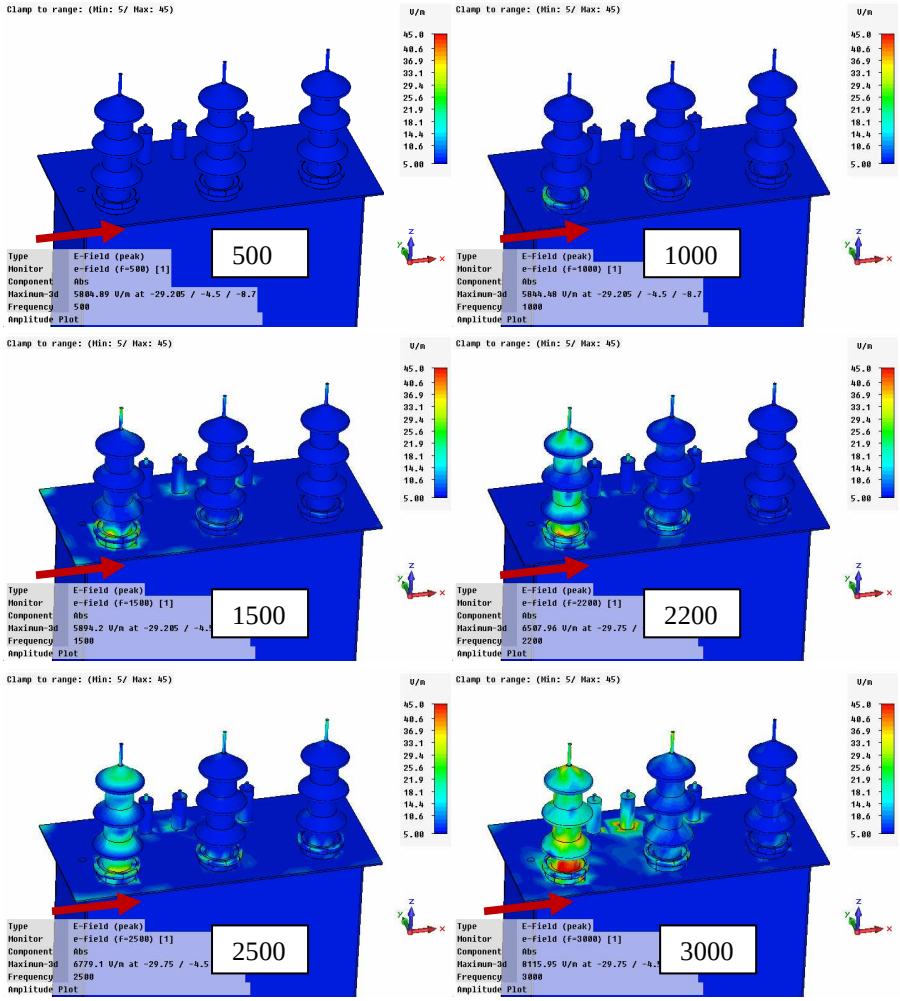

FIGURE 2.46 Simulated irradiation pattern inside and outside the three phase transformer at different frequencies when the monopole is placed at the top of the tank.

Figure 2.46 shows results got when the monopole was placed just below the bushing. It can be seen that at 500 MHz the electrical field is not perturbed outside the tank. Variations occur close to the bushing base at 1000 MHz and become maximum at 3000 MHz. Note that the irradiation is significantly attenuated in the second and, most of all, in the third bushing, according to the experimental results collected in Fig. 2.32.

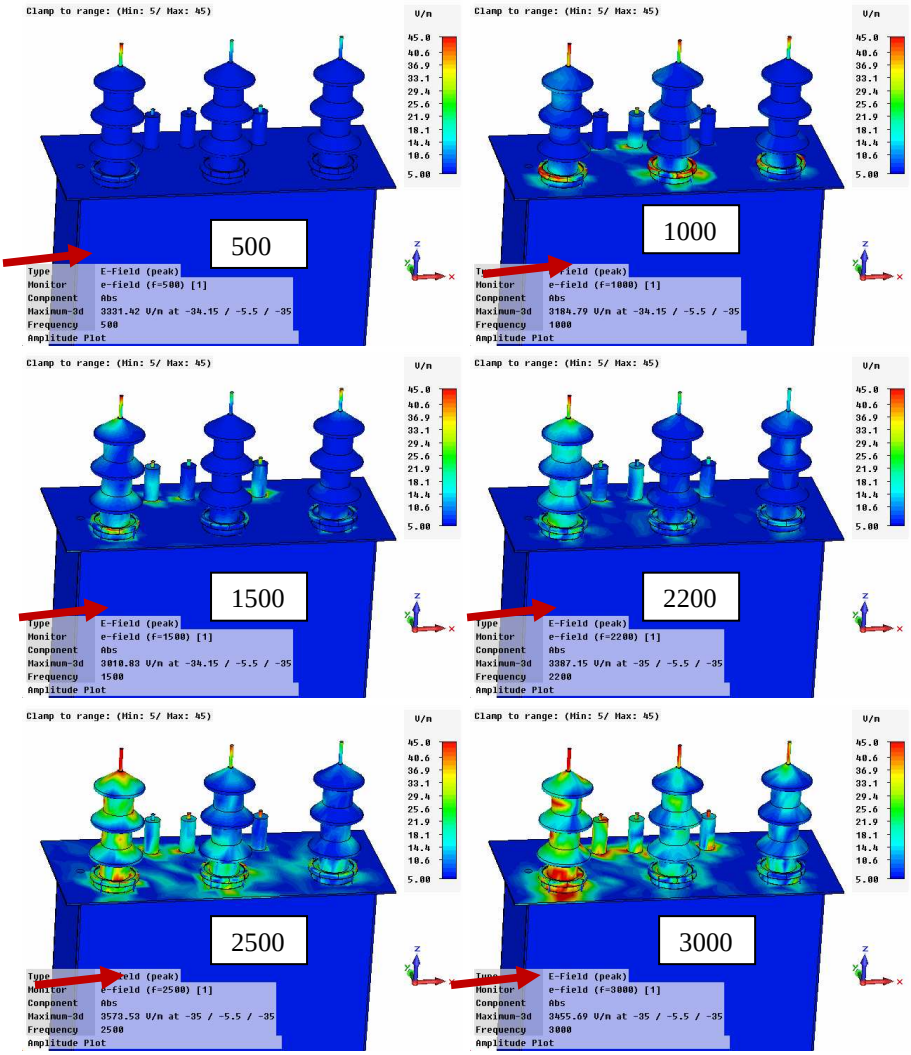

FIGURE 2.47 Simulated irradiation pattern inside and outside the three phase transformer at different frequencies when the monopole is placed in the middle of the tank.

The electric field variation outside the transformer tank, especially close to the bushing aperture, seems to be slightly higher when the monopole is placed in the middle of the tank (Fig. 2.47) than when is placed under the bushing (2.46). Such slight difference could be due to a better coupling between the monopole and the whole winding when it is placed in the middle of the tank.

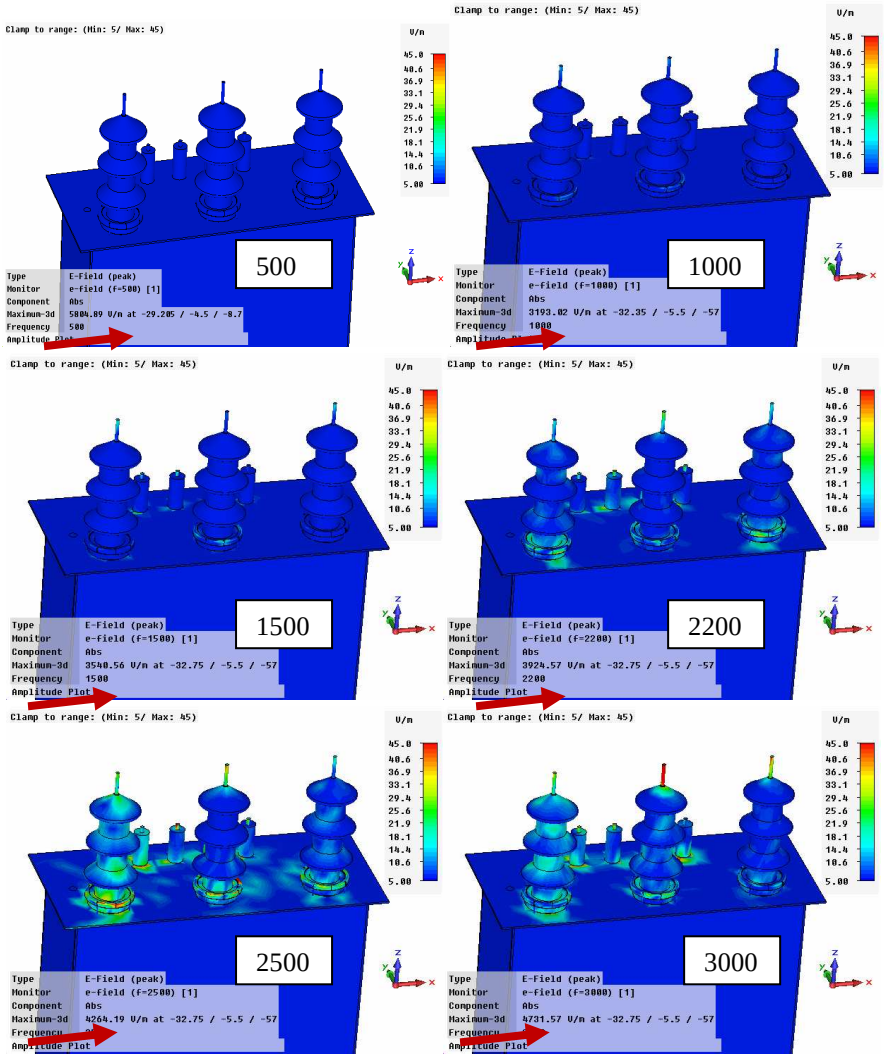

FIGURE 2.48 Simulated irradiation pattern inside and outside the three phase transformer at different frequencies when the monopole is placed at the bottom of the tank.

At last, the electric field distribution outside the tank was investigated placing the monopole under near the bottom of the tank. Simulations results are shown in Fig. 2.48, where, differently from the other two cases, it is possible to see that electric field perturbation occurs at higher frequencies, i.e., starting from 1500 MHz, and that the electric field amplitude is significantly lower within the whole frequency range, due to the combination of several effects which are:

- Higher distance between the source and the bushing, resulting in a lower emission in the low frequency range (<800 MHz).

- Higher distance between the source and the aperture, which means lower excitation of aperture resonances resulting in a lower emission at higher frequencies.
- Shielding effect due to the magnetic core, placed between the source and the apertures.

From the comparison between Figs 2.46-2.48, together with the results shown in Figs. 2.36-2.45, it can be concluded that:

1. Frequencies above 2 GHz have been shown, in general, to be less affected by the effect of monopole position and orientation. This could be due to the predominance, at very high frequencies, of the tank and aperture dimension effect with respect to the magnetic cores and the windings.
2. Sources far from the MV conductors produce significant variations in the external electric field only at high frequency (e.g., >1 GHz), which means that antenna sensors working in VHF bandwidth could not sense such phenomena. Therefore, broadband sensors working in UHF bandwidth could be the optimal ones for carrying out PD measurements on such kind of transformers.
3. Diagnosis based only on PD amplitude could be seriously misled when UHF or VHF sensors are used. As an effect of the attenuation inside the transformer tank and, thus, depending on the position of the source it is possible that the electric field sensed by couplers placed in different position could give results strongly variable in terms of amplitude. It is therefore necessary to identify the PD source and focus the diagnosis mainly on PD amplitude trend evaluation once the PD source is identified.
4. By using three sensors, one at each bushing, it could be possible to attempt a sort of localization of the PD sources comparing the electric field values sensed by each of them. Indeed, it can be seen in the simulation results that the electric field is generally higher in correspondence of the bushing above the source. However, in case of multiple sources this localization procedure can give controversial results. Other techniques working in time domain (Time of Arrival) could be used to achieve accurate results.

Effect of oil losses

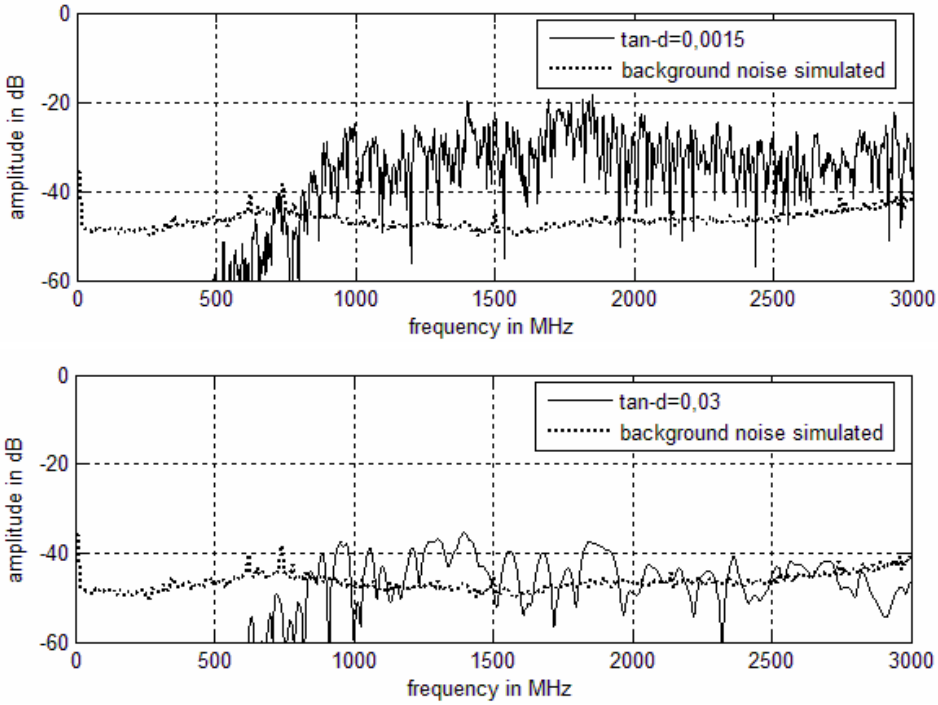

FIGURE 2.49 Simulated irradiation pattern outside the three phase transformer at different frequencies as a function of two different values of oil losses

At last, a simulation was carried out by placing the monopole far from the MV conductors on the top of the transformer and varying the oil losses in order to see the influence of oil tanδ in the EM emission outside the tank. It can be seen that emission decreases with the increase of the tanδ value.

2.5 Design of an UHF coupler for PD acquisition in MV transformers

An UHF coupler was designed to carry out PD detection in MV distribution transformers. Before describing it is important to point out again the difference between detection carried out by sensors placed in far field region (antenna working principle) and in near field region (capacitive coupling principle). Indeed, the resonance frequency of an antenna, or a cutoff frequency of a waveguide, indicate the frequency region where the

system can detect EM irradiation in far field region. Below the antenna resonance, the system can not receive anything in far field region, but it can sense EM field variations if the source is close to the antenna, i.e., within the near- or the reactive- field region. The capability to sense such EM perturbation is given by both the distance between the source and the receiver and the design of the receiver. When detection in near or reactive field region are considered, the term "coupler" instead of "antenna" should be more appropriate, indicating that the capacitive coupling between the source and the sensor predominates on the irradiation.

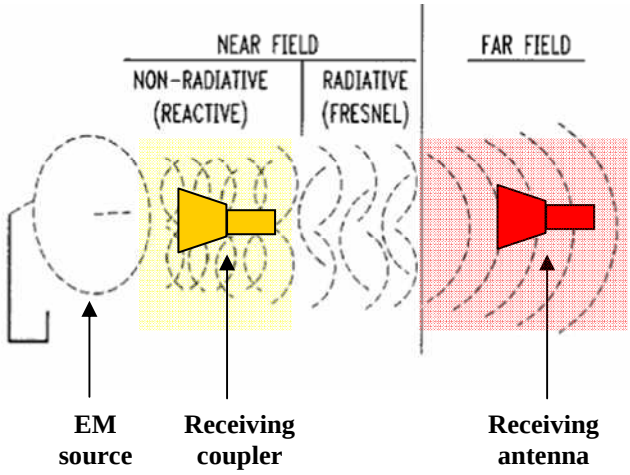

FIGURE 2.50 Sensor position with respect to the source.

In case of PD detection in distribution transformer, it has been shown that significant benefits could be taken considering the use of sensors placed at few centimeters from the bushing base, i.e., in the reactive field region with respect to the circular apertures (modellized as a slot circular antenna), thus improving its coupling capacitive properties.

Let us consider now the specifications and requirements that an UHF coupler should satisfy for PD detection purposes, on the basis of the results and considerations provided in 2.4.

- Broad bandwidth: It has been shown in 2.3 and 2.4 that EM field outside the transformer apertures can be detected within a broad band frequency range. In particular, it has been shown that EM fields can be detected with maximum amplitude above 2 GHz, referring to the worst case seen in Fig. 2.48 where the source is located at the bottom of the transformer, below the magnetic core. Therefore, sensors with good coupling above 2

GHz should be considered, but also coupling at lower frequency is to be taken into account in order to not loose EM field variation at low frequencies when the source is close to the MV conductors.

- Good SNR, i.e. immunity to external disturbances: MV transformers are usually placed near other electrical apparatuses which can give rise to electrical disturbances. A sensors with a reasonably good shielding should be therefore designed in order to be immune to the external disturbances as much as possible.
- Small sizes: In the view of on-field applications, sensors should be small enough to be portable and to fit as best as possible the transformer apertures.

2.5.1. Description of the antenna sensor

The final UHF coupler designed according to the specifications above mentioned is shown in Figs. 2.51 and 2.52. The final design and geometrical properties, shown in the following, were chosen after an optimization procedure which will be shown in the forthcoming paragraphs.

It consists of:

- a length of rectangular waveguide (WR 430 type), 109 mm wide, 55 mm high and 45 mm deep, short circuited at the feeder side;
- an N-type connector place in the central point of the wall at the waveguide short circuited end;
- two copper exponential pitchers placed inside the waveguide: one pitcher is connected between the central conductor of the N connector and the upper edge of the waveguide at the open end; the second pitcher is connected between the N connector ground to the lower edge of the waveguide at the open end;
- one lens of resin, 109 mm wide, 55 mm high and 10 mm deep, placed at the waveguide open end.

The UHF coupler, referred in the following as *horn UHF coupler*, was conceived as a customization of the conventional waveguide WR 430, which has a frequency bandwidth between 1.7 and 2.5 GHz. In particular a section of WR 430 waveguide, 7.5 cm deep, was considered as starting point to design the customized sensor.

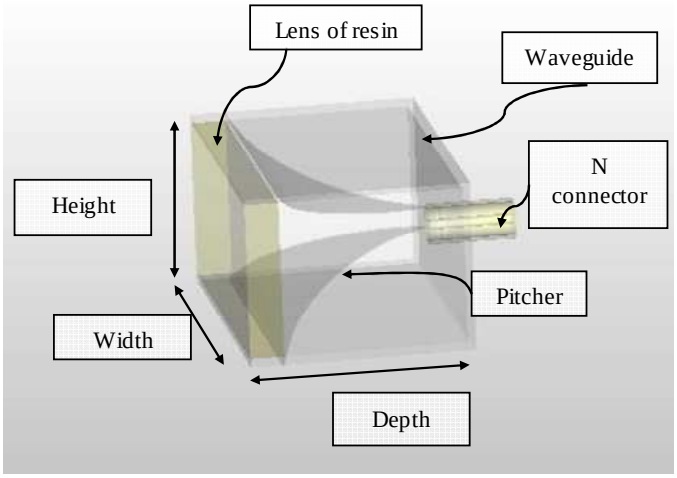

FIGURE 2.51 Sketch of the UHF coupler designed for PD detection pruposes in distribution transformer.

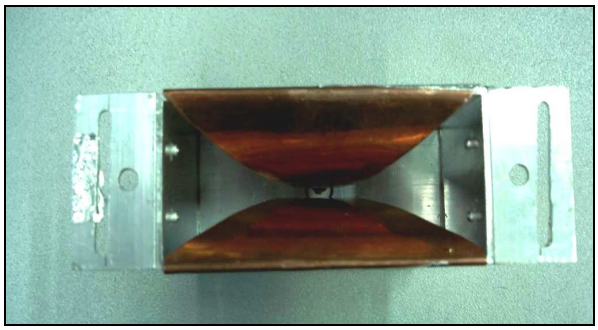

FIGURE 2.52 Picture of the UHF coupler before covering its front with the lens of resin.

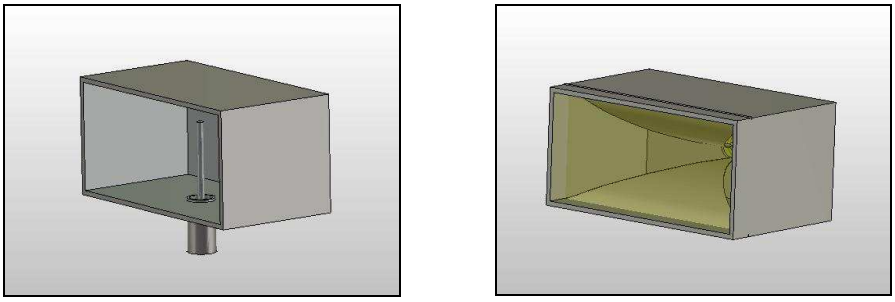

FIGURE 2.53 Sketch of a section of a standard WR 430 waveguide monopole-fed (left) and the final UHF “horn” coupler (right).

Indeed, both the dimension and the frequency bandwidth of such a waveguide were considered suitable for PD detection according to the recommendation listed above, except for the coupling at low frequencies which is negligible for this kind of waveguide Furthermore, waveguides are shielded systems, therefore having optimum SNR within their frequency ranges.

The WR430, used in general as a feeder for horn antennae, is shown in Fig. 2.53 (left) in its classical configuration with a feeding monopole placed at $\lambda/4$ from the back wall, where λ is the wavelength relevant to the cutoff frequency of the waveguide. Commercial WR430 have their first resonance, relevant to the TE10 fundamental mode, at 1.7 GHz and they do not allow propagation of EM waves at lower frequency.

In order to improve the coupling at low frequencies, it was chosen to modify the internal design of the antenna both to shift down the resonance frequency and to increase the capacitive coupling above 500 MHz. At first, the feeding point was moved from the lateral to the back side creating a loop lying in a plane which is parallel to the electric field components [70], as shown in Fig. 2.54 (b). No differences in terms of excitation of the TE10 mode exist between the two feeding choices. Then, the loop was replaced with a copper plate with an exponential profile (Fig. 2.54a). In addition, a mirror cooper plate with the same exponential profile was connected to the Type N connector ground and the upper part of the waveguide aperture (Fig. 2.54b).

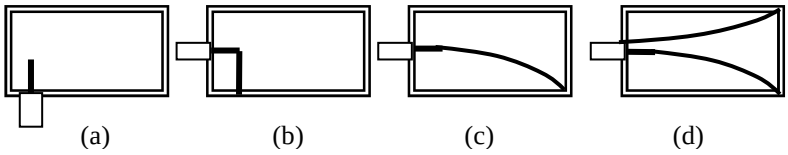

FIGURE 2.54 Different feeding options. Conventional TE10 excitation by electric monopole (a) and loop (b). Variation replacing the loop with a copper plate with exponential profile (c). Introduction of mirror plate with exponential profile connected to N-connector ground to emulate double TEM horn antenna.

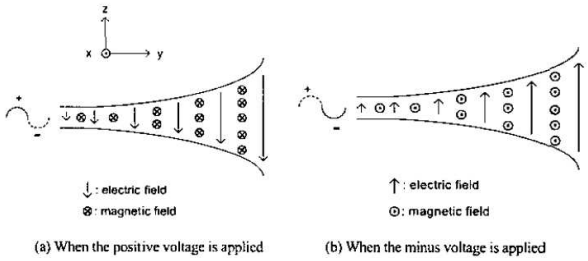

FIGURE 2.55 Principle of TEM generation for a horn structure connected to a coaxial line.

The aim of this modification was to keep the TE10 resonant frequency close to the original (indeed, the metallic plate connected at the end of the waveguide still constitutes a loop parallell to the TE10 electric field lines within the waveguide) and, at the same time, to improve the bandwidth of the coupler at low frequency. As a matter of fact two exponentially tapered plates, separated and then fed by a coaxial line allow TEM mode propagation. Indeed, current flowing through the coaxial lines is converted to waves due to the impedance mismatching between the coaxial connector and the two metallic pitchers at the feed point [70]. The waves which pass through the electric and magnetic fields, generated by the voltage difference between the two plates and by the current flowing through the plates, respectively, may form TEM modes, as sketched in Fig. 2.55. With such an innovative modification of the WR 430 it is therefore possible to increase considerably the bandwidth at lower frequencies allowing TEM modes to be propagated and letting the waveguide working as an antenna above its TE10 mode. At last, a lens of resin 10 mm deep was used to covering the WG aperture in order to shift down the TE10 resonance mode.

To describe the behavior of the UHF horn sensor two measurements were carried out both in far and near field.

Far-field properties

Both the conventional WG430 and the horn UHF coupler were tested and compared in far-field region, i.e. at a distance of 3 m from an emitting antenna source. A broadband elliptic antenna was used as a source when circular polarization was investigated, while a log-periodic antenna was used for investigating the linear polarization. Irradiation results are shown in Fig. 2.58 where it is easy to observe that the horn UHF coupler can detect EM

waves both in the WG430 bandwidth and in a lower frequency range. In particular good sensitivity was found above 500 MHz.

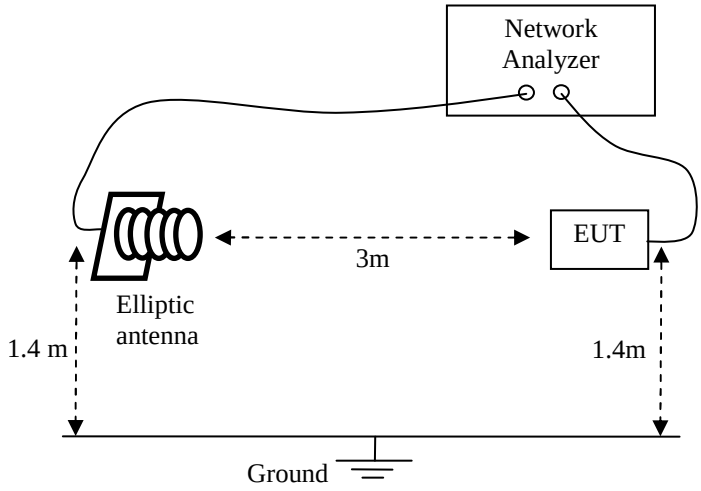

FIGURE 2.56 Far-field measurement setup in circular polarization. The equipment under test (EUT) was placed 3 m far from an elliptic antenna. Both the emitting and the receiving antennae were connected to a Netweork Analyzer.

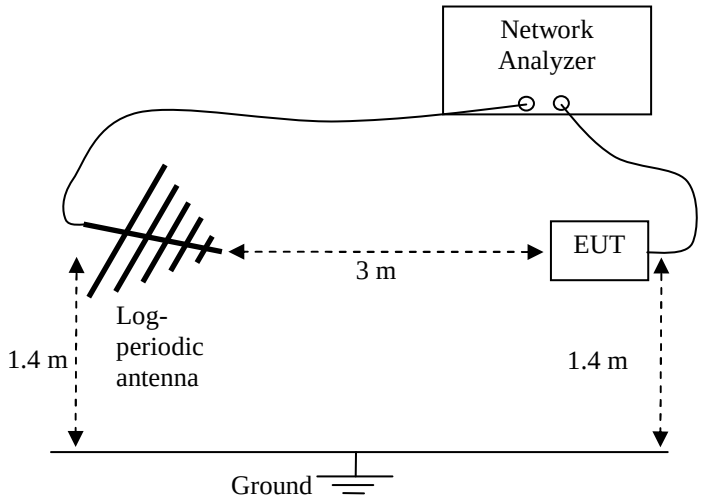

FIGURE 2.57 Far-field measurement setup in linear polarization. The equipment under test (EUT) was placed 3 m far from a log-periodic antenna. Both the emitting and the receiving antennae were connected to a Network Analyzer.

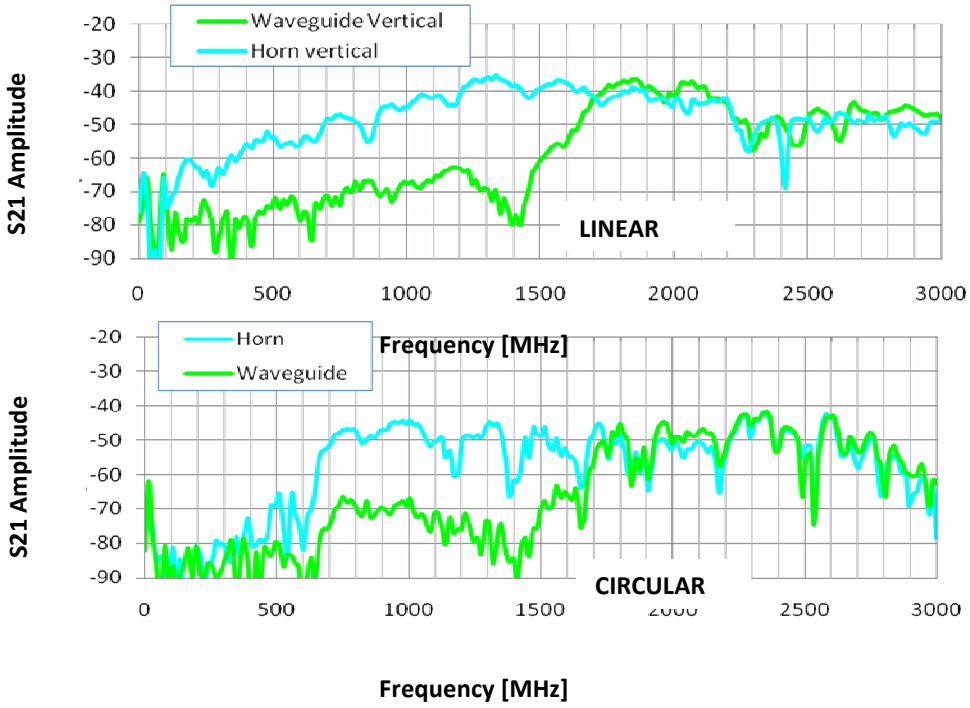

FIGURE 2.58 Far-field measurement in linear and circular polarization. The WG430 can detect irradiation significantly only above its TE10 cutoff (1.7 GHz), while the horn coupler can detect irradiation even at lower frequencies.

Furthermore, the S11 parameter, relevant to the horn UHF coupler, both simulated and measured, is reported in Fig. 2.59. Beyond the excellent agreement between the measured and simulated results, it is important to note that it has been possible to obtain a resonant frequency lower than that of the WR430, without changing the size of the cross section. Such a result was obtained introducing the lens of resin, as it will be shown in 2.5.2.

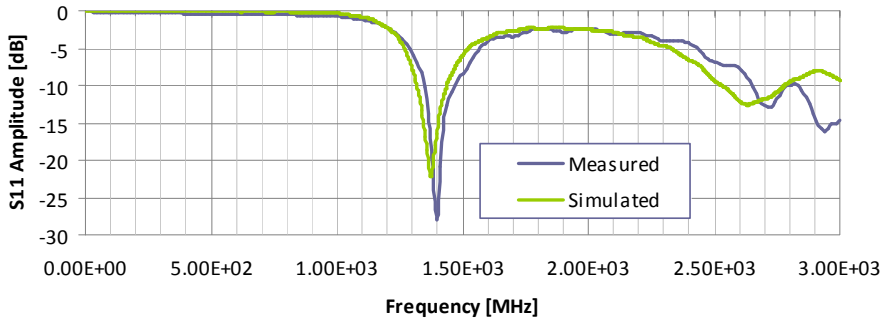

FIGURE 2.59 Comparison between measurement and simulation of the S11 horn coupler parameter. Resonant frequency has been moved from 1.7 GHz (WR430 characteristic TE10 resonance) to 1.5 GHz.

Near-field properties

Near field properties were investigated by using two identical horn couplers and placing them at a distance of 10 cm. Both couplers were then connected to the two ports of the Network Analyzer, as portrayed in Fig. 2.60.

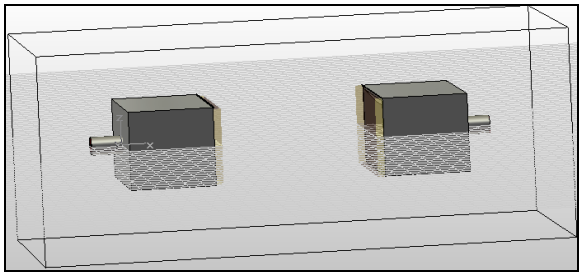

FIGURE 2.60 Near-field measurement setup simulated through CAD software. The two couplers are positioned at 10 cm of distance and connected to the two ports of the Network analyzer.

Insertion loss (S21) parameter was then measured and simulated. Figure 2.61 shows the results of the measured S21 compared to that simulated. It is possible to observe, beyond the good fitting between simulation and experimental results, that the sensor works with good capacitive coupling between 500 and 1.4 GHz. This is an excellent results because it allows to detect the EM field variation outside the transformer tank when the source is located close to the MV conductors, as seen in paragraph 2.4.

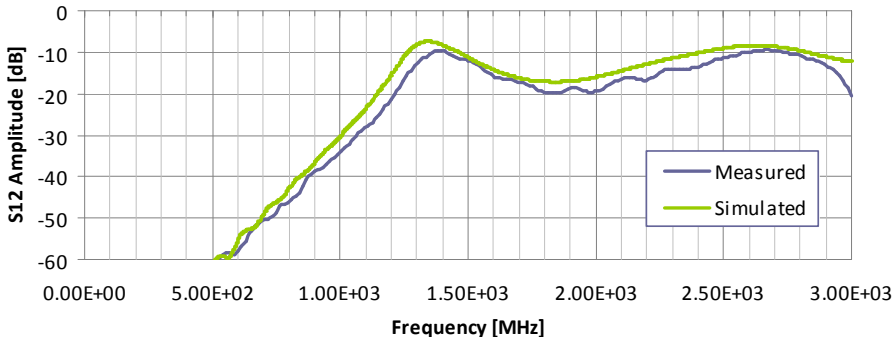

FIGURE 2.61 Comparison between measurement and simulation of the S12 horn coupler parameter. The sensor has very good capacitive coupling between 500 and 1.4 GHz.

2.5.2. Optimization procedures

The actual characteristics of the optimized horn UHF coupler have been shown in the previous paragraph. Anyway, optimization procedures have been carried out both through simulation and experiments in order to obtain the final version of the sensor. In particular, the effect on the S11 and S21 parameters were investigated during the project varying design characteristics before finding out the best features and then release the final version described in 2.5.1.

All the simulation relevant to the S21 parameter were carried out by placing two identical equipment under test at a distance of 10 cm, as sketched in Fig. 2.60.

Waveguide depth effect

At first, the effect of waveguide depth was investigated through simulations. Four different lengths were chosen: 25, 35, 55, and 75 mm. In particular, the latter was the one relevant to the first prototype (still without resin). The simulation results in term of S11 and S21 are shown in Fig 2.63.

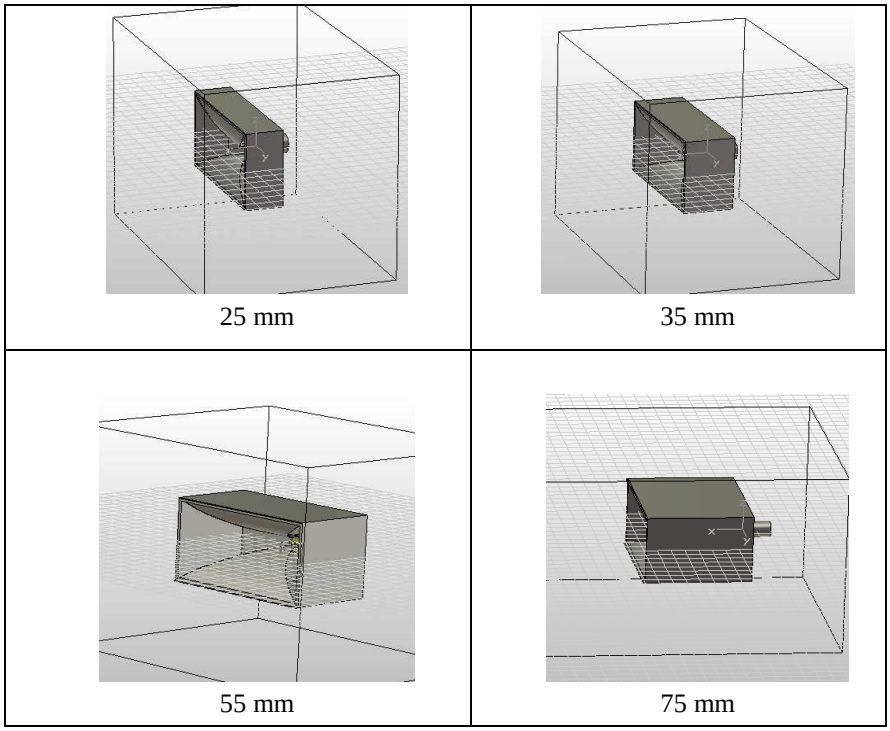

FIGURE 2.62 Simulation of different waveguide depth, without resin.

A low return losses (S11) value is generally desired since it means good impedance matching between the feeder line and the reactive element, that is to say that all the power is transmitted without reflections. However a minimum value is generally accepted, which is -10 dB, above that the antenna is considered not properly matched. It can be seen in Fig. 2.63 that in all cases the peak of the S11 parameter is equal or below -10 dB indicating good impedance matching independently on the four depth values investigated. It can be seen that the first prototype (75 mm) had a low resonant frequency, corresponding to the project requirements. However, both S11 and S21 parameters were the worst if compared to the other depths. In addition, S21 parameter had evident deficiencies above 2 GHz. A good compromise was therefore found out in the waveguide 55 mm deep, which had the same resonant frequency of the WR430 (1.7 GHz) but higher coupling at frequencies above 500 MHz.

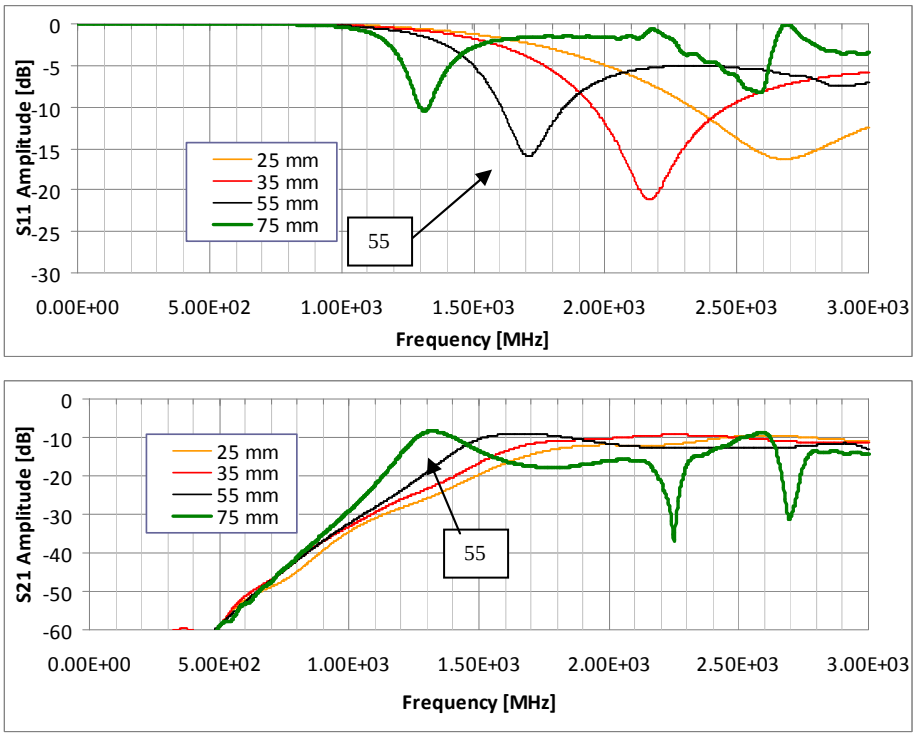

FIGURE 2.63 Simulation of S11 and S21 parameters for different waveguide depth, without resin.

Pitcher's profile effect

Before choosing the exponential profile, other different solutions were investigated for the two pitchers inside the waveguide. In particular, a simulation was carried out with four profiles defined in the following as exponential, abrupt curve, flat and inverse exponential, referring to Fig. 2.64. Simulation was carried out on two identical sensors 55 mm deep and without any resin inside.

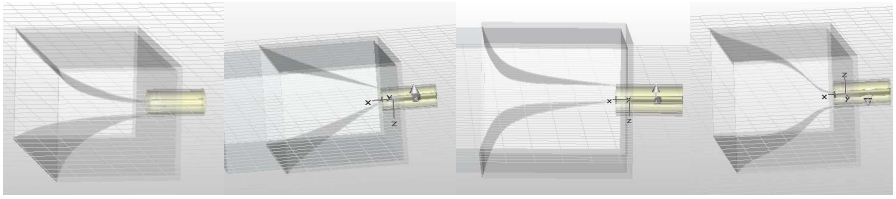

FIGURE 2.64 Different pitcher's profiles investigated through simulation.

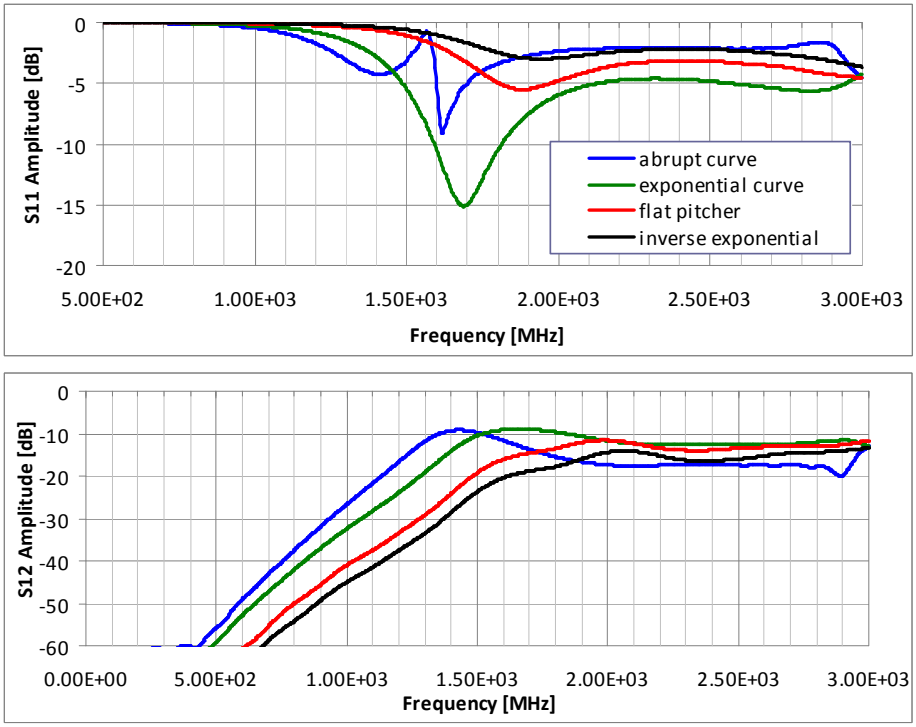

FIGURE 2.65 Simulation of S11 and S21 parameters for different pitcher profiles, without resin.

From the simulations, whose results are shown in Fig. 2.65, it comes out that the abrupt curve and exponential profiles presented best S21 parameter, being the transmission S21 peak at lower frequency than the others and being the capacitive coupling at low frequencies definitely higher. From S11 parameter it can be seen that the exponential profile is definitely better than the abrupt curve, being the latter characterized by a very poor S11. It was therefore chosen the exponential profile.

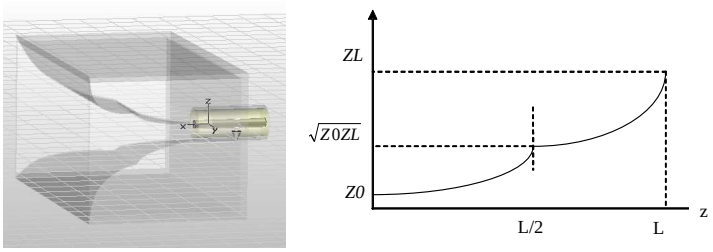

FIGURE 2.66 Klopfenstein profile design.

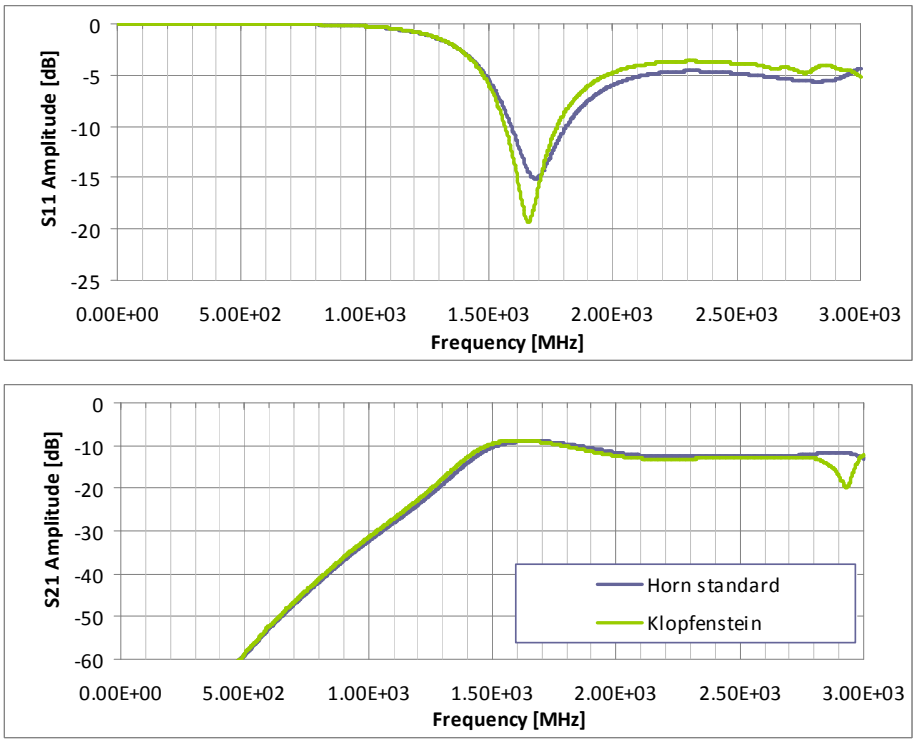

FIGURE 2.67 Comparison between S parameters simulated using an exponential and Klopfenstein profile.

A further simulation was then carried out comparing the exponential with the Klopfenstein profile. Such a profile allows better matching between coaxial impedance Z0 (50 ohm) and load impedance, i.e., the characteristic impedance at the waveguide aperture (377 Ohm). It can be seen in Fig. 2.67 that actually the Klopfenstein profile improves a little the S11 parameter (from -15 to -20 dB) but such an improvement is definitely too small to justify the introduction in the antenna design of a so complex geometry.

Filling material effect

At last, once the waveguide depth and pitcher profile were optimized, the effect of the introduction of a resin material was investigated.

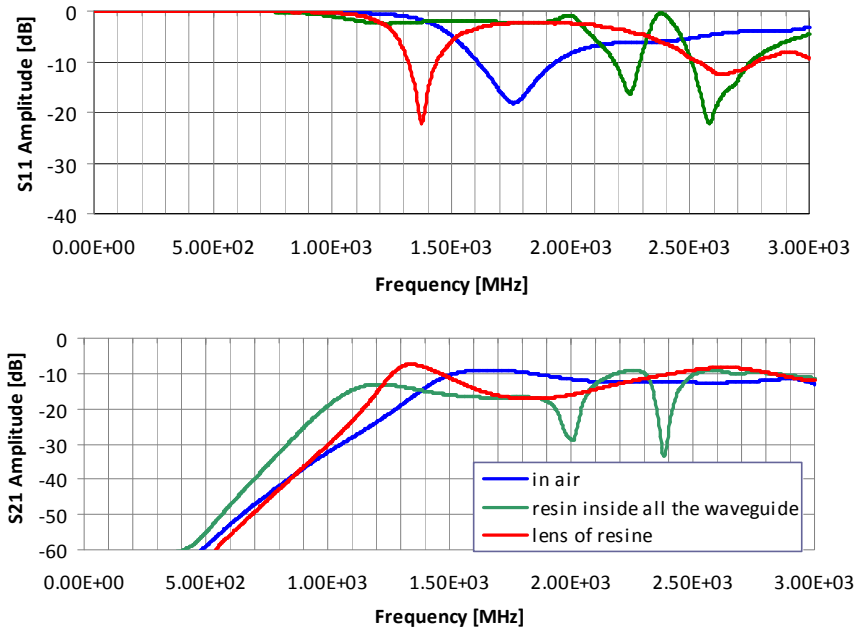

FIGURE 2.68 Comparison between S parameters simulated for different filling.

In particular two solutions were taken into account: filling entirely the sensor with epoxy resin or just covering the waveguide aperture with a lens of resin. Figure 2.68 shows the results obtained from the simulation between the horn sensor without resin, the horn sensor with 1 cm of resin at waveguide aperture and the horn sensor completely filled with resin.

It can be observed that, in terms of S11, better matching can be obtained with the lens of resin. Furthermore, the resonant frequency can still be shifted down from 1.7 GHz to less than 1.4 GHz. In terms of S21, higher coupling at low frequencies is given by the complete filling of the sensor

with resin, but S11 relevant to the sensor filled with resin is definitely poor around 2.3 GHz.

The best compromise in terms of S11 and S21 can be thus achieved by introducing only a 10 mm layer of resin just at the waveguide aperture.

2.6 Partial Discharge measurement on a three-phase MV transformer

A real application of the study carried out in the previous paragraphs is here shown through the detection, in factory, of PD phenomena inside a two 1000 kVA, 15000/400 V, three phase transformers.

During both measurements four sensors were used:

1. HFCT around the transformer ground connection. This setup is generally not used on-field due to presence of several grounding connection between the transformer and the main earth, which results in a strong attenuation of the signal. On the contrary, in factory it is possible to let the transformer grounded only through one earth connection, thus allowing PD detection using an inductive HFCT clamped around that ground lead.

2. TEV Jumper at transformer top cover. Such sensor is a capacitive probe able to sense the current pulses traveling on the outer box surface. Indeed, when PD occur inside the tank, transient currents can be induced in the inner tank surface. Owing to apertures in the box, such pulses can also propagate along the outer surface, and be detected through capacitive probes. It has been placed close to the bushing as shown in Figure 2.68 (a).

3. Inductive sensor: A magnetic sensor constituted of 5 turns around a ferrite core was placed close to the base of the bushing as shown in Fig. 2.68 (b). Its bandwidth lies in the VHF range.

4. HORN coupler: It was placed close to the base of the bushing as shown in Fig. 2.68 (c).

Two different PD activities were detected in the two transformers under test. The relevant Phase Resolved Partial Discharge (PRPD) patterns detected through the HFCT connected to a commercial PD detection instrument, having a bandwidth in the [0.016-35] MHz range, are collected in Fig. 2.70.

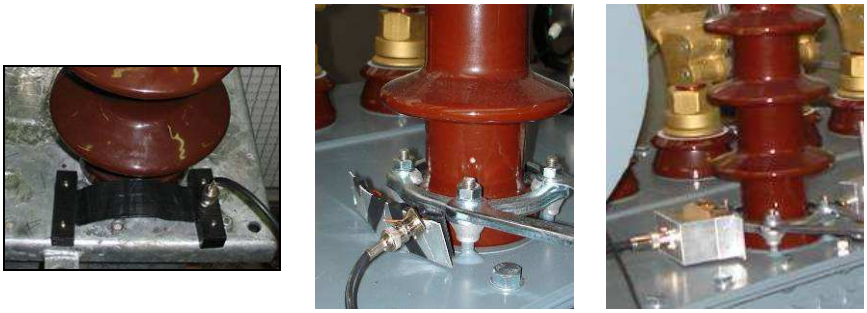

TEV Jumper (a) Inductive strip sensor (b) HORN coupler (c)

FIGURE 2.69 Installation of different sensors close to the transformer bushings.

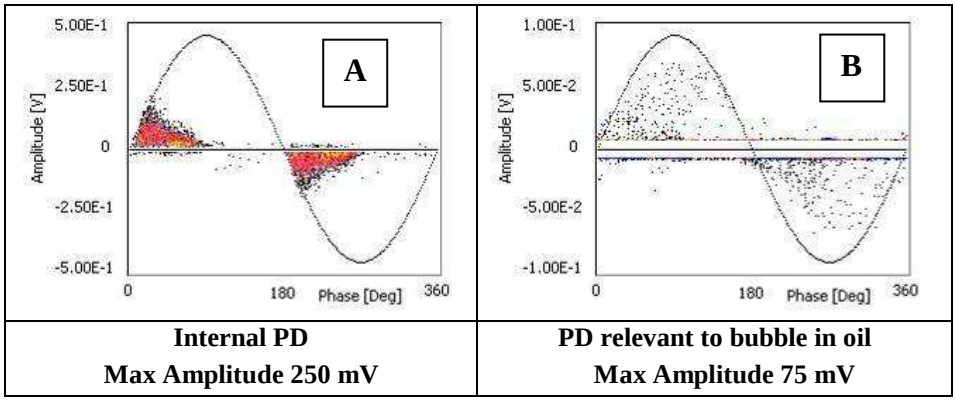

Internal PD **Max Amplitude 250 mV**	**PD relevant to bubble in oil** **Max Amplitude 75 mV**

FIGURE 2.70 PRPD pattern relevant PD activities originated from an internal defect (A) and bubbles in the oil (B), detected through the HFCT sensor clamped around the ground connection of the transformer under test.

The other three sensors were then connected to the 3 GHz Spectrum Analyzer using a 3 MHz resolution bandwidth. Results from this first measurement are collected in Fig. 2.71, where it can be seen that:

- the maximum spectrum in terms of bandwidth and amplitude was detected by the horn coupler, especially above 800 MHz, according to the results obtained from the simulations.

- The TEV jumper sensor was able to detect EM emission in a broad band frequency range as well, due to the capacitive coupling with the aperture in the reactive field region.
- The inductive strip was able to detect only frequencies below 1500 MHz, but with significantly lower amplitude than the horn.

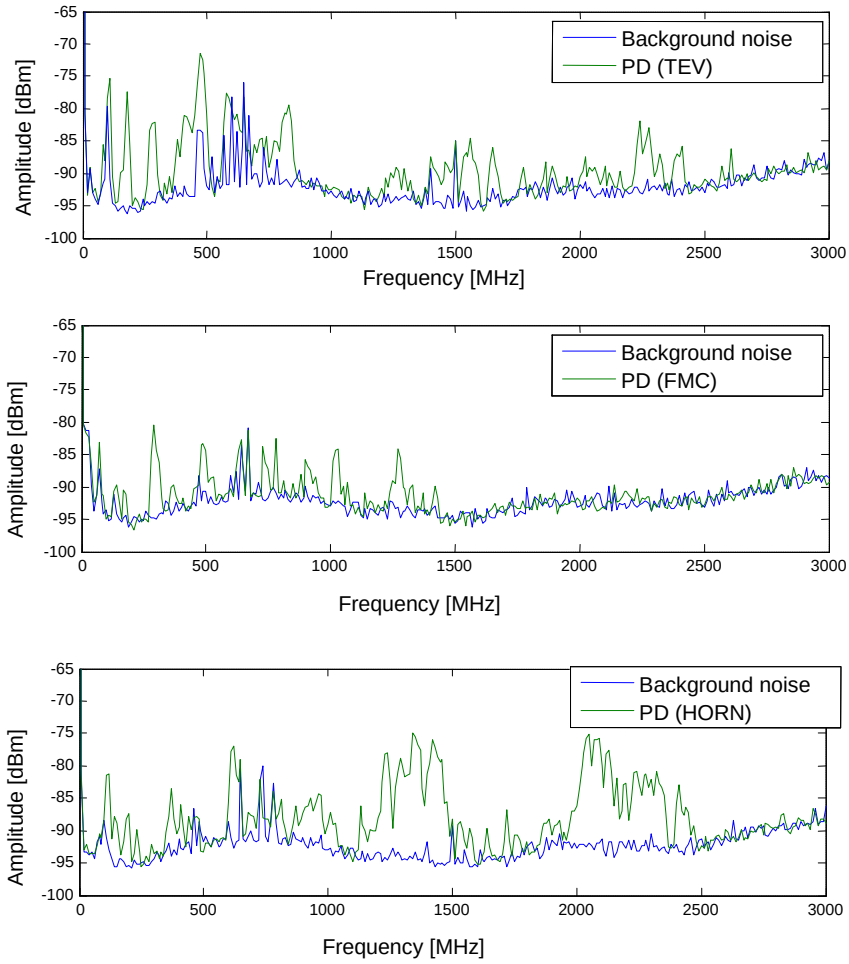

FIGURE 2.71 Spectra relevant to PD activity (A), detected through different sensors. Maximum amplitude was detected when Horn Coupler was used.

PD activity B, likely due to bubble in oils, was detected through the HFCT with significantly lower amplitude (75 mV) than PD activity A (max amplitude 250 mV), which was likely due to an internal PD within the paper layers. During the first measurement through the Spectrum Analyzer no emission was sensed by the TEV Jumper and the inductive strip at PD

inception. Only using the horn coupler it was possible to detect something with quite small amplitude between 800 and 1500 MHz, as can be seen in Fig. 2.72.

Therefore, a 20 dB broad band amplifier was connected between the sensors and the Spectrum Analyzer.

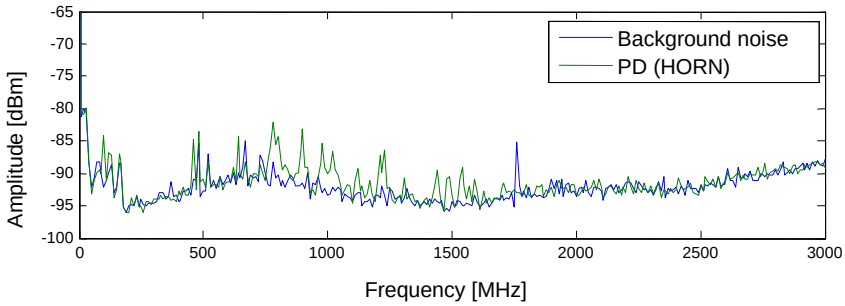

FIGURE 2.72 Spectrum relevant to PD activity (B), detected through Horn Coupler. EM emitted outside the transformer apertures is very low due to the weak PD activity.

It can be observed in Fig. 2.73 that using the amplifier it was possible to detect a slight emission also with the TEV and the inductive strip. Anyway, it can be seen that the spectrum detected by the horn coupler connected to the amplifier is comparable to the other sensors in the low frequency range (<800 MHz), while it is significantly higher in the high frequency range, i.e., where the S21 of the sensor presents a flat behavior.

It is thus reasonable to think that PD activity B is originated from a source far from the MV connection, so that the coupling between the source and the MV bushing is weak and only the high frequencies, associated to the higher modes of the cavity, can be irradiated outside the tank, according to the simulation results in 2.4. On the other hand, the PD source relevant to PD activity A was better coupled with the MV conductors, resulting in a perturbation of the EM field outside the aperture at low frequencies detectable even without any amplifier.

However, it is clear that horn coupler present good coupling with the source and with the transformer apertures in both cases, thus allowing PD detection with very good SNR over a wide frequency range.

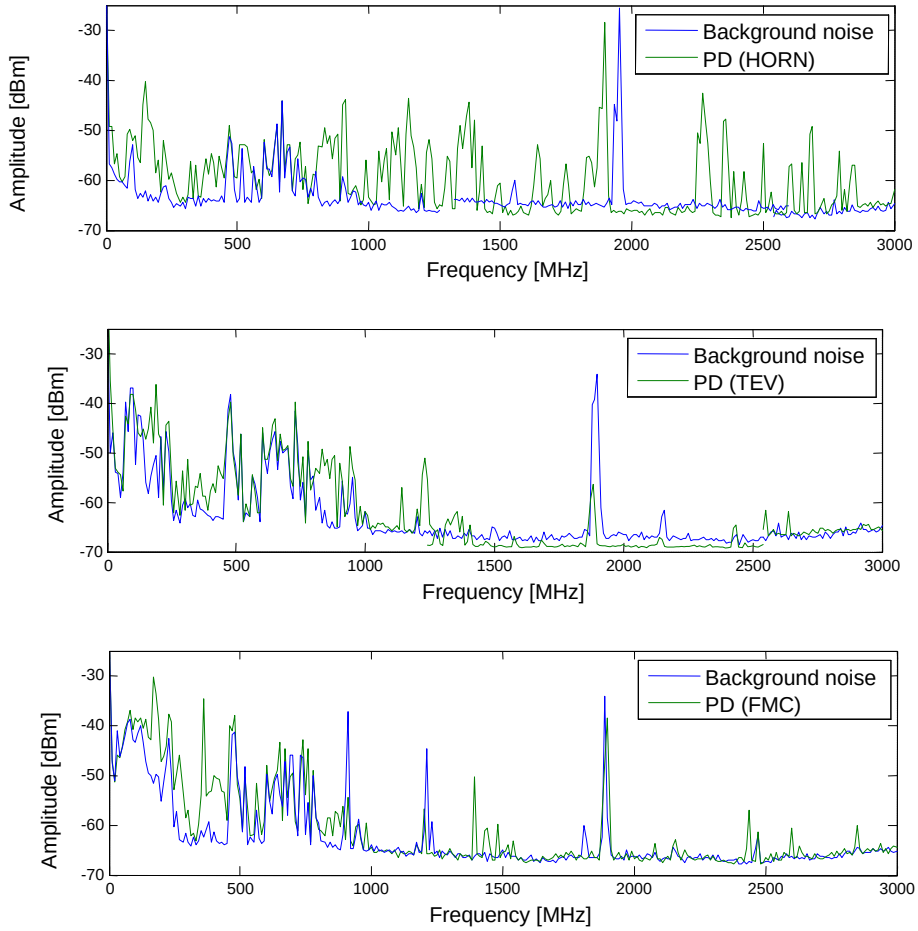

FIGURE 2.73 Spectra relevant to PD activity (B), detected through different sensors. A 20 dB amplifier was connected between sensors and the Spectrum Analyzer. Maximum amplitude was detected when Horn Coupler was used.

Chapter 3

PD propagation and detection in Medium Voltage switchgears

3.1 Premise

Partial discharges are involved (as a symptom or as a cause) in 85% of medium voltage (MV) switchgears faults [71, 72]. Thus, PD detection is a key technique to prevent switchgear dielectric failures. As an example, when surface PD are observed, cleaning or replacement of terminations can prevent flashovers. However, it must be stressed that not all defects in MV switchgears are equally harmful and, therefore, not all PD activities deserve the same level of attention. As a matter of fact, corona PD (that is, discharges in free air volume due to metallic protrusions on conductors) produce ozone, which can attack chemically polymeric insulation systems used in MV cables. The degradation rate, however, is not very large, as ozone is spread in the surrounding environment. On the contrary, as mentioned above, PD on MV cable terminations produce tracking, leading in relatively short time to flashover. PD that are internal to cables, potential or current transformers insulation systems (due to cavities, protrusions, contaminants, etc.) or in the bus spacers are characterized by yet larger degradation rates.

According to the above considerations, characterizing PD within switchgears through magnitude or repetition rate alone is not the most effective way to carry out proper Condition Based Maintenance (CBM)

operations. Indeed, performing maintenance when not needed (in the presence of corona PD alone, for instance) means incurring in extra costs while, possibly, other more harmful sources go unchecked (due to, e.g., personnel limitations) leading to faults. In the current scenario of severe industrial competition, sustaining such costs is no longer affordable, so that more effective solutions need to be devised. The only way to maximize the economic performance of CBM practices on switchgears resorts to a correct identification of PD sources. As a matter of fact, if PD sources are correctly identified, ranking the harmfulness of the defect in the various apparatus becomes possible, leading to an effective schedule of human and economic resources.

The following paragraphs will discuss the bandwidth of irradiated phenomena associated to PD activities inside switchgears, in order to design appropriate detecting sensors.

3.2 Overview on existing PD detection methods

3.2.1 PD detection from HFCT sensors installed inside the switchgear

Providing MV switchgears with HFCT sensors permanently installed around the cables ground lead connections can represent a good solution to assess both the cable and the switchgear condition.

FIGURE 3.1 HFCT sensors installed inside the switchgear, around the cables ground lead.

Indeed, irradiation phenomena, associated to the PD activity within the switchgear, or capacitive coupling, between the PD source and the cables conductors, can lead PD pulses, originated inside the cabinet, to propagate

along the MV cables and, thus, to be detected by the HFCT inductive sensors. However, it must be considered that spare panels are also present in MV substations, which are connected to the same MV bus-bar of the other cabinets, but they are not provided with any MV cable. It is, therefore, not possible to install HFCT sensors in such panels and, therefore, monitor their conditions.

3.2.2 PD detection from capacitive couplers installed inside the switchgear

In some cases, switchgear manufacturers (especially those involved in gas insulated 33 kV switchgears design) can provide the cabinets with voltage probes embedded in the bushings connected to the MV bus-bars. On-field measurements have demonstrated that such low voltage probes can be effective for PD detection, if proper designed resistive quadrupole are connected between the voltage probe and the PD acquisition unit. In this case, the sensitivity inside the switchgear can increase outstandingly, allowing PD detection to be carried out successfully in spare panels too.

When the switchgears are not endowed with the above mentioned probes, it is possible to permanently install capacitive couplers to the MV bus-bars inside the cabinets. However this solution has to be mutually agreed with the switchgear manufacturer. This procedure can take long time and it is approved, in general, with difficulty since the introduction of couplers (which can also be manufactured by third companies) can represent an extra cost and can affect the whole system reliability if not proper designed and qualified.

3.2.3 PD detection from Transient Earth Voltage capacitive sensors

When PD occur the phase-to-earth insulation, a small quantity of electrical charge is transferred capacitively from the PD source to the earthed metal cladding. Therefore transient pulses can travel along the switchgears earthed panel surface and be detected through proper capacitive sensors attached at the cabinet surface. Such sensors are commonly called Transient Earth Voltage (TEV) probes and have a bandwidth ranging between few kHz to a maximum of 100 MHz.

To explain the working principle of such sensors, let us assume the PD event to be qualitatively modeled as a discharge between two electrodes, separated by a gap of air, connected in parallel to a capacitance Ca, representing the main insulation between MV electrode and the ground, as shown in Fig. 3.2a.

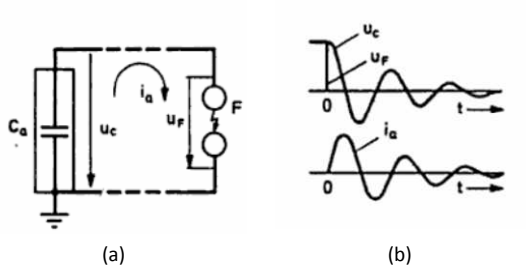

FIGURE 3.2 Qualitatively representation of a discharge, occurring between two electrodes, originating a transient current Ia flowing in the circuit.

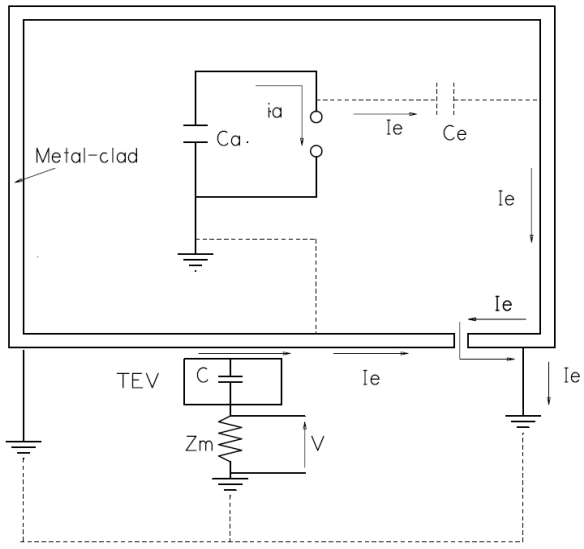

FIGURE 3.3 TEV capacitive coupler working principle. A transient earth induced current, *Ie*, flows along the switchgear metallic surface accordingly to a PD event inside the cabinet, through earth stray capacitances, *Ce*. By using a capacitive probe, C, in series to a measuring impedance, *Zm*, it is possible to record the transient current associated to the PD event.

When the two electrodes are short circuited, consequently to the PD event, a transient current, I_a, will flow along the circuit and a transient voltage, u_c, will appear across C_a [73]. Therefore, as an effect of the stray

earth capacitance *Ce* (Fig. 3.3), a transient current *Ie* will be induced also in the inner surface of the switchgear metal-clad. If there are apertures in the switchgears, transient currents, Ie, can propagate also in the outer surface of the cabinet and it will be, therefore, possible to detect such induced currents through appropriate capacitive probes, *C*, attached to the metal outer surface, as shown in Fig. 3.3. Furthermore, localization could be feasible, by placing several TEV probes on the earthed metal cladding of the switchgear, and using well known algorithm as those based on the Time of Arrival, i.e., based on the comparison of the time of flight of PD pulses detected simultaneously by different sensors placed in different positions.

However, it must be considered that such a detection method could present two criticalities:

1. PD events occurring between two phases could be detected with low sensitivity, since the coupling with the earthed metal-clad can be significantly lower if compared to a phase-to-ground discharge.
2. The outer metallic surface is always covered with a thin layer of insulating painting. The presence of this thin insulating layer can result in a decrease of the global capacitance between the sensor and the metal-clad and, thus, a reduction of sensitivity. Therefore, to increase the effectiveness of such sensors, they should be placed in an unvarnished area of the metal-clad (which is, in general, not feasible).

3.2.4 PD detection through acoustic sensors

Properly designed microphones are largely used for PD detection in MV switchgears [74]. Such sensors have bandwidth lying in a hundred of kHz and are generally mounted on proper holders allowing the sensors to be handled easily and brought close to the apparatuses. It must be stressed that such detectors are suitable for detection and location of PD in air, like surface or corona PD. On the contrary, the sensitivity is very poor for internal PD (e.g., internal cavities inside the bushings or in cable terminations). Furthermore, in air-insulated distribution substations, several corona phenomena can occur simultaneously outside the switchgears and be detected by the same microphone, thus influencing the acquisition and reducing outstandingly the PD localization accuracy.

3.3 Investigation of PD irradiation properties inside and outside switchgears

Irradiation inside and outside Medium Voltage switchgears is investigated in the following paragraph. Indeed, a switchgear can be represented as a resonant cavity excited by an impulsive source, similarly to MV transformers. By using equation (2.3) it is possible to evaluate the internal resonances of the cabinets, associated to TE and TM propagation modes, which can be excited by an internal impulsive PD source.

By placing EM probes or antennas inside the switchgear, it could be, therefore, possible to detect PD activities with advantageous SNR, being the whole cabinet shielded from external disturbances. To design such probes or antennas it is, at first, necessary to workout the resonance frequency of the cabinets in order to match the sensor bandwidth or resonances to those of the cabinet. In order to carry out proper maintenance on switchgears that are already in service and, thus, can not be opened to allow the introduction of internal sensors, it is essential to develop external sensors able to sense either EM irradiation through apertures in the cabinet, or PD current pulses traveling on the metal clad surface, i.e., following the TEV principle. All cases are investigated in the following.

3.3.1 PD detection inside switchgears through internal sensors

Likewise MV transformers, the cabinet resonances can be evaluated resorting to the waveguide theory, being such resonances the same of those relevant to a short-circuited section of rectangular waveguide. Thus, it is possible to evaluate TE and TM propagation modes using equations (2.3), indicating the cutoff frequency of each possible propagation mode.

As an example, the switchgear discussed here is an air-insulated 15 kV cubicle having the following geometrical sizes: height 1.95 m, width 0.56 m, depth 1.15 m. The cubicle is endowed with a front door 1.20 m high, 0.50 m wide, with 0.24 x 0.1 m rectangular inspection window.

Table 3.1 collects the TE and TM propagation modes for the air-insulated switchgear shown in Fig. 3.4. Anyway, the same process can be carried out for air-insulated switchgears having different dimensions or gas-insulated. Therefore, it is possible to design internal sensors for PD detection purposes,

having a frequency bandwidth centered on a frequency equal or higher than the fundamental resonant mode of the cabinet.

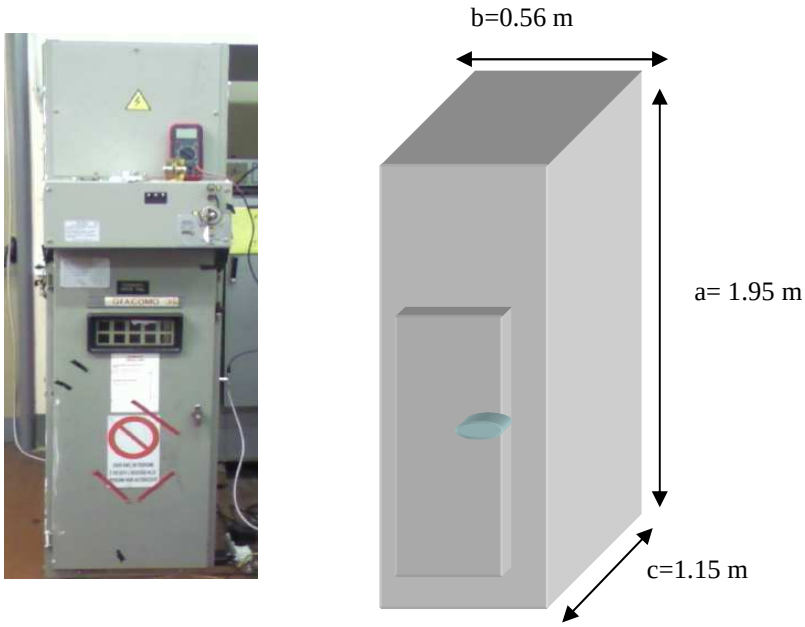

FIGURE 3.4 Medium Voltage 15 kV air-insulated switchgear used for carrying out the investigation on PD propagation properties.

TABLE 3.1 TE and TM Propagation modes cutoff frequencies

m	n	p	TE^{z}_{mnp} Frequency [MHz]	TM^{z}_{mnp} Frequency [MHz]
1	0	1	151.4	/
1	1	0	/	297.92
1	1	1	307.6	307.69
2	0	1	271.9	/
2	0	2	302.8	/
1	2	0	/	551.3
1	1	2	335.3	335.3
1	2	2	572.4	572.4
2	2	1	600.7	600.7

3.3.2 PD detection outside switchgears through external antenna sensors

The irradiation outside the switchgear will be investigated in the following. The cabinets are endowed, in general, with apertures which can let the EM waves to propagate outside the switchgears. Two types of apertures can be basically considered:

a) narrow slots between the cabinets and the door (Fig. 3.5a)
b) narrow slots between the switching module and the cabinet (Fig.3.5b)

Both aperture types can be studied as narrow rectangular slot antennas having resonance frequency f_s equal to

$$f_s = \frac{c}{2L\sqrt{\varepsilon\mu}} \tag{3.1}$$

where c is the speed of light and L is the slot length. Therefore, whenever the PD pulses, occurring inside the switchgear, can excite the resonant frequencies of the slot apertures, EM waves can propagate outside the cabinet and be detected through proper antenna sensors. As an example, for a MV switchgears provided with a front door 1.20 m high and 0.50 m wide, as the one shown in Fig. 3.4, two slots can be considered along the two dimensions, having resonant frequencies at 125 and 300 MHz, respectively, according to (3.1).

The consideration above can be demonstrated through a series of experimental tests carried out through an electrically short monopole connected to a Noise Generator (the same used in Chapter 2) and placed inside the switchgear. In particular, the monopole was placed in correspondence of the center of mass of the switchgear. The EM irradiation outside the cabinet (with the door closed) was captured by means of a log-periodic antenna (30 MHz-3 GHz) connected to the same Spectrum Analyzer used in Chapter 2. The first result, gained from the experimental test, was that the antenna was able to sense EM waves irradiated outside the switchgear, demonstrating that the narrow slots were actually excited by the internal source, letting EM waves propagate outside, as expected. The receiving antenna was placed in several positions with respect to the cabinet door, but always at the same distance from the door (300mm), showing

significant changes in the irradiation pattern in terms of magnitude of the spectral components.

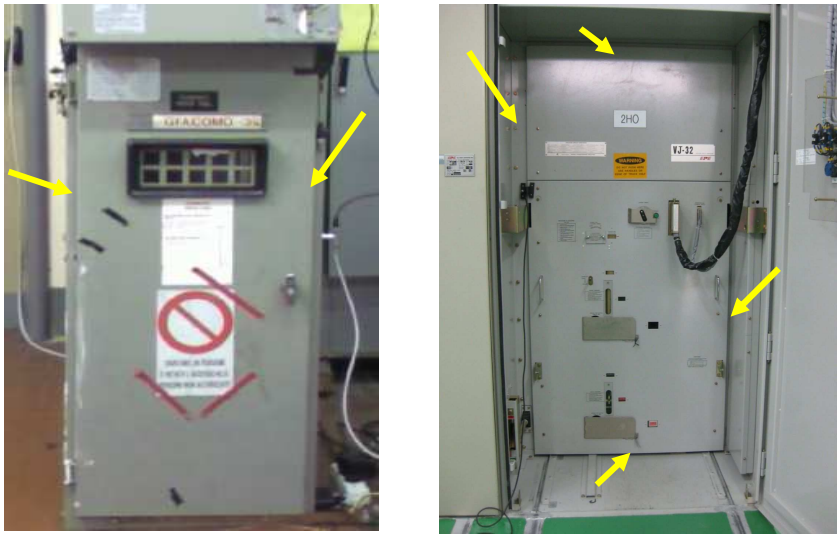

(a) (b)

FIGURE 3.5 Narrow slots in MV switchgears (marked in yellow) which can allow EM irradiation outside the cabinet.

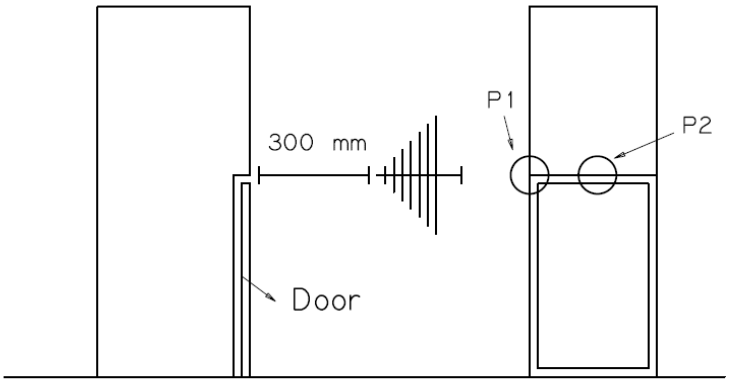

FIGURE 3.6 Drawing indicating the position of the log-periodic antenna during experimental tests. The antenna was placed 300 mm far from the door, oriented to the upper left door's corner (P1) and to the middle point of the upper door's aperture (P2).

As an example, Fig. 3.7 shows two spectra detected by the log-periodic antenna in two different positions (indicated as P1 and P2 in Fig. 3.6, respectively).

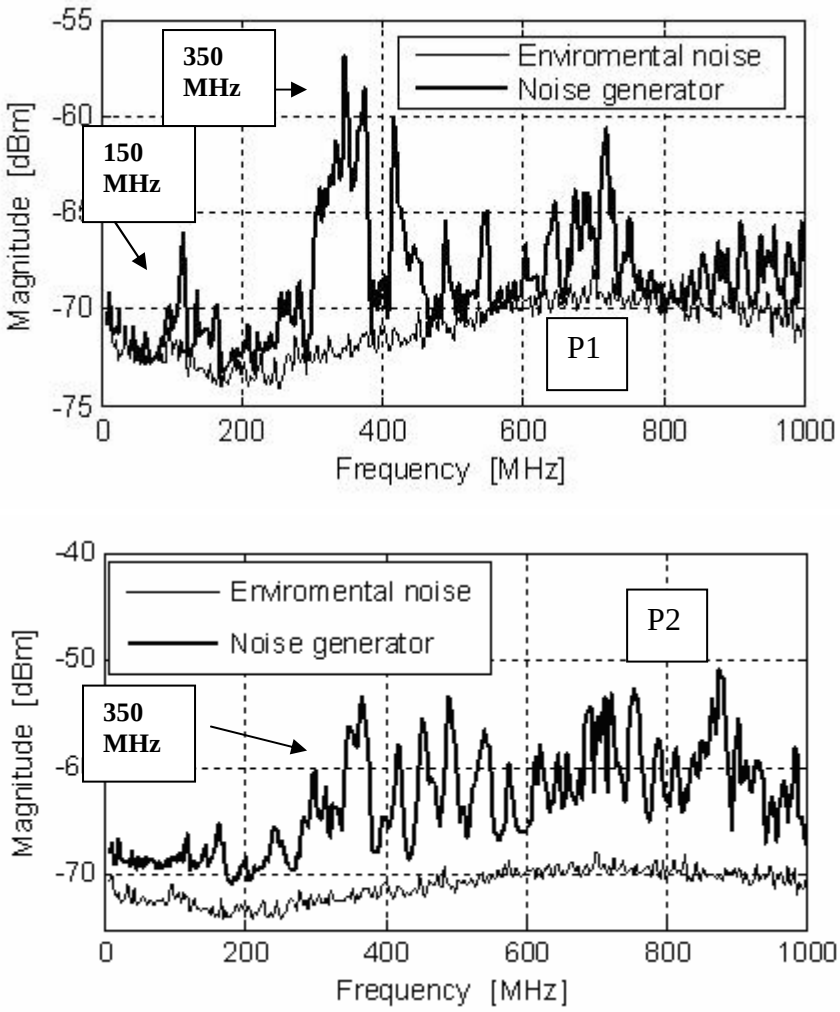

FIGURE 3.7 Irradiated spectra detected during experimental tests using a log-periodic antenna in two different detection points.

Furthermore, it can be noted that when the antenna is placed in front of the door's corner (position P1), significant irradiation starts above 300 MHz and that the highest irradiation occurs around 350 MHz, i.e., approximately around the resonance frequency of the shorter door aperture. However, smaller irradiation can be also noted at lower frequencies, around 150 MHz, i.e., around both the estimated resonance frequency of the longer door aperture and the cabinet fundamental propagation mode. Figure 3.7 shows also that irradiation is very poor at frequencies lower than 300 MHz when the antenna is placed in point P2, i.e. close to only the shorter aperture. Furthermore, irradiation above 300 MHz is almost 10 dBm higher than that measured in point P1.

The experimental test carried out through the log-periodic antenna and the noise generator inside the switchgear was useful to elaborate some simple conclusions of outstanding importance, which are:

- small apertures (few millimeters wide) can allow irradiation outside the switchgear;
- proper antennas can be designed to detect such irradiation;
- the frequency bandwidth of the irradiated spectrum can depend on both the slot dimensions and the cabinet size. Indeed, the cabinet behaves like a resonant cavity, generating EM waves which can propagate outside the cabinet through the apertures. The whole system can, thus, considered as a high pass filter having a lower cutoff-frequency which depends on the aperture's size.

A further experiment was performed using a corona generator (Fig. 3.8), constituted of a needle, connected to an HV source, and a ground plane. The corona sample was placed inside the switchgear under test, along with a small 12 kV transformer.

An HFCT sensor was clamped around the sample ground connection in order to compare the results obtained using the antenna to those of the conventional inductive sensors.

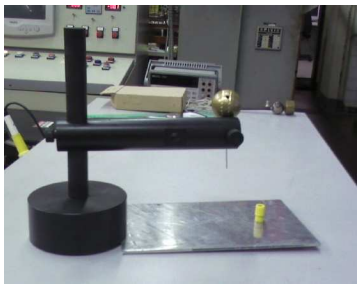

FIGURE 3.8 Needle-ground plane corona generator.

Figure 3.9 shows the results of the PD detection carried out through the log-periodic antenna, placed in position P2, connected to the Spectrum Analyzer. It can bee seen how the spectrum relevant to the corona PD is mostly concentrated between 250 and 350 MHz, i.e. around the resonant frequency of the shorter door's dimension. It must be observed that no spectral components were detected at higher frequencies. Indeed, it is possible that the spectrum of corona PD is not wide enough to excite the higher internal resonances of the switchgear. The log-periodic antenna was then connected to the Ultra Wide Bandwidth detector (already used in

Chapter 1) by means of a signal demodulator which allows to shift all the frequency components detected in VHF or UHF range, to the detector frequency bandwidth (16 kHz-40 MHz). In such a way it is possible to obtain PRPD patterns similar to those obtainable using conventional HFCT sensors connected to the PD detector and, thus, allow PD phenomena identification. Note that the two patterns differ in the polarity. The reason lies in the signal demodulator device, which works on the absolute value of the recorded signals.

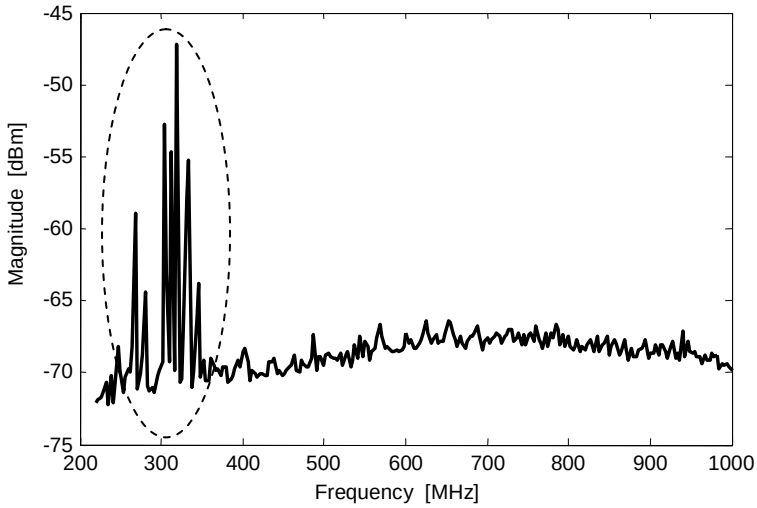

FIGURE 3.9 Frequency spectrum relevant to the corona PD detected through the log-periodic antenna connected to the Spectrum Analyzer.

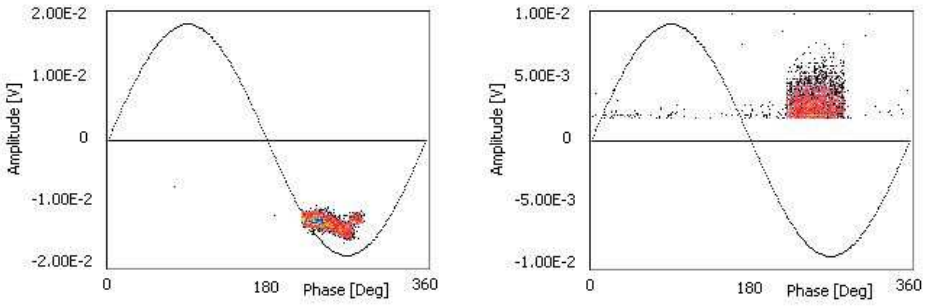

(a) HFCT (b) Log-periodic antenna

FIGURE 3.10 Patterns relevant to HFCT sensor (a) and log-periodic antenna (b).

3.3.3 Simulations using CAD systems

Simulations on PD irradiation outside MV switchgears were carried out using the same Computer Aided Design software of Chapter 2.

The same cabinet investigated in the previous paragraphs was modeled accurately according to its geometrical characteristics. Several discrete ports, simulating PD event occurring in different positions, were placed inside the modeled switchgear. The door's apertures were then represented through two thin rectangular slot apertures, 2 mm wide, simulating the air gap between the door and the cabinet, as sketched in Fig. 3.11.

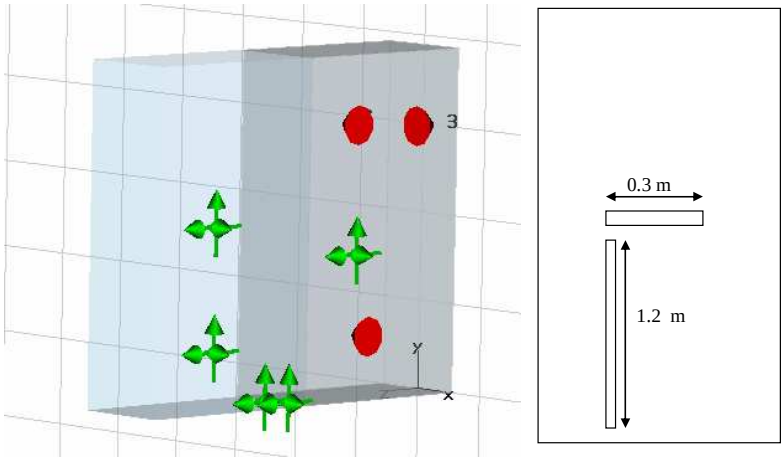

FIGURE 3.11 Simulated switchgear. Discrete ports simulating PD event are marked in red. Green arrows represent the EM field probes used for detection. Cabinet door's apertures are represented by narrow rectangular slots.

Electromagnetic field probes were used both inside and outside the cabinet to sense the EM irradiation. Several positions and orientation of the receiving probes were investigated. For the sake of brevity, it will be reported here only the result of one of the most significant simulations, where an electric probe was placed in front of the cabinet door, 300 mm close to the shortest door aperture and the source was placed in correspondence of the cabinet's center of the mass. The aim of the simulation was to replicate the results obtained from the experimental tests with the noise generator. Figure 3.12 collects the simulation results for several frequency values.

It can be observed that there is no irradiation outside the cabinet at 20 MHz. According to Figure 3.7, above 300 MHz variations of the electrical

field can be sensed, due to the excitation of the shortest aperture resonance. It can also be observed that at higher frequencies, i.e., above 1 GHz, there are some points, especially in correspondence of the door's aperture, where the irradiation is significantly higher. Therefore, the position of the antenna with respect to the door's aperture can influence the detection sensitivity.

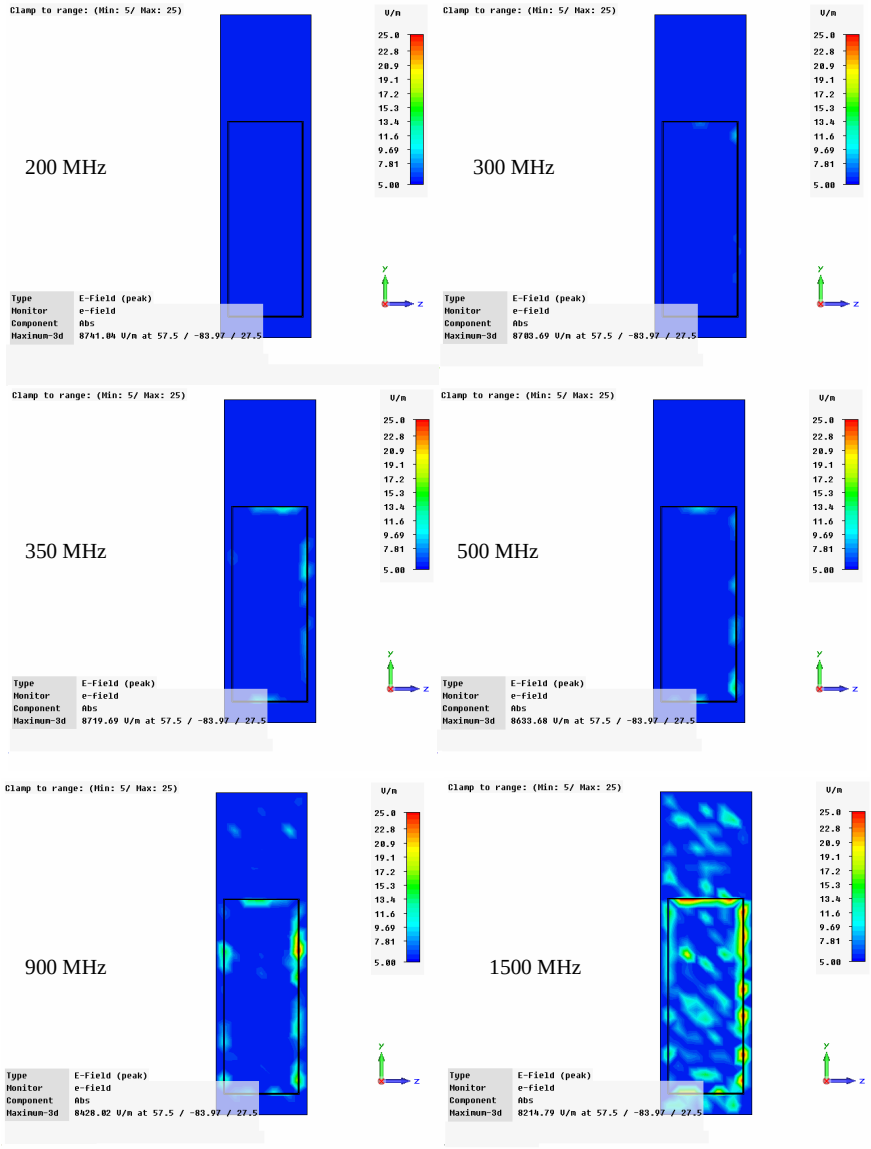

FIGURE 3.12 Simulated switchgear. Electrical field simulated outside the cabinet at different frequencies

Note that between 350 and 900 MHz the amplitude of the electric field detected close to the upper shortest door's aperture does not change

significantly in terms of peak, according to Fig. 3.7. On the contrary, significant variations can be noticed if detection is carried out close to the longer door's dimension.

It is anyway important to underline the main result of the investigation, which is the possibility of detecting, outside the switchgear, the irradiation associated to PD phenomena close to the apertures

3.4 PD detection through proper antenna sensors

It has been shown in the previous paragraphs that irradiation inside and outside the switchgears can occur consequently to a PD event.

Focusing the attention on the latter case, since introducing of sensors inside the switchgears is not possible on-line, two sensors can be used to sense the irradiation outside the cabinet:

1) TEV sensors, placed attached to the metallic surface of the cabinet

2) Antenna sensors, placed near the switchgear apertures.

The experimental results shown in Fig. 3.9 highlighted that EM waves associated to a corona PD event can be detected outside the cabinet close to the door's apertures and that maximum emission occurs in a frequency range centered on the resonant frequency of such apertures.

As demonstrated in Chapter 2, if the sensor is placed very close to the door's aperture (i.e. in the so-called reactive field region with respect to the slot) it is possible to sense also EM field variations in at frequencies related to the internal resonances of the cabinet. Therefore, the PD detection optimum bandwidth can vary according to both the cabinet and aperture's dimensions.

Considering the typical dimensions of the switchgears (height between 1.5 and 2 m, dept between 0.5 and 1.5 m, width between 0.5 and 1.5 m) and the typical dimensions of the rectangular apertures (L=0.3%1.5 m) it can be generally assumed that the detection bandwidth should involve lower frequencies with respect to the MV transformers studied in Chapter 2. An effective solution could be represented by antenna sensors having a wide bandwidth below 1 GHz. Indeed, the test carried out with the corona PD demonstrated that the irradiation associated to the corona was almost zero above 500 MHz.

A commercially available antenna, indicated in the follow as "TEM antenna" was found to be suitable for PD detection purposes in MV switchgear. Such an antenna is characterized by:

1) small dimensions: 50x30x200 mm

2) flat S11 up to 2 GHz

3) high capacitive coupling up to 500 MHz.

The comparison between the measured S21 parameter of the TEM antenna and the Horn antenna, described in Chapter 2, is shown in Fig. 3.13. Note that below 500 MHz the capacitive coupling of the TEM antenna is significantly higher if compared to that of the Horn. Therefore, by placing the antenna close to the cabinet's aperture it is possible to sense EM field variations at frequencies ranging in the VHF bandwidth (30 - 300 MHz).

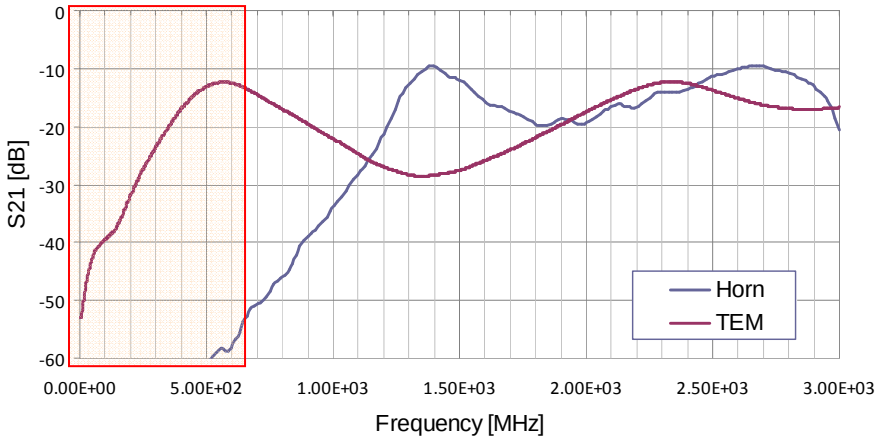

FIGURE 3.13 Comparison between measured S21 parameter of TEM and Horn Antenna

Chapter 4

Applications: on-line PD detection in MV grids

4.1 Premise

Optimum detection bandwidths have been singled out in the previous chapters for PD detection in MV cables, transformers and switchgears.

The results can be summarized as follows

- Cables: HFCT inductive sensors can be clamped around the cables ground lead or, alternatively, around the cable itself. The optimum bandwidth for such sensors has been found to lie within the range of few tens of MHz, in order to acquire PD pulses waveform, to carry out effective separation through proper algorithms [19-22] and, at the same time, achieve advantageous Signal-To-Noise-Ratio. Furthermore, antenna sensors can be used to detect the irradiation associated to PD sources inside the cable accessories, thus improving the detection and localization effectiveness.
- MV/LV Transformers: Installing HFCT sensors around cables ground connection it is possible to sense also the PD phenomena occurring inside the transformers. However, it has been demonstrated that using proper antenna sensors it is possible to detect, outside the transformers, also the irradiation associated to the PD events, thus improving the detection and localization. The apertures in the transformer, through which EM waves can

propagate outside, are those in correspondence of the bushings. Such apertures can behave as slot antennas, exhibiting resonances at frequencies even above 2 GHz. However, if proper sensors are placed close to the apertures (in the reactive-field region), it is possible to detect also the internal resonances of the transformer tank. The optimum bandwidth has found to lie in the UHF region.

- Switchgears: PD activities occurring inside the switchgears can be sensed also using the HFCT connected around the cables ground lead. However, to carry out PD detection also in spare panels it is necessary to use external sensors, such as antenna or TEV sensors. If antennas are used, it has been shown that irradiation can occur outside the switchgears in correspondence of apertures, due, as an example, to the small air gap between the switchgear door and the cabinet. Tests and simulations have shown that such irradiation can occur at frequencies even lower than 500 MHz. Therefore, sensors having bandwidth lying within this range seems to be suitable for PD detection in such apparatuses. It is however important that the central resonant frequency of antenna detectors should be not lower than the cabinet lowest resonance frequency.

The investigation carried out in the previous chapters is of utmost importance to develop proper sensors for on-line PD detection purposes in MV distribution grid. Indeed, on-line PD monitoring provide significant advantages if compared to off-line PD detection as, for instances, the possibility of carry out the measurements without shutting down the system along with the opportunity to assess the actual condition of the equipment under test in its normal working condition. This latter aspect is important especially in machines like transformers and motors. Indeed, the thermo-mechanical stress affecting such apparatuses on-line can not be reproduced off-line. On the other side, on-line measurement can introduce some disadvantage, as:

1. disturbances and noise can affect the measurement sensitivity;
2. PD pulses, associated to a PD source within one system, can propagate along the other interconnected apparatuses and be detected in different points, affecting the localization effectiveness.

The first issue can be solved determining the optimum detection bandwidth for each apparatus under test, as described in the previous chapters, in order to design proper sensors and to achieve optimum SNR. Furthermore, using proper detection instruments and algorithms [19-22] it is possible to separate the pulses associated to external disturbances to those coming from PD activities. As regards the second issue, it is necessary to carry out PD measurements in all the interconnected systems. As an example, if PD detection is carried out on a MV cables, it is suggested to extend the investigation also to the apparatuses connected at cable terminations, e.g., transformers, motors or switchgears.

4.2 Examples of on-line PD measurement setups

Two typical PD on-line measurement setups are here described.

When switchgears and MV transformers are connected at MV cable ends, respectively, it is suggested to install the PD sensors as shown in Fig. 4.1. In particular, HFCT should be clamped around the ground lead of the cables terminations in order to sense both PD activity within the cable and those inside the other apparatuses. For localization purposes, antenna sensors can be used, additionally, close to the switchgear and the transformer. Once the sensors are installed, PD detection could be carried out using a suitable PD instrument. It can be suggested to run a continuous monitoring session where critical situations have been found during the screening of the MV network. Alternatively to antennas, TEV sensors can be used for PD monitoring of MV switchgears. In particular, a commercially available TEV Jumper sensor is suggested. Its working principle is the same of TEV capacitive probes, since it is able to detect the impulsive transient currents traveling on the cabinet surface. The main difference with the other TEV probes is that it must be placed across the switchgear apertures. Owing to its direct coupling with the cabinet apertures, where irradiation occurs, such a sensor has been found to be more sensitive than the other TEV probes.

In large power-plants with 33 kV gas insulated cabinets, it can happen that the cables re not accessible in the switchgear room, but only in the lower floor. In such a case, TEV sensors and antennas can be used upstairs, while HFCT sensors can be installed downstairs, as sketched in Figure 4.2.

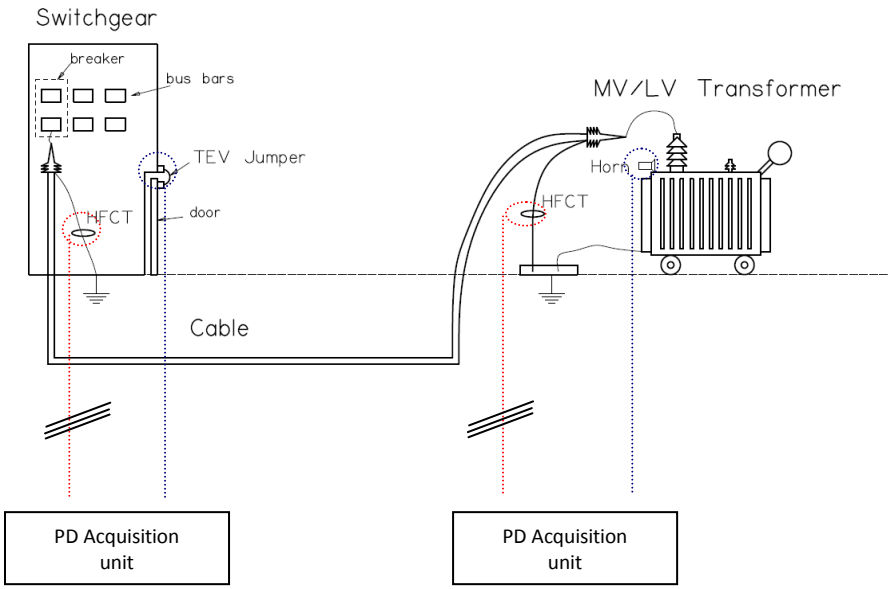

FIGURE 4.1 PD detection measurement setup for Switchgear-cable-transformer.

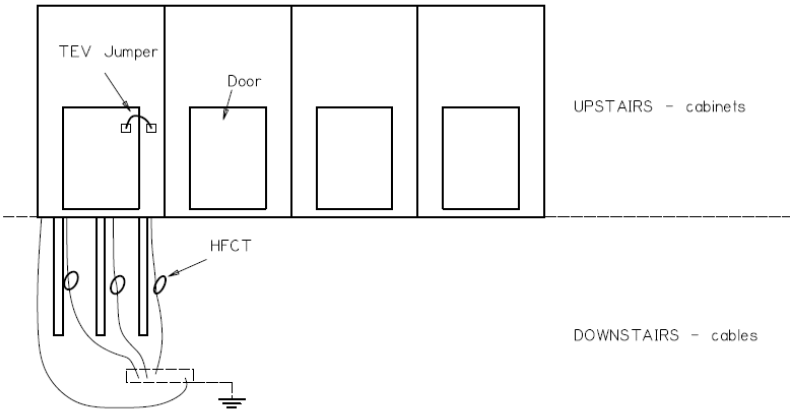

FIGURE 4.2 PD detection measuring setup in MV substation when cables are not accessible in the switchgear room.

Screening through acoustic sensors can be done, but, as emphasized in Chapter 3, such sensors are not able to detect any internal PD activity due to cavities in solid insulation materials.

4.3 PD detection and localization in MV cables

HFCT sensors were permanently installed around the ground lead of three 11 kV single-core cable terminations, located inside an MV air-insulated switchgear.

MV cables were connecting two switchgear substations (SS1 and SS2) 256 m far from each other, as sketched in Fig. 4.3. The three single-core cables monitored by the HFCTs were joined together into a three-core joint (J1) 43 m far from the measurement point (SS1). The three-core cable coming out from J1 was then split again in correspondence of joint J2 in three single-core cables before reaching the substation SS2. The joint J2 was 195 m far from the substation SS1 and 61 m far from the Substation SS2.

At first, measurements were carried out in SS1. Significant PD activity was found affecting all the phases. From the analysis of the Phase Resolved Partial Discharge (PRPD) pattern, shown in Fig.4.4, the PD activity was identified as an internal PD. Further measurements were thus scheduled within one month, in order to analyze the amplitude trend of this phenomenon, evaluate the PD harmfulness and plan the required maintenance on cables.

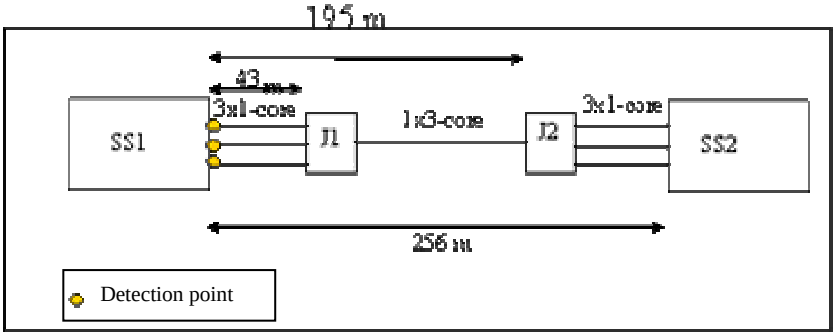

FIGURE 4.3 MV cable circuit layout.

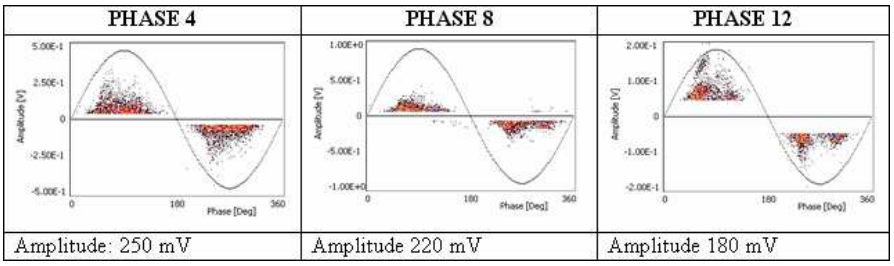

FIGURE 4.4 Internal PD activities acquired in MV cables through HFCT sensors

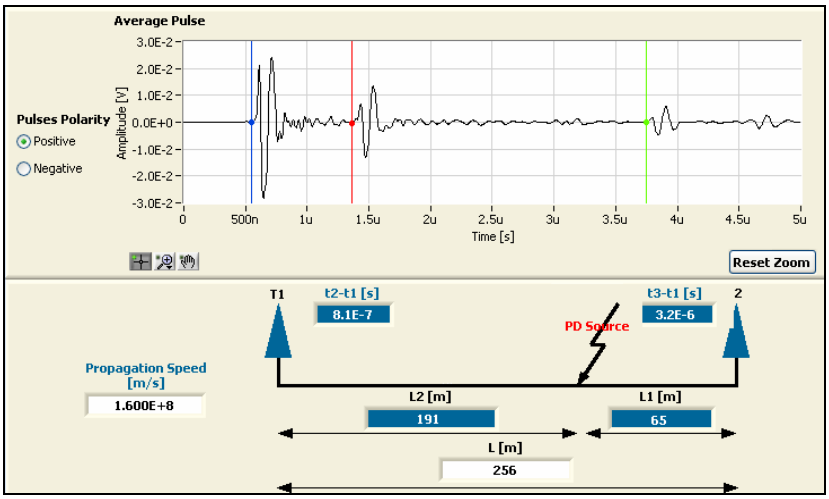

FIGURE 4.5 TDR software used to localize the PD source.

Resorting to Time Domain Reflectometry (TDR) techniques, PD waveforms were analyzed in order to localize the PD source within the cables (Fig. 4.5). As a matter of fact, once the total cable length is known and the propagation speed is estimated, it is possible to use software properly designed to estimate the distance between the measurement point and the PD source. Fundamental requirements in the use of such localization techniques are:

1. record the entire PD pulses waveform with appropriate time-length in order to capture multiple reflections along the cable;

2. use UWB detectors having at least 20 MHz of bandwidth in order to preserve the most of the PD pulses shape.

As shown in Figure 4.5, the PD source was localized at 191 m far from the substation SS1. Therefore, it was highly probable that the PD source could be located at joint J2. This result was confirmed by the TDR analysis done on the other two phases, indicating once again a PD source 191 m far from the measurement point, that is to say, in correspondence of the joint J2. From these results, it was speculated that the PD source could be inside the joint, between the phases in the three-core side. The small difference between the result given by the TDR method (191 m) and the actual distance between the joint J2 and the SS1 (195 m) was basically due to unavoidable

inaccuracies on the estimation of both the cable speed and the joint location by utility people.

Two other measurement sessions were carried out after 1 and 4 months, respectively. The recorded PRPD patterns are reported in Fig. 4.6, while the amplitude trend is shown in Fig. 4.7

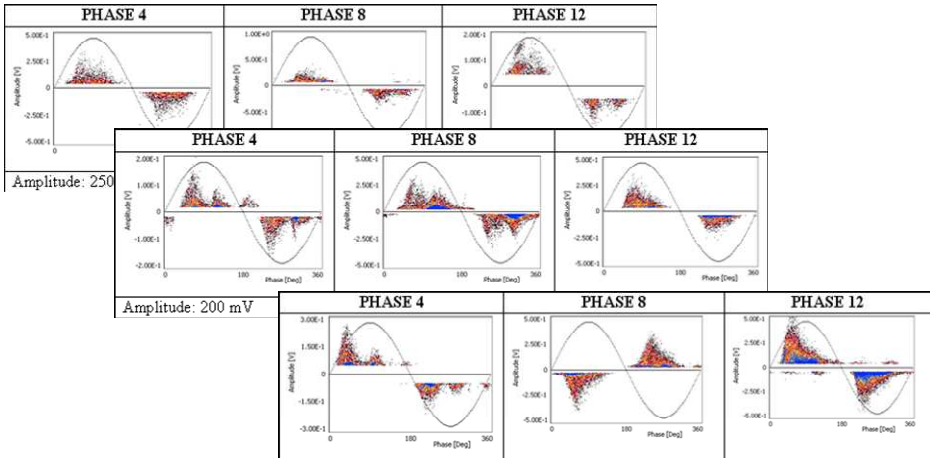

FIGURE 4.6 Acquired PRPD Patterns during the three measurement sessions. Note the increase of the PD activity in Phase 12.

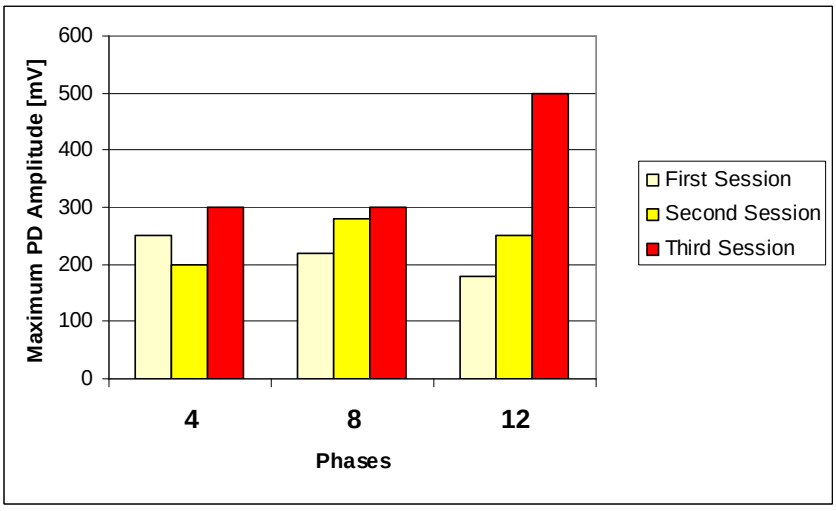

FIGURE 4.7 Amplitude trend of recorded PD activity in phases 4, 8 and 12. Note the significant increase of about 200 mV in phase 12 between the second and the third measurement.

No significant increase in terms of PD amplitude was observed after the second session except for phase 4 that experienced an increase of almost 100 mV. After the third measurement a significant increase in PD amplitude was noted in Phase 12, which was found to be 200 mV higher with respect to the previous measurement session. Hence, an alarm was given to the utility people, suggesting the replacement of joint J2.

The cable eventually failed during a DC hipot test on phase 12 carried out by utility personnel to analyze the current absorption of the line. Joint J2 was cut out from the cable and a phase/phase failure within the joint was found, as effectively predicted by the PD analysis.

4.4 PD detection in MV transformers

The measurements here described were carried out on several 400/15000 V oil-insulated transformers (see Fig. 4.8) in a solar park. Five transformers exploded during the last year, and the reason was unknown.

FIGURE 4.8 On-line PD measurement setup for a 400V / 15 kV oil insulated transformer in a solar park. PD detection carried out through HFCT and Horn Antennas.

Resorting to HFCT sensors, clamped around the cables ground lead, and Horn antennas, significant PD activities, likely due to interfaces between oil and air on the transformer top, were detected on-line. Figure

4.9 and 4.10 show the PRPD patterns detected through HFCT and horn antenna, respectively. The PD source was localized inside the transformer since it could be detected using both the antenna and the HFCT. show the PRPD patterns detected through HFCT and horn antenna, respectively.

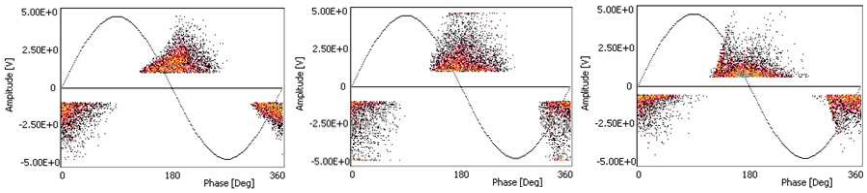

FIGURE 4.9 PRPD patterns acquired through HFCT clamped around MV cables connected at transformer terminals.

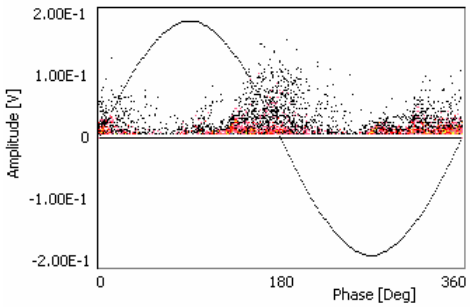

FIGURE 4.10 PRPD pattern acquired through Horn antenna sensor in correspondence of the cable entrance.

4.5 PD investigation in MV substations

4.5.1 PD sources localization in MV switchgears

Cross coupling between compartments in MV substations is unavoidable for both conducted as well as irradiated signals. Indeed, large number of cabinets are connected to the same bus bar and grounded at the same main earth, as sketched in Fig . As a consequence, the same PD phenomenon is usually observed in at least two adjacent compartments.

Localization can, therefore, become complex if not dealt with an appropriate methodology. Radiated signals outside the cabinet are affected by reflections, so that exact location is often more complex.

Conducted signals may give rise to localization problems when cabinets without cable earthing system (e.g., spare cabinets) are affected by PD activities (e.g., in spacers): these PD may be detected in other cabinets giving rise to wrong localization.

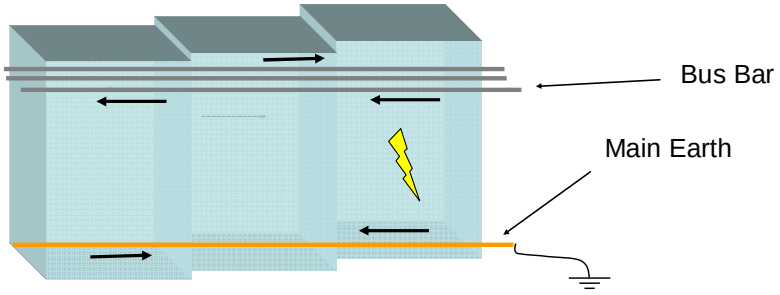

FIGURE 4.11 Switchgears are connected one each other through MV busbar and common earth. When PD occur inside one cabinet, it can be sensed also in the adjacent ones.

To achieve exact PD source location the following procedure could be employed. First of all, measurements should be performed on all the compartments within the same room. Generally, when a PD source is active, one or more adjacent compartments will provide positive evidence of PD activity. The compartments where PD phenomena are located with highest likelihood are tested again, for both TEV and (if possible) conducted signals. Generally speaking, the compartment where the PD source is located will be characterized, with respect to the others, by:

- PD pulses having larger magnitude and equivalent bandwidth;
- Larger repetition rate

These considerations can be used to devise a location index, $L_{I,}$ evaluated as (4.1), where Q_{max} is the 98^{th} percentile of the PD amplitude distribution (in mV) and F is the equivalent bandwidth of the pulse (in MHz), evaluated as (1.24). Due to attenuation phenomena, the larger L_I in one compartment, the larger the probability that the PD source is located within the compartment itself. It must be observed that the repetition rate parameter is not taken into account and should not considered for localization purposes, since it can strongly depend on the way noise couple with a particular compartment, fluctuate randomly, etc., repetition rate.

$$L_I = Q_{\max} \cdot F \tag{4.1}$$

Moreover, it must be stressed that such a localization index can be evaluated only if the same sensor is used in correspondence of each cabinet, during PD measurements. As a matter of facts, different sensors can have significantly different bandwidth and sensitivity, resulting in the impossibility to correlate the recorded Q_{max} and F parameter. HFCT sensors are suggested for such applications, since the PD amplitude recorded through antenna and TEV sensors can vary with the sensor position.

Examples relevant to PD localization in MV switchgears, resorting to the Localization Index application, are described in the following. The first example refers to a PD measurement carried out in a 33 kV substation. In total, 13 compartments were scanned for PD using the HFCT sensor around the ground lead of 33 kV cables connected to each compartment.

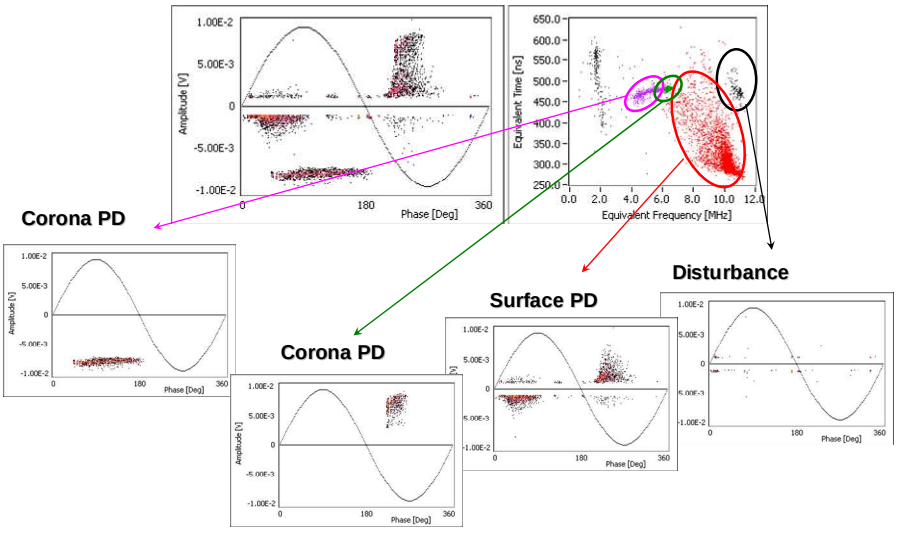

FIGURE 4.12 Example of acquisition and separation in a 33 kV MV switchgear. Several phenomena were detected, but only one critical (the surface PD).

Two PD phenomena were observed on almost all the compartments. They were separated exploiting the characteristics of the pulse waveshapes [75]. The first one (see the pattern reported in Figure 4.12)

was addressed to surface PD, i.e., PD occurring on an insulating surface, caused by prevailingly tangential field, [76]. These PD are typical of tracking phenomena occurring at cable terminations, therefore further investigations were needed to determine the exact location of the source. Localization was firstly attempted by checking the maximum magnitudes of PD recorded at each cubicle, as shown in Fig.4.13.

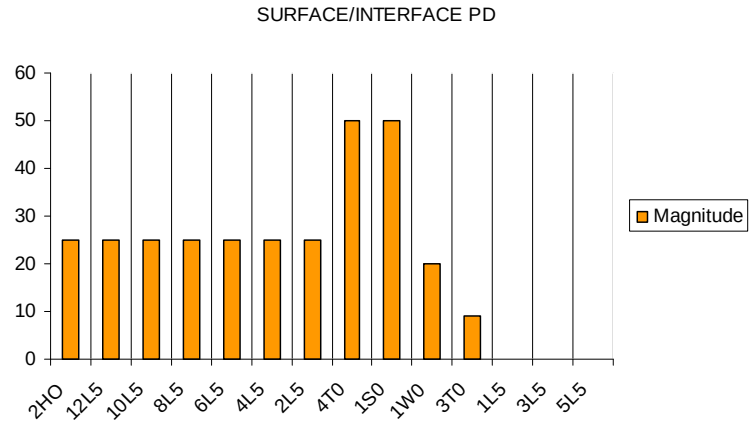

FIGURE 4.13 Comparison of maximum PD magnitudes (in mV) recorded for the Surface PD of Fig. 4.12.

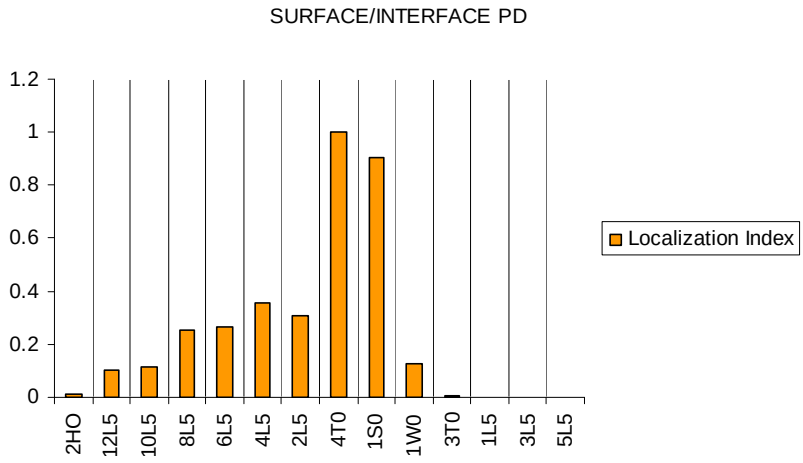

FIGURE 4.14 comparison of (normalized) localization index values for the surface phenomenon of Fig. 4.12.

The results were partially inconclusive: two of the cubicles had larger PD levels (4T0 and 1SO), but the maximum levels were not significantly different. Using the localization index (Fig. 4.14), it could be ascertained that PD were occurring at compartment 4T0. The second phenomenon

(see the PD pattern reported in Fig. 4.12) could be ascribed to corona phenomena. This phenomenon was recorded on several compartments, so that localization through the index (1) was attempted. The result, reported in Fig. 4.14 permitted to address it to compartment IL5. In this case, maintenance was not scheduled due to the fact that corona PD are not harmful if not of very large intensity. However, it must be noted the importance of separation and identification procedure: maintenance based only on PD magnitude is not effective. As an example, suppose to decide to carry out maintenance in the cabinet where PD activity is found to have maximum amplitude. In this case, Panel 1L5 would be taken out of service. But, the activity occurring inside such a panel is just a corona PD, i.e., not equally harmful to the surface PD occurring in panel 4T0. As a matter of fact, panel 4T0 is the critical switchgear, although the surface PD was much lower than the corona in 1L5. As a demonstration, panel 4T0 had a failure in cable termination after only four months from the measurement.

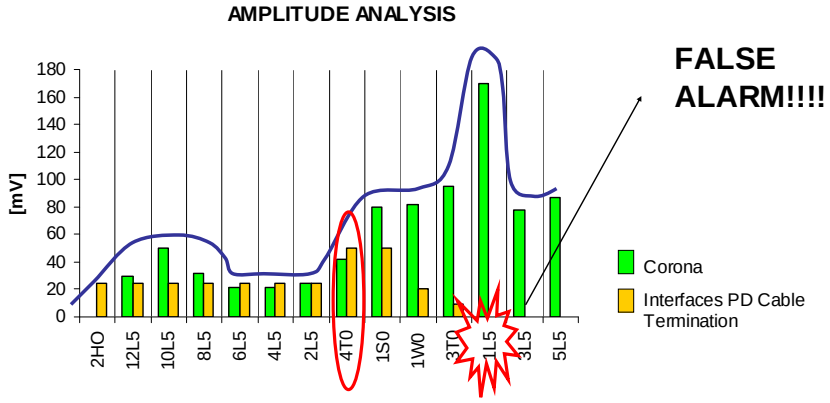

FIGURE 4.15 Comparison between the corona and surface PD amplitude. PD analysis and diagnosis based only on PD amplitude are not effective if multiple PD sources are not properly separated and identified.

4.5.2 PD detection in MV switchgears through EM field couplers

Both TEV jumper sensor and HFCT were used to pick up PD signals from a 15 kV air insulated compartment. The HFCT was clamped around the ground lead of the cable termination.

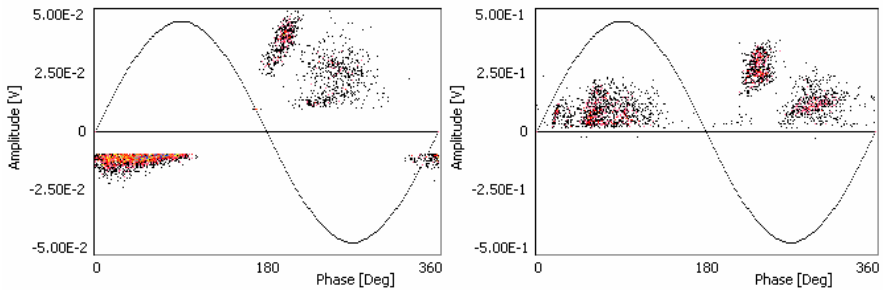

FIGURE 4.16 PD activity measured at a MV switchgear cubicle using an HFCT clamped on cable ground lead (left). PD activity measured at a MV switchgear cubicle using a TEV jumper sensor (right).

Figure 4.16 (left) shows the PD pattern of a phenomenon that could be ascribed (based on the artificial intelligence tool of the PD detector, then confirmed after opening the cubicle) to surface PD occurring at a cable termination. Figure 4.16 (right) shows the PD measurements carried out by sweeping the TEV jumper on the cubicle surface. It comes out that, apart from some distortion (associated with the use of a non-linear circuit as an interface between sensor and detector), the TEV sensor is able to pick up the PD signal, providing a pattern that can be fed to automatic identification system for PD source identification.

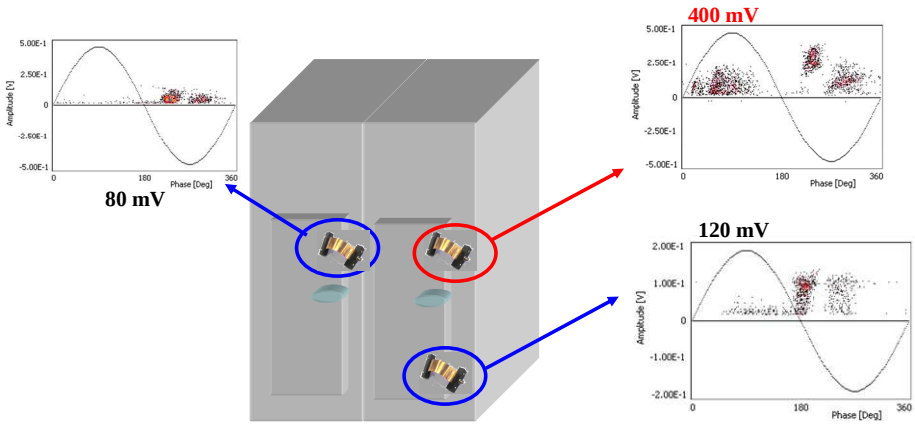

FIGURE 4.17 Example of PD detection carried out using TEV Jumper sensor across cabinet's apertures. The maximum amplitude was found to be at the same height of the cable termination, confirming the location of the PD sources in the cable.

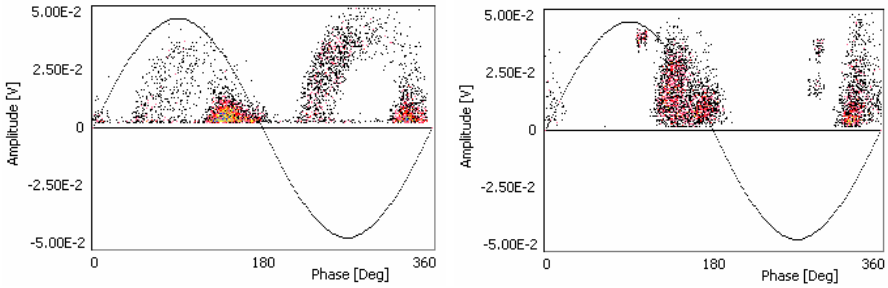

FIGURE 4.18 Internal and surface PD detected through TEM antenna sensor.

Furthermore, TEM antenna sensor was used to sense PD in the same substation of Figs. 4.13-4.16. The pattern shown in Fig. 4.18 (left) is relevant to an internal PD within a solid material, likely due to a cavity in the epoxy barriers or ceramic bushings. Such PD activity was detected in a spare panel, confirming the effectiveness of using antenna sensors in MV substations in addition to HFCT.

The second PRPD pattern (Fig. 4.18, right) is relevant to the same surface PD detected in panel 4T0 using the HFCT connected to the cable. The same surface PD was detected also in the adjacent panels, but with significantly lower amplitude and repetition rate.

4.5.3 Discrimination between PD sources close and far from the switchgears

At last, another example describing the presence of multiple sources inside a MV substation is dealt with in the following.

In the substation under exam, 15 switchgears were investigated. A three-core MV cable was connected inside each switchgear. Pumps and motors were connected to the other cables end, in a industry 200 m far from the MV substation, as sketched in Fig. 4.19.

HFCT sensors were clamped around each MV cable, since the ground lead was not accessible. Several PD activities were sensed in each cable, but, thanks to the sensors appropriate bandwidth, along to the T-F separation map, it was possible to separate successfully PD activities occurring inside the substation cabinets from those located either in the MV cables or in the machines connected at the far end.

Indeed, the PRPD pattern was obtained in each measurement point, and different phenomena were separated as shown in Fig. 4.20.

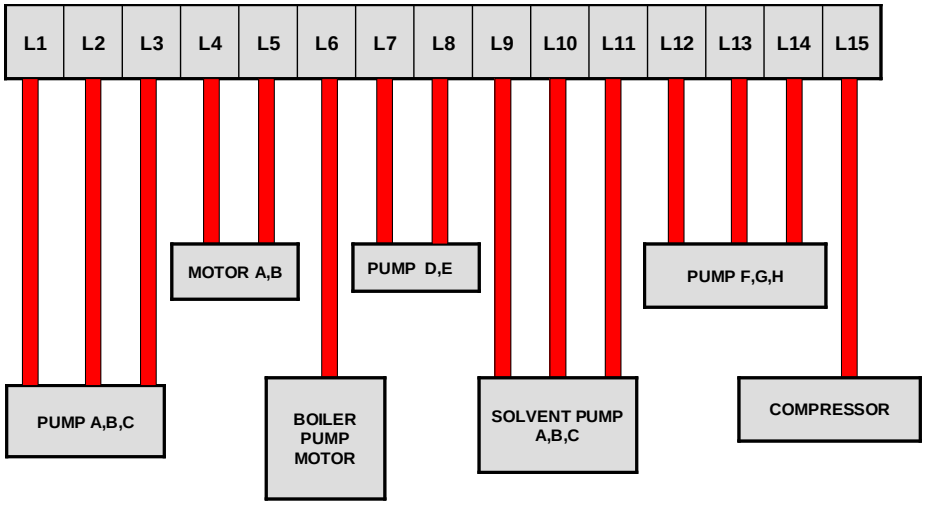

FIGURE 4.19 Layout of a power-plant. All cables are connected to switchgears, at one end, and to motors/pumps at the other end.

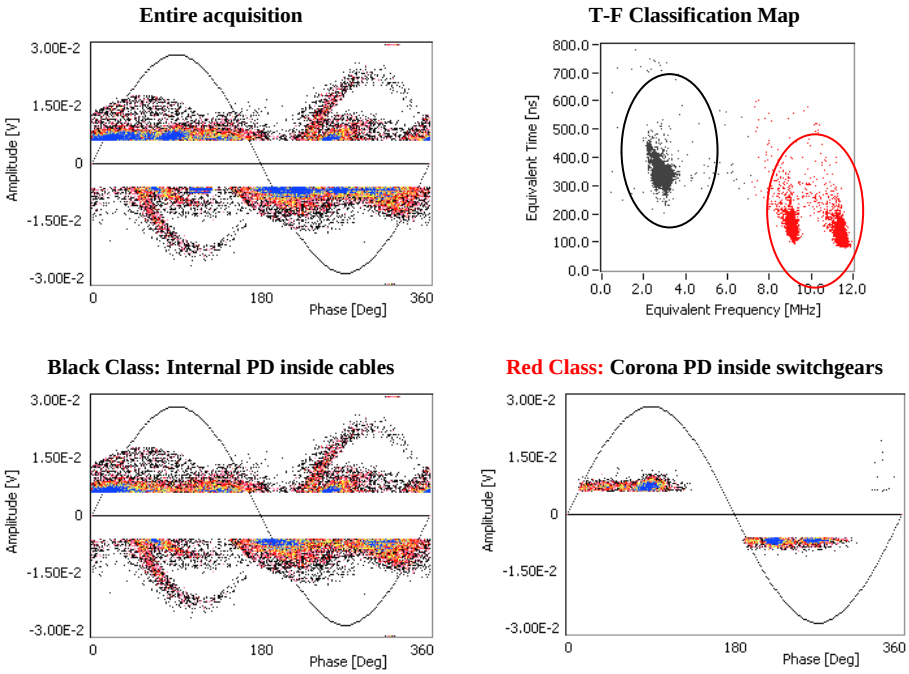

FIGURE 4.20 Example of PD acquisition in one of the switchgears of Fig. 4.19. Low frequency internal PD are relevant to defects in paper-oil cable insulation, far from the detection point. High frequency clusters in the T-F Map are relevant to PD located inside one of the switchgears, close to the detection point.

In every cabinet, PD phenomena having significantly high F parameter (i.e., equivalent frequency > 8 MHz) were detected, due to corona and surface activities. Such activities were clearly due to PD source inside some cabinet in the switchgear room. Since all the cabinets were interconnected, it was easy to sense such activities in all the panels. However, resorting to the Localization Index analysis, it was possible to address the PD source to the appropriate panel.

In addition, a low frequency activity (F<4 MHz) can be observed in Figure. 4.20, having the typical characteristics of a insulation defect due to presence of multiple cavities. However, this PD activity was easily addressed to a PD source far from the switchgear room, thus occurring either inside the MV cable or in the motor (or pump) connected at the cable far end. The reason of such diagnosis is lying in three fundamental facts:

1. this PD activity was not sensed in the adjacent panels;
2. this PD activity was not sensed through antenna sensors;
3. the relevant equivalent frequency is quite low, indicating the presence of attenuation phenomena between the PD source and the detection point.

As a matter of fact, according to the investigation carried out in Chapter 3, when PD occur inside a switchgear, it is expected to detect the irradiation associated to the PD with proper sensors placed close to the cabinet.

Furthermore, as an effect of both the irradiation and the interconnection between the cabinets through the MV bus bars, it is expected to sense the same phenomenon, but with lower amplitude, in the adjacent panels.

On the contrary, when a PD occur far from the switchgear rooms, it can propagate along the MV cables, so that it can arrive in the substation and be detected through HFCT clamped around the cables. However, PD pulses associated to this PD will arrive to the switchgear considerably attenuated in amplitude and frequency, due to the attenuation in the MV cables, and will not produce any kind of irradiation.

4.6 Conclusion

Investigation on PD propagation in MV apparatuses was carried out in order to single out the optimum detection bandwidth.

Irradiation phenomena were studied in cables, switchgears and transformers, showing the real possibility to assess the insulation condition using properly designed antenna sensors along width conventional inductive sensors installed on MV cables ground lead.

By providing a large number of MV systems with permanently installed sensors, it is possible to carry out PD measurements using the same PD detector, in order to

- acquire the PD pulses;
- separate the PD activities from disturbances/noise and crosstalk (i.e., PD activities occurring in other phases or systems);
- correlate the data;
- localize the PD source;
- address proper diagnosis;
- carry out proper maintenance.

In such a way, investment on diagnostics in MV distribution grid is economically viable and effective.

Prerequisite to develop proper sensors is the accurate knowledge of the PD propagation properties within the systems under investigation. The work here presented highlighted innovative techniques and models to both analyze and predict the frequency optimum bandwidth where PD detection can performed achieving maximum SNR.

Such techniques and models can be further developed and improved in order to extend the investigation over a wide range of systems having different geometries, both in MV and in HV.

References

[1] IEC 60270, *Partial Discharge Measurement*, 3rd Edition, 2001.

[2] R. Villefrance, J. T. Holboll and M. Herinksen, "Estimation of medium voltage cable parameters for PD-detection", IEEE Intern. Sympos. Electr. Insul. (ISEI), Arlington, Virginia, USA, pp. 109-112, 1998.

[3] R. Papazyan and R. Eriksson, "Calibration for time domain propagation constant measurement on power cables", IEEE Trans. Instrum. Meas., Vol. 52, pp. 425- 418, 2003.

[4] G. C. Stone and S. A. Boggs, "Propagation of partial discharge pulses in shielded power cables", IEEE Conf. Electr. Insul. Dielectric Phenomena (CEIDP), pp. 275-280, 1982.

[5] R. Papazyan, P. Pettersson, H. Edin, R. Eriksson and U. Gäfvert, "Extraction of high frequency power cable characteristics from S-parameter measurement", IEEE Trans. Dielectr. Electr. Insul., Vol. 11, pp. 461-470, 2004.

[6] G. Mugala, R. Eriksson, U. Gäfvert and P. Pettersson, "Measurement technique for high frequency characterization of semi-conducting materials in extruded cables", IEEE Trans. Dielect. Electr. Insul., Vol. 11, pp. 471-480, 2004.

[7] S. Chandrasekar, A. Cavallini, G. C. Montanari and F. Puletti "Bandwidth and sensitivity issues in PD detection in power cables", IEEE Trans. Dielectr. Electr. Insul., Vol. 14, pp. 735-743, 2007.

[8] M. Hasheminezhad, M. Vakilan, T.R. Blackburn and B.T. Phung, "Direct introduction of semicon layers in XLPE Cable Model", Intern. Conf. on Power System Technology, pp. 1-7, 2006.

[9] C. Xu, L. Zhou, J.Y.Zhou and S. Boggs, "High frequency properties of shielded power cable – part 1: overview of mechanisms", IEEE Electr. Insul. Mag., Vol. 21, No. 6, pp. 24-28, 2005.

[10] A. Ametani, Y. Miyamoto and N. Nagaoka, “Semiconducting layer impedance and its effect on cable wave propagation and transient characteristics”, IEEE Trans. Power Delivery, Vol. 19, pp. 1523-1531, 2004.

[11] H. N. O., T. R. Blackburn, B.T. Phung. M. Vakilan, M. S. Naderi and H. Zhang, “Investigation of high frequency signal propagation characteristic on HV XLPE cables”, 7th intern. Power Engineering Conf., IPEC, Vol. 2, pp. 776-781, 2005.

[12] G. Mugala, R. Eriksson and P. Pettersson, “Dependence of XLPE insulated power cable wave propagation characteristics on design parameters”, IEEE Trans. Dielectr. Electr. Insul, Vol. 14, pp. 393-399, 2007.

[13] C. Xu, L. Zhou, J. Y. Zhou and S. Boggs, “High frequency properties of shielded power cable. part 1: overview of mechanisms”, IEEE Electr. Insul. Mag., Vol. 21, No. 6, pp. 24-28, 2005.

[14] C. Xu and S. Boggs, “High frequency properties of shielded power cable. part 3: loss from neutral Wire-Shielded Interaction”, IEEE Electr. Insul. Mag., Vol. 23, No. 2, pp. 12-15, 2007.

[15] W. T. Shugg, *Handbook of Electrical and Electronic Insulating Materials*, New York, NY, USA, Van Nostrand Reinhold Company, 1986.

[16] N. Oussalah, Y. Zebboudy and S. Boggs, “PD pulse propagation in shielded power cables for symmetric and asymmetric PD pulses”, IEEE Intern. Sympos. Electr. Insul. (ISEI), Toronto, Canada, pp. 30-33, 2006.

[17] L. A. Wainstein and V. D. Zubakov, *Extraction of signals from noise*, Dover, 1970.

[18] N. Oussalah, Y. Zebboudj and S. A. Boggs, “Analytic solutions for pulse propagation in shielded power cable for symmetric and asymmetric PD pulses”, IEEE Trans. Dielectr. Electr. Insul., Vol. 14, pp. 1264-1270, 2007.

[19] A. Cavallini, A. Contin, G. C. Montanari and F. Puletti, “Advanced PD inference in on-field measurements. I. Noise rejection”, IEEE Trans. Dielectr. Electr. Insul., Vol. 10, pp. 216 - 224, 2003.

[20] A.Cavallini, G. C. Montanari and F. Puletti, “A novel method to locate PD in polymeric cable systems based on amplitude-frequency (AF) map”, IEEE Trans. Dielectr. Electr. Insul., Vol. 14, pp. 726-734, 2007.

[21] A. Contin, A. Cavallini, G. C. Montanari, G. Pasini and F. Puletti, “Digital detection and fuzzy classification of partial discharge

signals", IEEE Trans. Dielectr. Electr. Insul., Vol. 9, pp. 335-348, 2002.

[22] A. Cavallini, M. Conti, A. Contin, G. C. Montanari. "Advanced PD inference in on-field measurements. II. Identification of defects in solid insulation systems", IEEE Trans. Dielectr. Electr. Insul., Vol. 10, pp. 528-538, 2003.

[23] IEEE Std 400.3, "IEEE Guide for Partial discharge Testing of Shielded Power Cable Systems in a Field Enviroment", 2006.

[24] P. D. Agoris, S. Meijer, E. Gulski, J. J. Smit, T. J. W. Hermans and L. Lamballais, "Sensitivity check for on-line VHF/UHF PD detection on Transmission cables", IEEE Intern. Sympos. Electr. Insul. (ISEI), Indianapolis, USA, pp. 58-61, 2004.

[25] N. H. Ahmed, N. N. Srinivas, "On-line partial discharge detection in cables", IEEE Conf. Electr. Insul. Dielectr. Phenomena (CEIDP), pp. 214-217, Minneapolis, USA, 1997.

[26] J. Veen and P. C. J. M. van der Wielen, "The application of matched filters to pd detection and localization", IEEE Electr. Insul. Mag., Vol. 19, No. 5, pp 20-26, 2003.

[27] L. Hao, P. L. Lewin and S. J. Doos, "Partial discharge source characterization within a HV cable joint", IEEE Intern. Conf. on Solid Dielectrics (ICSD), Winchester, UK, pp. 577-580, July, 2007.

[28] Hockanson D.M., Drewniak J.L., Hubing T.H., Van Doren T.P., Fei Sha, Wilhelm M.J, "Investigation of fundamental EMI source mechanisms driving common-mode radiation from printed circuit boards with attached cables", IEEE Trans. on EMC, Vol. 38, no. 4, pp. 557 – 566, Nov. 1996.

[29] Hwan-Woo Shim; Hubing, T.H., "Model for estimating radiated emissions from a printed circuit board with attached cables due to Voltage-driven sources", IEEE Trans. on EMC, Vol. 47, no. 4, pp. 899 – 907, Nov. 2005.

[30] Shaowei Deng, Hubing, T, Beetner, D, " Estimating Maximum Radiated Emissions From Printed Circuit Boards With an Attached Cable", IEEE Trans. on EMC, Vol. 50, no. 1, pp. 215 – 218, Feb. 2008.

[31] F. W. Grover, Inductance calculations, Van Nostrand Company, Inc., New York, USA, 1946.

[32] F. M. Tesche, M. V. Ianoz, T. Karlsson, EMC analysis methods and computational models, John Wiley & Sons, Inc., New York, USA, 1997.

[33] CST Microwave Studio v.5 Manuals.

[34] IEEE Std C57.113, “IEEE Guide for Partial Discharge Measurement in Liquid-Filled Power Transformers and Shunt Reactors”, 2002.

[35] M. D. Judd, O. Farish, B. F. Hampton, “The Excitation of UHF Signals by Partial Discharges in GIS”, IEEE Trans on Dielectr. and Electr. Insul., Vol 3, No. 2, pp.213-228, April 1996.

[36] J. S. Pearson, B. E Hampton and A. G. Sellars, "A Continuous UHF Monitor for Gas-insulated Substations", IEEE Trans. on Electrical Insulation, Vol. 26, No. 3, pp. 469478,1991.

[37] A. Petit, "Field Experience of Partial Discharge Monitoring with the UHF Method", Proceedings of the 9th ISH (Graz), Vol. 5, pp. 5596-1 – 5596-4, 1995

[38] S. Pack, A. Diessner and J. Gorablenkow, "PD Signal Propagation in GIS Considering Frequencies up to GHz", Proceedings of the 8th ISH (Yokohama), Vol. 3, pp. 93-96,1993.

[39] M. Hikita, S. Ohtsuka, T. Teshima, S. Okabe and S. Kaneko, “Electromagnetic (EM) Wave Characteristics in GIS and Measuring the EM Wave Leakage at the Spacer Aperture for Partial Discharge Diagnosis”, IEEE Trans on Dielectr. and Electr. Insul, Vol. 14, No. 2, pp 453-460, April 2007

[40] M.D. Judd, Li Yang, I.B.B. Hunter, “Partial discharge monitoring of power transformers using UHF sensors. Part I: sensors and signal interpretation”, IEEE Electr. Insul. Mag., vol. 21, no. 2, pp. 5-14, March-April 2005.

[41] IEEE Std C57.127, “IEEE Guide for the Detection and Location of Acustic Emissions from Partial Discharges in Oil-Immersed Power Transformers and Reacors”, 2007.

[42] C. A. Balanis, Advanced Engineering Electromagnetics, Wiley and Sons, New York, 1989.

[43] A. W. Rudge, K. Milne, A. D. Oliver, P. Knight, *The Handbook of Antenna Design* (Ieee Electromagnetic Waves Series), Vol. 1

[44] A.M. Boifot, “Broadband method for measuring dielectric constant of liquids using an automatic network analyser” IEE Proc. H. Microwave Antennas and Propagation, vol. 136, no. 6, pp 492-498, December 1989.

[45] H. A. Bethe, "Theory of Diffraction by Small Holes," Physical Review, Vol. 66, pp. 163-182 (1944).

[46] M. Born and E. Wolf, Principles of Optics: Electromagnetic Theory of Propagation, Interference and Diffraction of Light, Sixth Edition, Pergamon Press, pp. 109-121 (1980).

[47] C. J. Bouwkamp, "Diffraction Theory," Rep. Prog. Phy., Vol. 17, pp. 35-100 (1954).

[48] S. Ramo, J. R. Whinnery, and T. Van Duzer, Fields and Waves in Communication Electronics, Second Edition, John Wiley & Sons, Inc., pp. 422-428 (1984).

[49] Lord Rayleigh, "On the Passage of Waves Through Apertures on a Plane Screen," Philosophical Magazine, Vol. 43, No. 263 (April 1897).

[50] J. E. Casper, D. R. Rutt, and D. E. Tremain “Performance of standard aperture shielding techniques at microwave frequencies” Proc. On IEEE 1988 International Symposium on EMC, pp218-222, Seattle, WA, USA.

[51] MENDEZ, H.A.: ‘Shielding theory of enclosures with apertures’, IEEE Trans., 1978, EMC-20, (2), pp. 296-305

[52] AUDONE. B., and BALMA. M.: ‘Shielding effectiveness of apertures in rectangular cavities’, IEEE Trans., 1989, EMC-31, (1), pp. 102-106

[53] W. L. Stutzman and G. A. Thiele, Antenna Theory and Design, John Wiley & Sons, Inc. (1981).

[54] C. G. Montgomery, R. H. Dicke, E. M. Purcell, *Principle of microwave circuits* (IEE Electromagnetic Waves Series), Vol. 25, McGraw-Hill, 1948

[55] S. Cohn, “Microwave Coupling by Large Apertures”, Proc. I.R.E, Vol. 40, No. 6, pp.696-699, June 1952.

[56] R. Lee and D. G. Dudley “Transient Current Propagation Along a Wire Penetrating a Circular Aperture in an Infinite Planar Conducting Screen”, IEEE Trans.Electromagn. Compat., Vol. 32, No. 2, May 1990

[57] E.S. Siah, K. Sertel, J.L. Volakis and V. Liepa “EM Coupling and suppression through slots into lossless overmoded cavities using the Multilevel Fast Multipole Algorithm”, Proc. IEEE Int. Symp. On EMC, Vol.1, pp.161-166, 19-23 August, 2002.

[58] J. D. Turner, T. M. Benson, C. Christopoulos, D. W. P. Thomas, M. P. Robinson, J. F. Dawson, M. D. Ganley, A. C. Marvin, and S. J. Porter, “Characterization of the shielding effectiveness of equipment cabinets containing apertures,” in Int. Symp. EMC, Rome, Italy, Sept. 1996, pp. 574–578.

[59] M.P. Robinson, T.M. Benson, C. Christopoulos, J.F. Dawson, M.D. Ganley, A.C. Marvin, S.J. Porter, and D.W.P. Thomas, "Analytical formulation for the shielding effectiveness of enclosures with

apertures," IEEE Trans. Electromagn. Compat., vol. 40, no. 3, pp. 240-247, Aug. 1998.

[60] F. Po'ad, M. Mohd, C. Christopoulos and D.W.P. Thomas, "Estimation of Electric and Magnetic Shielding Effectiveness of a Metallic Enclosure with Apertures", Proc. International RF and Microwave Conference, pp. 291-295, Spetember 12-14 2006, Putrajaya, Malaysia

[61] M.P. Robinson, J.D. Turner, D.W.P. Thomas, J.F. Dawson, M.D. Ganley, A.C. Marvin, S.J. Porter, T.M. Benson and C. Christopoulos "Shielding effectiveness of a rectangular enclosure with a rectangular aperture"

[62] C. Christopoulos, The Transmission Line Modeling Method TLM. IEEE Press, New York, 1995.

[63] Dawson, J.F.; Ahmadi, J.; Marvin, A.C., "Reduction of radiated emissions from apertures in resonantenclosures by the use of lossy materials", IEE Colloquium on Screening of Connectors, Cables and Enclosures, 17 Jan 1992 Page(s):3/1 - ¾ Digital Object Identifier

[64] De Smedt, R. et al., "Assessment of the shielding effectiveness of a real enclosure" International Symposium on EMC, Rome, Italy, Sept. 14-18 1998, pp248-253.

[65] T. Konefal, J.F. Dawson, A. Denton, T. M. Benson, C. Christopou1os, A.C. Marvin, S.J. Porter, D.W.P. Thomas "Electromagnetic field predictions inside screened enclosures containing radiators" Proc. International Conference and Exhibition on EMC, pp. 95-100, York, UK, 1999.

[66] T. G. Tang, Q. M. Tieng, and M. W. Gunn "Equivalent Circuit of a Dipole Antenna Using Frequency-Independent Lumped Elements", IEEE Trans on Antennas and Propagation, Vol. 41, No.1, pp.100-103, January 1993

[67] K. C. Gupta, R. Garg, and I. J. Bahl, Microstrip Lines and Slotlines. Norwood, MA: Artech House, 1979, ch. 7.

[68] K.S. Kunz, and R.J. Luebbers, The Finite Difference Time Domain Method for Electromagnetic. CRC Press, Boca Raton, 1993.

[69] P.P. Silvester and R.L. Ferrari, Finite Elements for Electrical Engineers. Cambridge University Press, 2P^{ndp} Edition, Cambridge, 1990.

[70] Kyung-Ho Chung; Sung-Ho Pyun; Chung, S.-Y.; Jae-Hoon Choi, "Design of a wideband TEM horn antenna" Proc. Intern. Symp. on Antennas and Propagation Society, Vol.1, pp. 229 – 232, 22-27 June 2003.

[71] N. Davies, D. Jones, “Testing distribution switchgear for partial discharge in the laboratory and the field”, IEEE ISEI, Vancouver (CA), 9-12 June 2008, pp. 716-719.

[72] C. Kane, I. Blokhintsev, A. Golubev, “Measurement and analysis of partial discharges in switchgear”, IEEE EIC, 23-26 Oct. 2005, pp. 203-210.

[73] D. King, K. Feser, "High Voltage Test Techniques", 2001, Newnes, 2nd edition.

[74] L.E. Lundgaard "Partial Discharge - Part XIV: Acoustic PArtial Discharge Detection - Practical Application ", IEEE Electr. Insul. Mag., vol. 8 no. 5, pp. 34-43 Sept/Oct 1992

[75] A. Cavallini, G. C. Montanari, A. Contin, F. Puletti, “A new approach to the diagnosis of solid insulation systems based on PD signal inference”, IEEE Electr. Insul. Mag., vol. 19, no. 2, pp. 23-30, April 2003.

[76] A. Cavallini, M. Conti, A. Contin and G.C. Montanari, “Advanced PD inference in on-field measurements. Part 2: Identification of Defects in Solid insulation Systems IEEE Trans. on Diel. and Elec. Insul., Vol. 10, No. 3, pp. 528-538, June 2003.